



저작자표시-비영리-동일조건변경허락 2.0 대한민국

이용자는 아래의 조건을 따르는 경우에 한하여 자유롭게

- 이 저작물을 복제, 배포, 전송, 전시, 공연 및 방송할 수 있습니다.
- 이차적 저작물을 작성할 수 있습니다.

다음과 같은 조건을 따라야 합니다:



저작자표시. 귀하는 원저작자를 표시하여야 합니다.



비영리. 귀하는 이 저작물을 영리 목적으로 이용할 수 없습니다.



동일조건변경허락. 귀하가 이 저작물을 개작, 변형 또는 가공했을 경우에는, 이 저작물과 동일한 이용허락조건하에서만 배포할 수 있습니다.

- 귀하는, 이 저작물의 재이용이나 배포의 경우, 이 저작물에 적용된 이용허락조건을 명확하게 나타내어야 합니다.
- 저작권자로부터 별도의 허가를 받으면 이러한 조건들은 적용되지 않습니다.

저작권법에 따른 이용자의 권리는 위의 내용에 의하여 영향을 받지 않습니다.

이것은 [이용허락규약\(Legal Code\)](#)을 이해하기 쉽게 요약한 것입니다.

[Disclaimer](#)

이학박사 학위논문

마이크로 채널 내부 염다리 구성을 통한 칩 기반
전류검출법과 고농도 용액에서의 전기전도도
측정에 미치는 전극의 나노다공 구조 효과

**In-Channel Salt Bridge for Amperometric Detection
of Chip Based Capillary Electrophoresis and
Structural Effect of Nanoporous Electrode for
Conductometric Detection at High Ionic Strength**

2015년 2월

서울대학교 대학원

화학부 전기분석화학 전공

강 충 무

A Ph. D. Dissertation

**In-Channel Salt Bridge for Amperometric Detection
of Chip Based Capillary Electrophoresis and
Structural Effect of Nanoporous Electrode for
Conductometric Detection at High Ionic Strength**

By

Chung Mu Kang

Supervisor: Professor Taek Dong Chung

Major: Electroanalytical Chemistry

Department of Chemistry

Graduate School of

Seoul National University

February 2015

ABSTRACT

In-Channel Salt Bridge for Amperometric Detection of Chip Based Capillary Electrophoresis and Structural Effect of Nanoporous Electrode for Conductometric Detection at High Ionic Strength

Chung Mu Kang

Department of Chemistry

The Graduate School

Seoul National University

Electrochemical techniques provide key solutions to the construction of miniaturized systems for bioanalysis, neuroscience, chemical, and environmental analysis. With the rapid developments in nano-electromechanical systems (NEMS) and micro-electromechanical systems (MEMS), electrochemical detection techniques along with electrochemical sample injection, mixing, and preparation have proven to be important components of miniaturized analytical devices. Although various electrochemical detection strategies for miniaturized systems have been proposed, there remain many challenges related to the microchannel-electrode design and electrode material and structure. This dissertation describes

electrochemical strategies for use under strong electric fields for miniaturized analytical devices and a unique conductivity detection method based on a well-defined nanoporous electrode.

Chapter 1 introduces the background and an overview of the challenges related to analytical miniaturized systems. This section particularly focuses on electrochemical detection techniques for analytical microsystems.

In Chapter 2, we propose a novel method for in-channel electrochemical detection under a high electric field using a polyelectrolytic gel salt bridge (PGSB) that is integrated into the middle of the electrophoretic separation channel. The finely tuned placement of a gold working electrode and the PGSB on an equipotential surface in the microchannel provided highly sensitive electrochemical detection without any deterioration in the separation efficiency or interference of the applied electric field. To assess the working principle, the open circuit potentials between gold working electrodes and the reference electrode at varying distances were measured in the microchannel under electrophoretic fields using an electrically isolated potentiostat. In addition, “in-channel” cyclic voltammetry confirmed the feasibility of electrochemical detection under various strengths of electric fields (~ 400 V/cm). Effective separation on a microchip equipped with a PGSB under high electric fields was demonstrated for the electrochemical detection of biological compounds such as dopamine and catechol. The proposed “in-channel” electrochemical detection under a high electric field enables wider electrochemical detection applications in microchip electrophoresis.

Keywords: Microchip, Electrochemical detection, Polyelectrolytic gel salt bridge, Equipotential surface, Electrophoretic field, In-channel

In Chapter 3, we examine electrochemical behavior in a nano-confined space and introduce well-defined nanoporous electrodes to improve conductivity detection for ion chromatography. Nanoporous electrified surface creates unique nonfaradaic electrochemical behavior that is sensitively influenced by the pore size, morphology, ionic strength, and electric field modulation. Here we report the contributions of ion concentration and applied ac frequency to the electrode impedance through electrical double layer overlap and ion transport along the nanopores. The impedance analysis based on the transmission line model revealed the elements of the equivalent circuit such as pore resistance (R_{pore}) and capacitance (C_e), which are characteristic parameters varying with surface morphology as well as ion concentration. Nanoporous Pt with uniform pore size and geometry (L_2 -ePt) was investigated in comparison to Pt black with a dendritic structure and broad distribution of pore size. In spite of similar real surface areas, L_2 -ePt responded more sensitively to conductivity changes in aqueous solutions than Pt black and enabled quantitative conductometry for high electrolyte concentrations, which is difficult in general. The nanopores of L_2 -ePt were more effective to reduce electrode impedance so as to exhibit superior linear responses to not only flat Pt but also Pt black, leading to successful conductometric detection in ion

chromatography without ion suppressor at high ionic strength.

Keywords: Nonfaradaic electrochemical behavior, Surface morphology, Electrical double layer overlap, Pore resistance, Ion concentration, Nanoporous Pt, Ion chromatography

* Most of the parts of this thesis are verbatim reproductions of SCI papers by the author (*Anal. Chem.*, 2012, 84, 901 & *Anal. Chem.*, 2015, in press, DOI: 10.1021/ac504415c).

Student number: 2008-30810

CONTENTS

ABSTRACT	i
CONTENTS	v
LIST OF FIGURES	viii
LIST OF SCHEMES AND TABLES	xvi
CHAPTER 1. GENERAL INTRODUCTION	
1.1. Overview of an Analytical Microsystem	2
1.2. Electrochemical Detection Methods	5
1.3. Electrochemical Detection Using a Nanostructured Electrode	8
CHAPTER 2. IN-CHANNEL ELECTROCHEMICAL DETECTION IN THE MIDDLE OF MICROCHANNEL UNDER HIGH ELECTRIC FIELD	
2.1. Introduction	14
2.2. Experimental	22
2.2.1. Reagents	22
2.2.2. Fabrication of a PGSB Integrated Microchip	22
2.2.3. Electrochemical Cleaning of Contaminated Gold Electrodes	27
2.2.4. Instruments	31
2.2.5. Electrophoresis and Amperometric Detection	33
2.3. Results and Discussion	35

2.3.1. Open Circuit Potential under an External Electric Field	35
2.3.2. Effect of the Bipolar Electrochemical Reaction at the Micro- electrode	37
2.3.3. Inaccuracy of Amperometric Detection	41
2.3.4. Cyclic Voltammetry under Various Electric Fields	43
2.3.5. Separation on a PGSB Integrated Microchip	47
2.4. Conclusions	51

CHAPTER 3. NONFARADAIC NANOPOROUS ELECTROCHEMISTRY FOR CONDUCTOMETRY AT HIGH ELECTROLYTE CONCENTRA- TION

3.1. Introduction	53
3.2. Experimental	58
3.2.1. Reagents	58
3.2.2. Fabrication of Nanoporous Pt	58
3.2.3. Electrochemical Measurements	59
3.2.4. Fabrication of a Nanoporous Pt Integrated PDMS/Glass Chip	60
3.2.5. Ion Chromatography and Conductivity Detection	61
3.3. Results and Discussion	64
3.3.1. Determination of Real Surface Area Using Cyclic Voltammetry	64
3.3.2. Impedance in Various Electrolyte Concentrations	66
3.3.3. Capacitance of Nanoporous and Flat Pts	68
3.3.4. Determination of the Pore Resistance Using TLM	71

3.3.5. Mechanism for Conductometry at Nanoporous Electrode	80
3.3.6. Nonfaradaic Electrochemical Behavior at Nanoporous Electrode ...	85
3.3.7. Conductance Detection Using Nanoporous Electrode	87
3.3.8. Conductance Detection at High Electrolyte Concentration	91
3.4. Conclusions	97
REFERENCES	98
APPENDIX	107
A. Mask Layout	107
B. Microchip Fabrication for Conductivity Detection	109
C. Simulation of Electric Field Gradient Using CFD-ACE+	110
D. Measurement of the Potential Window of the Gold Electrode	111
E. Difference of OCP of the Forward and Reverse Electric Fields	112
F. Test of Ion Leakage through PGSB	113
G. Comparison of the Real Surface Area of the Microelectrodes	114
H. Peak Distortion Effects in Ion Chromatography	115
LIST OF PUBLICATIONS	116
ABSTRACT (in Korean)	117

LIST OF FIGURES

Figure 1-1. Incidence of different levels of miniaturization within the sequential steps of the analytical process. Higher degrees of development are represented by more intense colors in the figure.

Figure 1-2. Recent trends and advances in the electroanalytical chemistry.

Figure 1-3. Applications of nanostructured electrode materials.

Figure 1-4. Schematic of the effect of the morphology of a nanoporous electrode on conductivity detection.

Figure 2-1. Schematic of a capillary electrophoresis system.

Figure 2-2. Interference effects of the CE voltage and current on the electrochemical detector.

Figure 2-3. Effect of applied electrophoretic field on the potential shift in the microchannel.

Figure 2-4. Effect of iR drop on the electrochemical detection in the microchannel.

Figure 2-5. Fabrication of the PGSB on a glass microchip. UV bonding was rapid and allowed the use of a glass chip, which guarantees stability of the electrode. The PGSB was formed by UV exposure immediately after bonding.

Figure 2-6. Optical image of the microchip. (a) Microchip channel dimensions: 80 μm wide, 15 μm deep. Double-T channel dimensions: 80 μm wide, 15 μm deep, and 100 μm injection intersection. PGSB channel dimensions: 120 μm wide, 15 μm deep. Au electrode dimensions: 10 or 20 μm wide. (c) Photograph of the microchip

for in-channel electrochemical detection.

Figure 2-7. Evaluations of the surface areas of the Au electrodes in the microchannel after UV epoxy bonding. Au working electrode width: 10 μm . Cyclic voltammetry was conducted by cycling the potential between 0 and +0.5 V versus Ag/AgCl in a 5 mM $\text{K}_3\text{Fe}(\text{CN})_6$ solution with 100 mM KNO_3 . The scan rate was 50 mV/s.

Figure 2-8. Effect of electrochemical cleaning with 0.5 M H_2SO_4 . Cyclic voltammograms of the Au disk electrode before and after electrochemical cleaning with H_2SO_4 . Cyclic voltammetry was conducted by cycling the potential between 0 and +0.5 V versus Ag/AgCl in a 5 mM $\text{K}_3\text{Fe}(\text{CN})_6$ solution with 100 mM KNO_3 . The scan rate was 50 mV/s.

Figure 2-9. Electrically isolated potentiostat.

Figure 2-10. Open circuit potential difference as a function of the relative position of the Au working electrode and the PGSB under various electrophoretic fields. The Au working electrodes (10 μm wide) were (a) 0 μm , (b) 100 μm , (c) 200 μm , (d) and 400 μm away from the PGSB. The microchannel was filled with 100 mM KNO_3 solution. Inset is a close-up of (a).

Figure 2-11. Effect of bipolar electrochemical reaction on the electrodes under a high electric field. As shown in the images, (a) 60 μm -wide Au electrodes under 250 V/cm are not sufficiently stable to be used as amperometric detectors, and (b) most of the 20 μm -wide Au electrodes are stable under 400 V/cm. Because the Au electrodes near the PGSB are under a much smaller electrophoretic field gradient,

they can be guaranteed to be stable.

Figure 2-12. Predicted potential profile near the PGSB region. The $\Delta\phi_{\text{PGSB}}$ of the PGSB channel should be much smaller than the potential difference elsewhere in the microchannel.

Figure 2-13. Cyclic voltammograms from the Au electrode located in front of the PGSB under CE fields: solid line (0 V/cm), dotted line (200 V/cm), and dashed line (400 V/cm). Cyclic voltammetry was performed in a 1 mM $\text{K}_3\text{Fe}(\text{CN})_6$ solution with 100 mM KNO_3 (supporting electrolyte). Conditions: width of the Au working electrode, 10 μm ; reference electrode, $\text{Ag}/\text{AgCl}/\text{KCl}$ (3 M); counter electrode, Pt wire; scan rate, 100 mV/s.

Figure 2-14. Effect of the distance from the PGSB to the Au working electrode under various electrophoretic fields. (a) Au working electrode 50 μm away from the PGSB. (b) Au working electrode 150 μm away from the PGSB. Au working electrode dimensions: 60 μm wide. Cyclic voltammetry conditions are the same as those for Figure 2-7.

Figure 2-15. Electropherograms of 200 μM $\text{K}_3\text{Fe}(\text{CN})_6$ detected (a) 0 μm and (b) 50 μm from the PGSB. Conditions: CE field strength, -150 V/cm; Au working electrode width, 20 μm ; total length, 1.6 cm; effective length, 1.2 cm; running buffer, 25 mM sodium borate; detection potential, +0.15 V vs $\text{Ag}/\text{AgCl}/\text{KCl}$ (3 M) reference electrode.

Figure 2-16. Electropherograms of dopamine (100 μM) and catechol (150 μM) under high electric fields obtained using the PGSB-integrated microchip.

Conditions: width of the Au working electrode, 20 μm ; total length, 5.4 cm; effective length, 5 cm; running buffer, 25 mM MES; detection potential, +0.05 V vs Ag/AgCl/KCl (3 M) reference electrode.

Figure 3-1. Effect of pore morphology on electrode impedance of the nanoporous electrode.

Figure 3-2. SEM image of nanoporous Pts: (a) L₂-ePt and (b) Pt black. Inset at (a) : TEM image of L₂-ePt.

Figure 3-3. Schematic diagram of the setup used for ion chromatography with microchip-based conductivity detector.

Figure 3-4. Comparison of cyclic voltammograms of the electrodeposited Pt electrodes (L₂-ePt and Pt black) and the flat Pt electrode in 1 M H₂SO₄ at 200 mV/s. MSE denotes mercury sulfate electrode (Hg/Hg₂SO₄). Apparent surface area of working electrode is 0.00001256 cm².

Figure 3-5. (a) Total impedance as a function of concentration for comparison between the nanoporous and flat electrode. (b) Impedance corrected by subtracting solution resistance (R_s) from (a).

Figure 3-6. Electrode capacitance (C_e) of L₂-ePt (■), Pt black (●), and flat Pt (▲) as a function of frequency. 1 mM (open) and 1 M (filled) NaF solutions.

Figure 3-7. Transmission line model for the analysis of electrochemical results from nanoporous materials.

Figure 3-8. Conceptual diagram of relaxation frequency.

Figure 3-9. Predicted charging time of the nanoporous Pt electrodes (L₂-ePt and Pt

black).

Figure 3-10. Bode plots from (a) L₂-ePt, (b) Pt black, and (c) flat Pt in 1 M NaF.

The Z' values in the Bode plots were corrected with the solution resistances. The data in (a,b,c) were fitted based on equivalent circuit with CPE based on TLM (solid line) presented in (d).

Figure 3-11. Mechanism for conductometry at nanoporous electrode. The impedance components in red indicate the elements to which the observed conductance is attributed.

Figure 3-12. Effect of pore connectivity in the nanoporous Pt electrodes (L₂-ePt and Pt black).

Figure 3-13. Effect of pore size in the nanoporous Pt electrodes (L₂-ePt and Pt black).

Figure 3-14. Two cases for nanoporous electrodes in the solution. Dashed line indicates electrical double layer.

Figure 3-15. Ion chromatograms obtained using the L₂-ePt, Pt black and Flat Pt electrodes as a function of frequency (a) 1 kHz, (b) 100 Hz, and (c) 10 Hz under suppressed detection mode: solid line (L₂-ePt), dashed line (Pt black), and dotted line (Flat Pt). Conditions: eluent, 3.5 mM sodium carbonate/1 mM sodium bicarbonate; flow rate, 1.2 mL/min; injection, 25 µL of 1.5 mM F⁻, 1 mM NO₃⁻, and 0.6 mM SO₄²⁻.

Figure 3-16. Electrode impedance as a function of frequency in 1 mM NaF solution.

Figure 3-17. Effect of frequency on moving distance of ion in the nanoporous electrode.

Figure 3-18. Ion chromatograms of synthetic seawater in the suppressed mode when the L₂-ePt (solid line), Pt black (dashed line), and flat Pt (dotted line) electrodes were operated at 1 kHz. Conditions: eluent, 7.5 mM sodium carbonate/1 mM sodium bicarbonate; flow gradient from 1.2 mL/min (0-2 min) to 0.8 mL/min (2-14 min); injection, 5 μ L of 500 mM Cl⁻, 1 mM Br⁻, and 30 mM SO₄²⁻.

Figure 3-19. Ion chromatograms of NaCl brine in the non-suppressed mode from the L₂-ePt, Pt black and flat Pt electrodes at 1 kHz. Conditions: eluent, 7.5 mM sodium carbonate/1 mM sodium bicarbonate; flow rate, 1.5 mL/min; injection, 5 μ L of (a) 30 mM, and (b) 1 M NaCl.

Figure 3-20. Calibration curves of peak areas for concentration of (a) Cl⁻ and (b) Na⁺ in brine solution from the L₂-ePt (solid line), Pt black (dashed line), and flat Pt (dotted line) electrodes. The conditions for ion chromatography are the same as those for Figure 3-19. The error bars are based on the standard deviations from four independent measurements for respective points.

Figure A-1. Mask layout for a PGSB-integrated microchip (chapter 2).

Figure A-2. Mask layout for conductivity detection (chapter 3).

Figure B. Microchip fabrication for an ion chromatography detector. The fabrication process comprises consecutive electrode patterning, oxide layer deposition, development, electroplating, patterned PDMS bonding, and IC-microchip connection formation (Chapter 3).

Figure C. CFD-ACE+ simulation. Channel dimensions: 100 μm wide, 30 μm deep. The parameters of the aqueous solution, such as density and viscosity, were included in this simulation (Chapter 2).

Figure D. *I-V* curves for the gold electrode in the 0.1 M KNO_3 and MES buffer. Conditions: Widths of the Au working electrodes: 20 μm and 40 μm ; reference electrode: Ag/AgCl/KCl (3 M); counter electrode: Pt wire; scan rate: 50 mV/s (chapter 2).

Figure E. Comparison of the open circuit potentials under forward and reverse electric fields. There is little difference between the forward and reverse electrophoretic fields. As stated in the “Instruments” section, the potentiostatic circuit for detection was electrically isolated from the custom-made DC power supply for the electrophoretic field. Repetitive reversals of the applied electrophoretic field between +150 and -150 V/cm showed a voltage change of less than 5 mV in the open circuit potential of the Au electrode, as shown in this figure (Chapter 2).

Figure F. Leakage test of the inner solution and ions in the microchannel. Hardened PGSB (with a negatively charged backbone) has such a high density of fixed charges that it should be able to effectively block the electrolyte solution. We monitored the motion of Rhodamine 6G, which is a cationic fluorescent dye that is in the chamber for the internal filling solution of the reference electrode, into the separation channel through the PGSB. The conclusion was that ion leakage through the PGSB is negligible (Chapter 2).

Figure G. Comparison of the cyclic voltammograms of the electrodeposited Pt microelectrodes (i.e., L₂-ePt and Pt black) and the flat Pt microelectrode in 0.5 M H₂SO₄ at 50 mV/s (Chapter 3).

Figure H. Peak distortion effects under overloaded conditions of sample ions in conventional ion chromatography. Conditions: Eluent: 3.5 mM sodium carbonate/1 mM sodium bicarbonate; flow rate: 1.2 mL/min; injection: 25 µL (Chapter 3).

LIST OF SCHEMES AND TABLES

Scheme 1-1. Schematic diagrams of three different methods for electrochemical detection: (a) End-channel detection, (b) in-channel detection, and (c) off-channel detection. In-channel detection is possible only when using an electrically isolated potentiostat.

Scheme 2-1. Schematic of the PGSB-Integrated microchip. The Au working electrode and polyelectrolytic gel plug, which is electrically linked to the reference electrode system through the internal filling solution, are on an equipotential surface in the channel under an electrophoretic field. The color distribution from red to blue in the channel represents the electrophoretic field gradient that was calculated using computational fluid dynamics (CFD) software, i.e., CFD-ACE+ (CFD Research Corp.). Inset: Schematic representation of the configuration of a PGSB/Au electrode for in-channel amperometric detection on the microchip.

Table 1-1. Relationship between the present analytical demands and technological developments for miniaturization.

Table 2-1. Potential fluctuations at various distances between the PGSB and the working electrodes under a range of electrophoretic fields.

Table 3-1. Impedometric parameters measured from L₂-ePt and Pt black.

CHAPTER 1

GENERAL INTRODUCTION

1.1. Overview of an Analytical Microsystem

Over the past two decades, the need for on-line and automatic measurements using small volumes has been a driving force in many research areas, such as environmental monitoring,^{1,2} biological and biomedical analyses,³ clinical diagnostics,^{4,5} and chemical analysis⁶. The micro total analysis system (μ -TAS), which is also known as a “Lab-on-a-chip,” has been employed to satisfy these demands.⁷ Many of the μ -TAS techniques that have been proposed so far are quite complicated with multiple sample-preparation and analytical-processing steps that are highly interconnected and often automated. Although an analytical device based on a μ -TAS has the advantage of complete and fast analysis in one integrated and automated instrument, there are many critical challenges that still hinder the construction of a real automated μ -TAS, especially with respect to component interfacing, sample handling, separation, and detection methods.

Considering the various steps involved in an analytical process, there are significant difficulties in miniaturization. Analytical processes, such as sample introduction and transportation, chemical reactions, measurements, and data processing, pose particular problems. Even the degree of miniaturization is a crucial issue. Figure 1-1 presents the incidence of different levels of miniaturization within the analytical process of a microsystem. Taking into account the entire analytical process, some of the major obstacles to miniaturization involve the pre-treatment process, such as sample introduction, transportation, and sample handling. In contrast, detection and data processing can be accomplished at a high

degree of miniaturization.

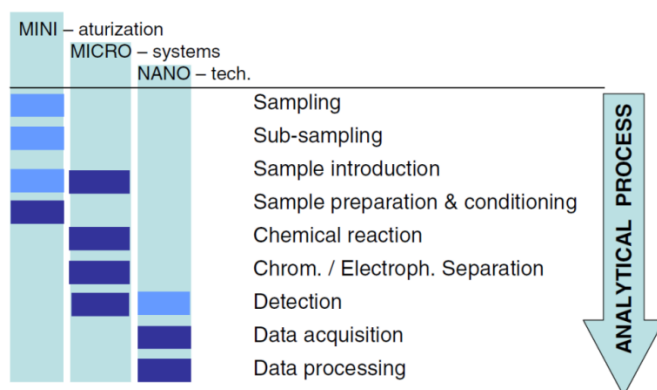


Figure 1-1. Incidence of different levels of miniaturization within the sequential steps of the analytical process. Higher degrees of development are represented by more intense colors in the figure.⁸

Typically, chemical analysis is implemented within the controlled environments of laboratories. However, the results depend not only on whether the instrument is specially made or customized for the purpose, but also on the skill of the users; this is quite evident, for example, in environmental or point-of-care fields. Miniaturization plays a key role in decentralizing chemical analysis. Therefore, a miniaturized analytical system should be comfortable, easy to operate, portable, and reliable.

From a technological perspective, analytical microsystems have some significant potential benefits (Table 1-1). However, on the other hand, there remains a

shortcoming of analytical microsystems that originate from the current technology. Occasionally, it is not possible to achieve real miniaturization of all components, including the electronic and mechanical units. Furthermore, the required technology is not always available.

Table 1-1. Relationship between the present analytical demands and technological developments for miniaturization.⁸

A) GOOD COMPLEMENTARITY	Technological tools
Analytical chemistry demands	• Microelectronic developments
–Low requirements:	• Microfabrication techniques
No skilled personnel	• Microfluidics
No specialized instrumentation	• Chemistry of materials
–Decentralization of analyses:	• Clean-room facilities
Real time	
In situ or on-line	
In vivo	
–Samples:	
Very low volumes	
High throughput	
–Reagents (low consumption)	
–Automation	
B) BETTER TECHNOLOGICAL APPROACHES NEEDED	
–Real world interfaces:	
Sampling and sample introduction	
Incomplete miniaturization	
Sample change between analyses	

Most miniaturized systems require extremely small volumes of sample and reagent (in the pL-nL range). Although this results in some advantages with respect to cost and throughput, there are also several drawbacks, such as suitable detection methods. As a consequence, many studies have concentrated on developing miniaturized and sensitive detection components.⁹ Improving the detection techniques is one of the most important requirements.¹⁰

1.2. Electrochemical Detection Methods

The detection method has been one of the major issues for analytical microsystems because highly sensitive detection techniques are necessary because of the extremely small sample volumes used in miniaturized systems. A wide variety of detection methods can be applied to analytical microsystems.¹¹ Laser-induced fluorescence (LIF) is a primary detection method and is also frequently used in separation-based miniaturized systems because of its inherent high sensitivity.^{9,10} This high sensitivity coupled with the fact that organic and biochemical molecules are sometimes fluorescent is a significant reason for the extensive integration of LIF detection system into microchips. LIF is currently an invaluable detection technique for separation-based microsystems. Nevertheless, the relatively large size, high cost, and high power requirements of the instrument are sometimes unsuitable for μ -TASs. Moreover, non-fluorescent molecules must undergo derivatization before using LIF. The primary alternative to LIF detection method is, undoubtedly, electrochemical detection, which is suitable because of its inherent ease of miniaturization and high compatibility with micro/nanofabrication techniques.

The interest in the use of electrochemical detection for analytical microsystems has increased dramatically because the method offers several powerful advantages for analytical microsystems, such as low detection limits, low power requirements, high selectivity, great compatibility, good portability, low cost, and miniaturization without any loss in sensitivity. Confirmation of the key role of the electrochemical detection method has been published in various reviews^{12,13} and other reports.¹⁴

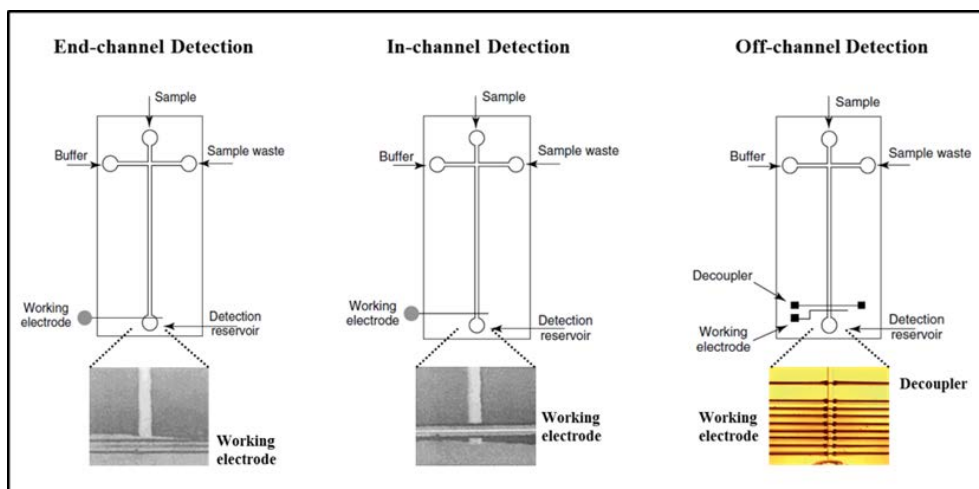
The major problem in coupling analytical microsystems (especially electric field-driven systems) with electrochemical detection is interference between the high voltage used in the electrophoresis-based separation and the detection potential. Three schemes have been proposed for electrochemical detection: End-channel, in-channel, and off-channel (Scheme 1-1).

End-channel electrochemical detection involves a working electrode that is positioned just outside the microchannel. The high electric field exerts minimal interference on the potential applied in the electrochemical detector because most of the potential drop occurs across the microchannel.

In-channel electrochemical detection requires that the electrode is located directly in the microchannel, which involves alignment of the working electrode at the very end of the microchannel with an electrically isolated potentiostat.

Off-channel electrochemical detection entails the application of a decoupler (i.e., an electrode or a hole) to the electrophoretic field before it reaches the working electrode of the detector. In principle, the decoupler shunts the high voltage required for separation to ground and creates an electrophoretic field-free area where the sample plugs are pushed over the working electrode by the electro-osmotic flow, which is generated prior to the decoupler.

Aside from electrochemical detection and LIF, there are other detection methods for analytical microsystems. However, in terms of practicality, they are much less developed than those mentioned above.



Scheme 1-1. Schematic diagrams of three different methods for electrochemical detection: (a) End-channel detection, (b) in-channel detection, and (c) off-channel detection. In-channel detection is possible only when using an electrically isolated potentiostat.

In practical terms, this dissertation focuses on a new method for electrochemical detection and proposes a fundamental solution that enables electrochemical detection at any point in the microchannel under a high electric field (Chapter 2).

1.3. Electrochemical Detection Using a Nanostructured Electrode

Over time, material science research began to remarkably deepen our understanding of how electrode materials can be reproducibly prepared.¹⁵ Since the 1960s, platinum, gold, silver, carbon, and other solid electrodes have become increasingly widespread as electroanalytical tools. With the more recent advances in nanomaterial science, chemical sensors and other analytical applications have taken advantage of the unique characteristics of nano-architected electrodes¹⁶ based on nanoparticles,¹⁷ carbon nanotubes,¹⁸ graphene,¹⁹ and electrodeposited materials^{20,21} for high-sensitivity analysis.

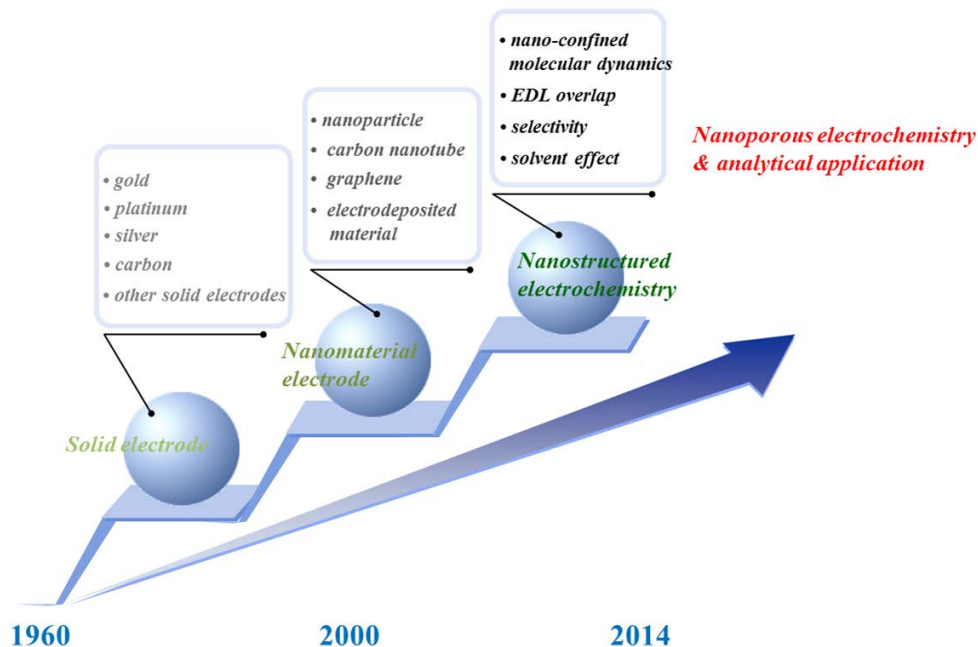


Figure 1-2. Recent trends and advances in the electroanalytical chemistry.

Nanostructured electrodes have attracted increasing interest for a wide range of applications, including catalysis,²² electrocatalysis,²³ energy conversion, and storage systems (batteries,²⁴ supercapacitors,²⁵ fuel cells,^{26,27} dye-sensitized solar cells,²⁸ etc.), electrochemical sensors,²⁹ biosensors,³⁰ neural probes,³¹ separation systems,³² and many more.

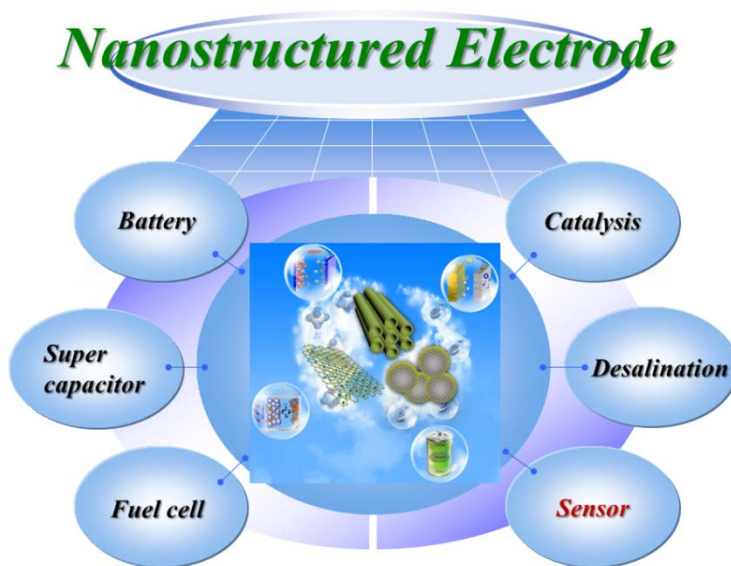


Figure 1-3. Applications of nanostructured electrode materials.

Research on nanoporous electrochemistry was recently diverted from the effect of enlarged surface areas to the unusual electrochemical features originating from the geometry of nanopores. The conditions experienced by a reactant molecule in a nano-confined space surrounded by an electrified surface should be different from

those experienced by a molecule in bulk solution. The nanoconfined molecule should reside in the vicinity of the electrode surface and should not be allowed to escape. By assuming the free diffusion of a molecule undergoing negligible adsorption, we can predict its highly frequent encounters with the electrode surface, which result in an enhanced rate of electrochemical reactions.^{33,34} Such a confined space for electrochemical reactions also accounts for an electrical double layer (EDL) overlap and the transport of ions along a nanochannel.³⁵ The novel phenomena arising from the nanoporous morphology are sensitive functions of the chemical components and their concentrations. This leads us to expect a major potential application of nanoporous electrochemistry to new analytical methods. By understanding the electrochemical aspects of nanoporous electrodes, we can seek unprecedented advances in electroanalysis.

Nanoporous Electrode

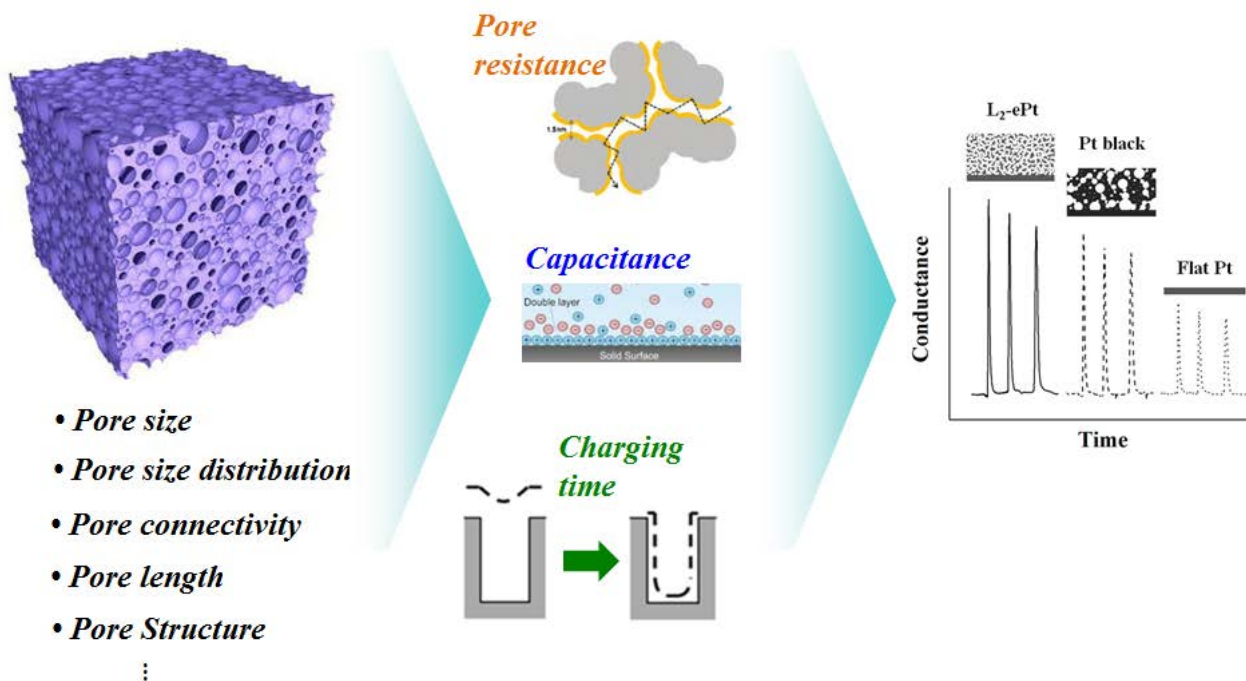


Figure 1-4. Schematic of the effect of the morphology of a nanoporous electrode on conductivity detection.

Conductometry is an inexpensive, nondestructive, and simple way to detect small inorganic ions that lack electrochemical activity and spectroscopic characteristics that are usually detected by conventional methods, e.g., fluorescence.³⁶ The general limitation of conductometry is the difficult detection of ions at high electrolyte concentrations because a change in the solution resistance is hardly distinctive in a low total impedance. That is why the maximum concentration of the dynamic range in most conductometric detectors does not exceed several tens of millimoles per liter.³⁷ This problem is enhanced at small electrodes: they reduce the contribution of the solution resistance compared to the impedance near the electrode, which prohibits the miniaturization of conductometric detectors.

In this dissertation, three electrodes (i.e., L₂-ePt, Pt black, and flat Pt) are used to investigate the effect of the morphology of the electrode and applied in conductivity detectors for ion chromatography (Chapter 3).

CHAPTER 2

IN-CHANNEL ELECTROCHEMICAL DETECTION IN THE MIDDLE OF MICROCHANNEL UNDER HIGH ELECTRIC FIELD

2.1. Introduction

Over the past decade, microchip electrophoresis (MCE) has emerged as an attractive method for chemical and biological analysis using miniaturized systems.³⁸⁻⁴⁰ With the aim of enabling nonexperts to carry out ubiquitous analysis, recent applications of microfluidic chip-based analytical tools tend toward the integration of multiple unit processes such as sample pretreatment, separation, and detection into a single chip.^{41,42} Of the necessary elements for portable systems, the detection technique is key for a high-performance separation-based system with low detection limits, fast analysis, high throughput, low cost, disposability, and portability.^{43,44} A detector that can be truly miniaturized would offer immeasurable benefits for chip-based analytical tools.

Many attempts to incorporate detection methods such as Fourier transformation of infrared light absorption spectra (FTIR), Raman scattering, nuclear magnetic resonance (NMR), refractive index (RI), thermal lens microscopy (TLM), microplasma-optical emission spectroscopy (OED), surface plasmon resonance (SPR), electrochemical analysis (EC), chemiluminescence (CL), mass spectrometry (MS), UV–vis absorbance (UV–vis), and laser induced fluorescence (LIF) into electrophoresis devices have been reported.⁴⁵⁻⁴⁷ In particular, much attention has been focused on MS, LIF, UV–vis, and EC because of their compatibility with the capillary electrophoresis (CE) technique without a significant loss in detection quality.

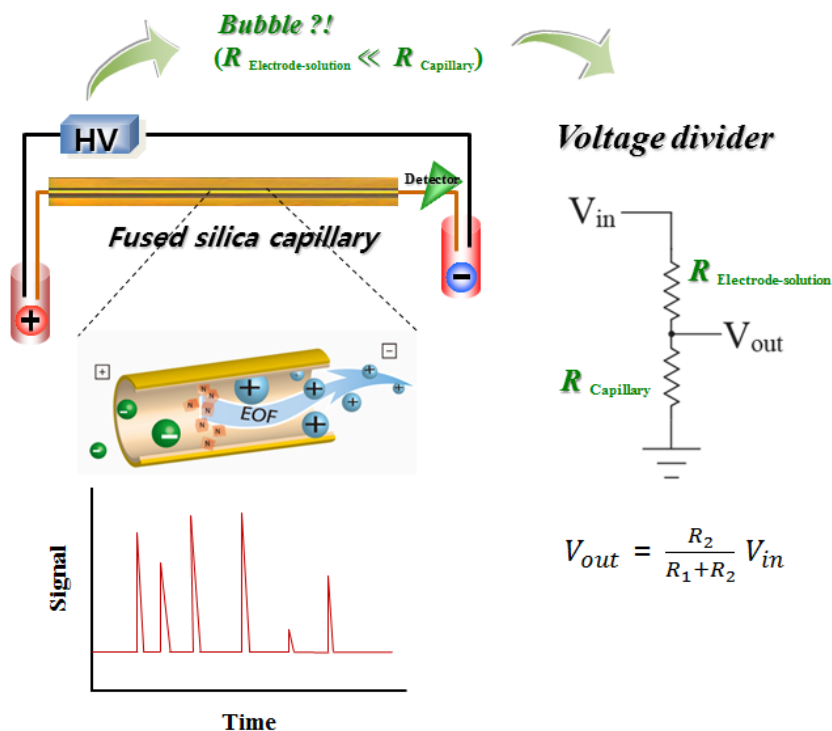


Figure 2-1. Schematic of a capillary electrophoresis system.

Although the majority of commercial CE instruments employ UV–vis absorbance, this method is unsuitable for trace chemical analysis in the nanomolar or below-nanomolar concentration range due to its inherently poor detection limit.⁴⁸ MS detection reportedly offers high throughput in conjunction with the MCE;⁴⁹ however, it is expensive and usually not portable. LIF is a common detection method that allows extremely sensitive detection in combination with a MCE.^{50,51} However, it is necessary to select natural fluorescent compounds which must be derivatized with a fluorophore to perform a LIF method. The EC detection method

comprises very simple instrumentation and integration of microscale electrodes onto a microchip,⁵² while maintaining excellent sensitivity and selectivity.⁵³ As a result, it has been intensively employed as the ideal detection method in microfluidic on-chip separation systems.⁵⁴ The largest challenge with respect to EC detection is the influence of the high CE voltage and current on the detector, which causes severe noise and can make electrochemical detection impossible.⁵⁵⁻⁵⁷ Furthermore, an electrical surge may critically damage the EC detector.⁵⁸

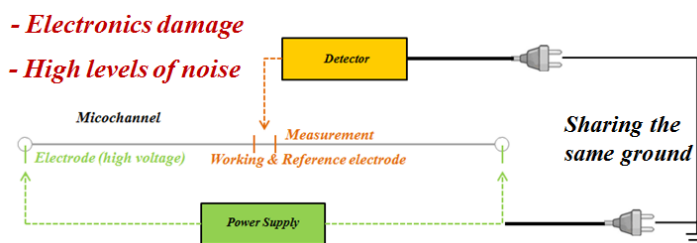


Figure 2-2. Interference effects of the CE voltage and current on the electrochemical detector.

Amperometric detection methods are classified into end-channel and in-channel types, depending on the position of the working electrode in a microchannel.⁵⁹ End-channel detection is a facile method to measure redox current from analytes that reduces the influence of the CE voltage and current. Woolley et al.⁶⁰ proposed end-channel detection on a microchip that was placed in a gradually widening separation channel just before the working electrodes in order to minimize the interference of the CE field. However, measuring the electrochemical current near

the outlet of the channel induces a shift in the half-wave potential of the redox couple, which results in poor reproducibility due to the sensitivity toward the relative position of the working electrode and the channel outlet under the CE field.

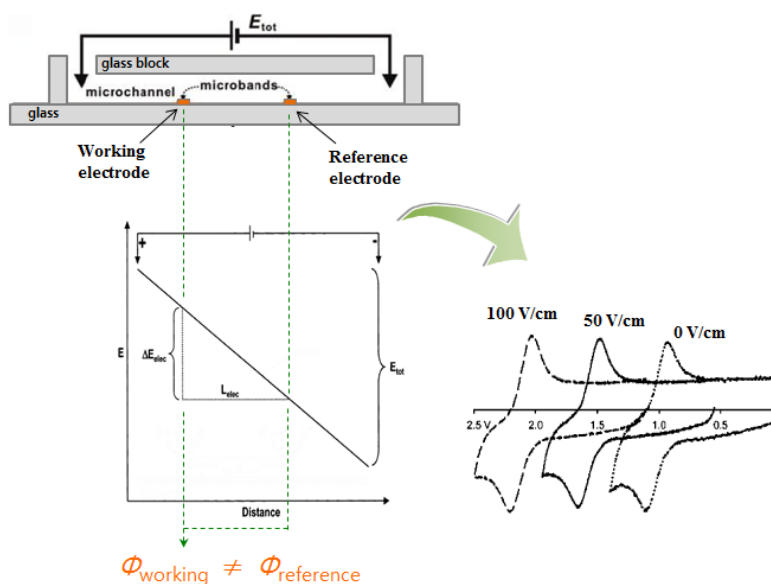


Figure 2-3. Effect of applied electrophoretic field on the potential shift in the microchannel.

To solve this problem, Wang et al.⁶¹ developed an end-channel detection method called the “wall-jet,” which maintains specific distance between the separation channel and the working electrode. However, the structure of the separation channel connected to the perpendicular detector strip limits the miniaturization and versatility of the microchip. Although end-channel detection provides a method to

measure EC current under a CE field, it still has a few practical problems including sample plug dispersion, which causes peak broadening and affects separation efficiency. Ertl et al.⁶² improved end-channel detection by focusing a sample plug with a sheath-flow supported microchip. However, the creation of sheath-flow channels increases the complexity of the channel design. Several theoretical and experimental strategies to measure the redox current from analytes within a separation channel have been reported.⁶³⁻⁶⁵ Martin et al.⁶⁶ reported a design with the working electrode aligned at the very end of, but still inside, the separation channel. However, this in-channel arrangement demands precise alignment of the working electrode in the separation channel to minimize the shift of the half-wave potential and electrochemical noise. Chen et al.⁶⁷ proposed in-channel detection to eliminate the potential shift using a dual channel configuration; however, the working and reference electrodes must be placed as close as possible to the counter electrode, which is located at the channel outlet, to minimize iR drop.

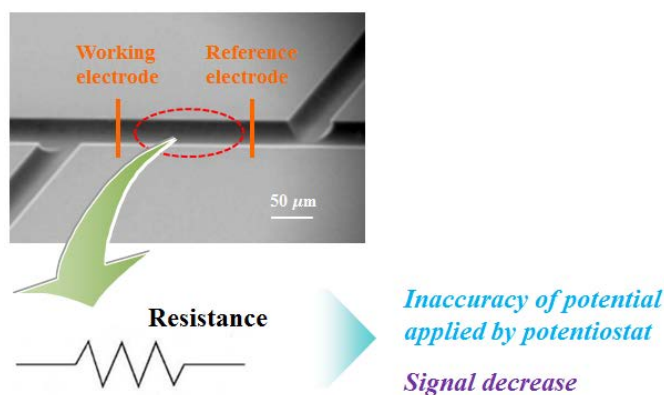


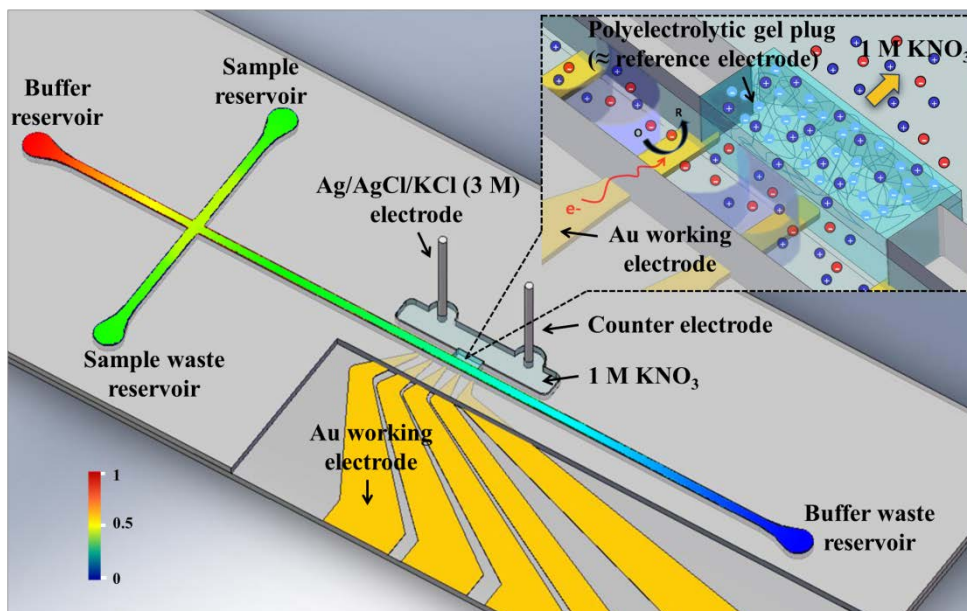
Figure 2-4. Effect of iR drop on the electrochemical detection in the microchannel.

In addition, the dual-channel in this detection scheme requires complex channel design that hinders the simplification of chip patterns and makes integration of other components onto the same chip difficult.

The decoupling approach is another strategy to isolate the amperometric signals from the CE field and eliminate the diffusive band-broadening that is observed in the end-channel strategies. Rossier and co-workers⁶⁸ reported the integration of a decoupler composed of a microhole array located perpendicular to the separation channel. Chen et al.⁶⁹ utilized a palladium metal electrode as a decoupler to effectively dissipate the hydrogen bubbles. Although these decoupling methods for in-channel detection offer another effective way to isolate the EC detector from the separation field and suppress the band broadening that is characteristic of end-channel methods, band dispersion still exists due to the rapid decrease of the electric field strength between the decoupler and working electrode.⁷⁰ Another approach that employs bipolar electrochemistry^{71,72} is an in-channel detection method without a decoupler. However, the amperometric detection method-based bipolar electrochemistry,^{73,74} which controls the potential of the working electrode by adjusting the bipolar electrode size, electrode gap, or the electric field strength, is not appropriate for the detection of redox-active analytes with different redox potentials.

In this study, we propose a new strategy that allows in-channel detection by the placement of a novel polyelectrolytic gel salt bridge (PGSB) between the reference and working electrodes on the equipotential surface of the separation channel

(Scheme 2-1). This in-channel method is particularly suitable for MCE for the following reasons: (i) In-channel detection is easily accomplished without a decoupler. (ii) The generation of PGSB by UV exposure is very simple and, thus, the PGSB can be placed anywhere in the separation channel. (iii) The electrically isolated detector obviates damage to the electronics, thereby minimizing potential fluctuation at the working electrode. (iv) The placement of the working electrode in the separation channel allows for high separation efficiency by eliminating the band-broadening that is observed when end-channel detection is used. (v) The placement of the working and reference electrodes on an equipotential surface substantially reduces the shift of the half-wave potential and the background noise; therefore, a constant potential can be applied to the working electrode even under varying and possibly fluctuating CE fields.



Scheme 2-1. Schematic of the PGSB-Integrated microchip. The Au working electrode and polyelectrolytic gel plug, which is electrically linked to the reference electrode system through the internal filling solution, are on an equipotential surface in the channel under an electrophoretic field. The color distribution from red to blue in the channel represents the electrophoretic field gradient that was calculated using computational fluid dynamics (CFD) software, i.e., CFD-ACE+ (CFD Research Corp.) (Figure C). Inset: Schematic representation of the configuration of a PGSB/Au electrode for in-channel amperometric detection on the microchip.

2.2. Experimental

2.2.1. Reagents

A 2.5 M aqueous solution of 2-acrylamido-2-methyl-1-propanesulfonic acid (AMPSA) was used in combination with 1% 2-hydroxy-4'-(2-hydroxyethoxy)-2-methylpropiophenone as a photoinitiator and 0.5% N,N'-methylenebisacrylamide as a cross-linker to fabricate the polyelectrolytic gels. A solution of 3-(trimethoxysilyl)propyl methacrylate (TMSMA) in anhydrous methanol was used as the coating material for adhesion of the polyelectrolytic gels onto the surface of the channels. Stock solutions of varying concentrations of potassium ferricyanide in 100 mM potassium nitrate were prepared as a supporting electrolyte for potentiometric measurements. The electrophoresis buffer solution of the potassium ferricyanide was 25 mM sodium borate. A solution containing neurotransmitters such as dopamine and catechol was prepared in a 25 mM 2-(N-morpholino)ethanesulfonic acid (MES) buffer solution with a pH of 6.5. All the reagents were purchased from Sigma-Aldrich (USA).

2.2.2. Fabrication of a PGSB Integrated Microchip

The MCE device depicted in Figure 2-5 was fabricated using traditional photolithographic techniques, UV epoxy bonding, and novel photopolymerization of the polyelectrolytic gel plug by UV exposure. The patterning of the channel and the Au electrode were prepared similarly to our previous work.^{75,76} In brief, for the

formation of the microchannel pattern, a glass cover slide (Cat. No. 1000412, Paul Marienfeld GmbH & Co. KG, Germany) was initially cleaned using a piranha solution ($\text{H}_2\text{SO}_4/\text{H}_2\text{O}_2 = 3:1$). (Caution: The piranha solution should be handled with extreme care because it is a powerful oxidizing agent that reacts violently with organic compounds.) Photoresist (AZ4620, Clariant, Switzerland) was spin-coated at 7000 rpm for 30 s onto the glass slide. It was then sequentially treated with photolithography procedures including soft baking, UV exposure, development, hard baking, and wet etching.

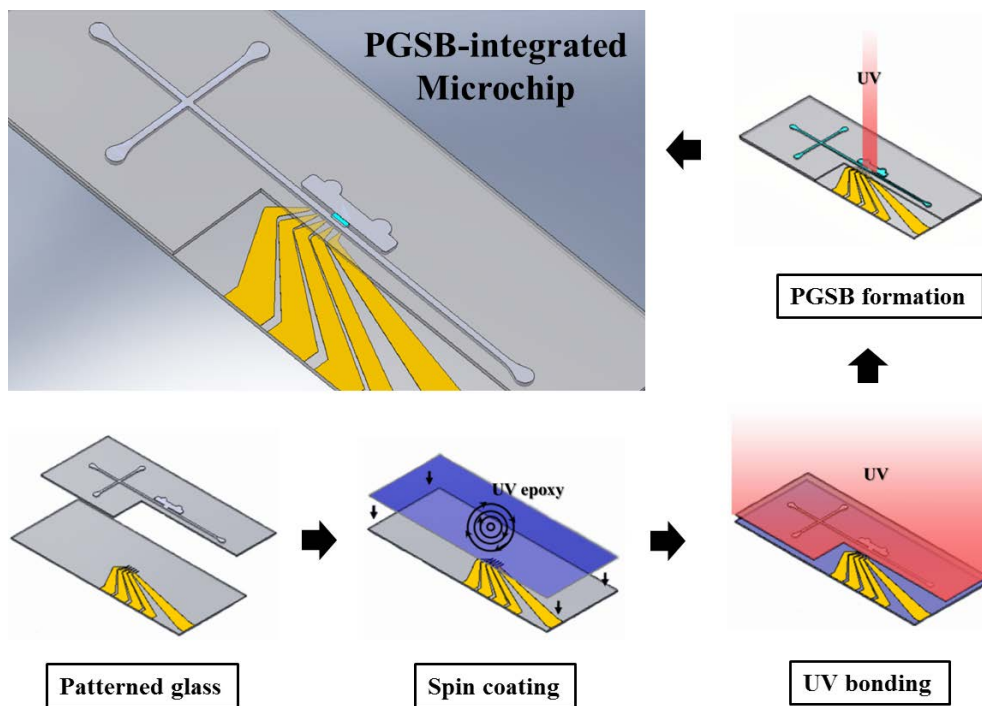


Figure 2-5. Fabrication of the PGSB on a glass microchip. UV bonding was rapid and allowed the use of a glass chip, which guarantees stability of the electrode. The PGSB was formed by UV exposure immediately after bonding.

A similar photolithographic protocol was applied to prepare the bottom glass slide. After cleaning the glass slide with the piranha solution and coating it with hexamethyldisilazane (HMDS; Clariant, Switzerland), AZ5214 (Clariant, Switzerland) was spin-coated at 4000 rpm for 30 s. Prebaking for 1 min at 100 °C was followed by a first exposure for 5 s at 17 mJ/cm², reversal baking for 5 min at 100 °C, flood exposure for 20 s at 17 mJ/cm², and development using AZ300MIF (Clariant, Switzerland). Metal films were sputtered on the patterned glass using a DC/RF magnetron sputter (Atek, Korea). An adhesion layer of titanium (Ti) was sputtered to a thickness of approximately 350 Å. A gold (Au) film 5000 Å thick and 10 or 20 µm wide was deposited at 5 Å/s onto the Ti layer. The Au-patterned glass was then immersed into acetone (J.T. Baker, USA) to remove the remainder of the patterned Au/Ti layer. UV exposure was used for the subsequent bonding procedure and PGSB integration. After cleaning with piranha solution and air blowing, the Au electrode pattern was spin-coated with a UV curing resin (LOT No. A10K01, ThreeBond Co., Ltd., Japan) at 1500 rpm for 30 s. The substrate was exposed to 365 nm UV light for 12 s at 17 mJ/cm². An optical image of the microchip is shown in the Figure 2-6. The microchip consists of a channel-patterned glass substrate and an Au-deposited glass substrate. Au electrodes are available in many different sizes for electrochemical research under various CE field conditions in addition to the electrode dimensions shown in Figure 2-6.

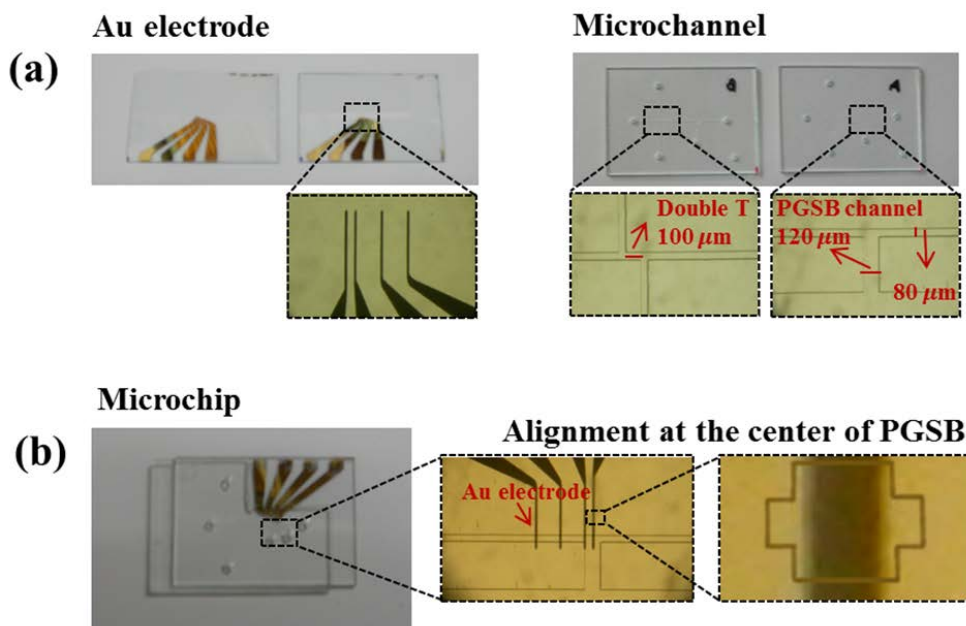


Figure 2-6. Optical image of the microchip. (a) Microchip channel dimensions: 80 μm wide, 15 μm deep. Double-T channel dimensions: 80 μm wide, 15 μm deep, and 100 μm injection intersection. PGSB channel dimensions: 120 μm wide, 15 μm deep. Au electrode dimensions: 10 or 20 μm wide. (c) Photograph of the microchip for in-channel electrochemical detection.

2.2.3. Electrochemical Cleaning of Contaminated Gold Electrodes

The channels were flushed with acetone for 30 s. The bottom glass slide was electrochemically cleaned by cycling the potential between +1.0 and +0.2 V in 0.5 M H₂SO₄ using an Ag/AgCl and a Pt wire as the reference and counter electrodes, respectively. The final chip was prepared by bonding the cover and bottom glass slides. After cleaning with H₂SO₄, the surface areas of the Au electrodes that were exposed in the microchannel were experimentally checked to confirm that the Au thin film was stable as an electrode. The surface areas of the Au electrodes exposed to the inner wall in the channel were investigated via the cyclic voltammetric limiting current (i_{lim}) in a 5 mM K₃Fe(CN)₆ solution and found to be consistent with the areas measured by the video microscope system (ICS-305B, Sometech, Korea). According to the model of the microband electrode,⁷⁷

$$i_{\text{lim}} = \frac{2\pi n F D C l}{\ln(64 D t / w^2)}$$

where n is the number of electrons transferred, F is the Faraday constant, D is the diffusion coefficient, l is the microband length, w is the microband width, t is the current time, and C is the bulk concentration of the electroactive species. Figure 2-7 shows the cyclic voltammograms obtained in a 5 mM K₃Fe(CN)₆ solution with 100 mM KNO₃ as the supporting electrolyte. The Au electrode areas calculated from the i_{lim} values were consistent with those measured from the video images.

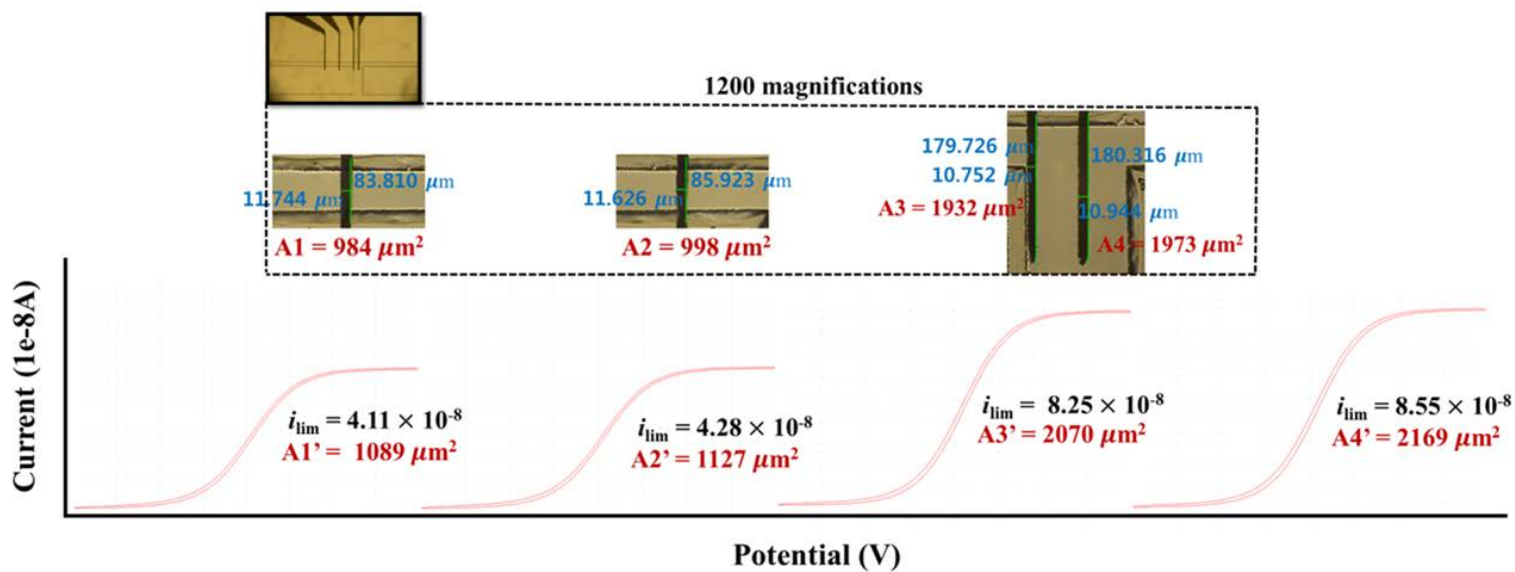


Figure 2-7. Evaluations of the surface areas of the Au electrodes in the microchannel after UV epoxy bonding. Au working electrode width: 10 μm . Cyclic voltammetry was conducted by cycling the potential between 0 and +0.5 V versus Ag/AgCl in a 5 mM $\text{K}_3\text{Fe}(\text{CN})_6$ solution with 100 mM KNO_3 . The scan rate was 50 mV/s.

The PGSB in the channel was fabricated using UV exposure. In brief, the channels in the microfluidic chip were filled with 0.1 M TMSMA solution and stored at room temperature for 20 min. Before being washed with anhydrous methanol and filled with a 2.5 M AMPSA monomer solution, the microfluidic chip was exposed to UV light through a photomask for 35 s at 17 mJ/cm^2 . Finally, the Au surface was electrochemically polished by cycling the potential between +1.0 and +0.2 V versus Ag/AgCl in 0.5 M H_2SO_4 until reproducible cyclic voltammograms were obtained. To confirm the effect of cleaning the Au electrode surface with H_2SO_4 , the electrochemical behavior was checked using a TMSMA-modified gold substrate as the control. The surface treatment was performed as follows: An Au disk electrode (radius: 3 mm) was cleaned with piranha solution and then soaked in a 0.1 M TMSMA solution for 20 min. After coating with TMSMA, the electrode was stored in a 2.5 M AMPSA monomer solution for 10 min. The cyclic voltammogram of the cleaned Au disk electrode is remarkably consistent with that of the bare Au disk electrode because of cleaning with H_2SO_4 . Thus, the results shown in Figure 2-8 suggest that a chemical-contaminated Au electrode can be effectively cleaned electrochemically with H_2SO_4 .

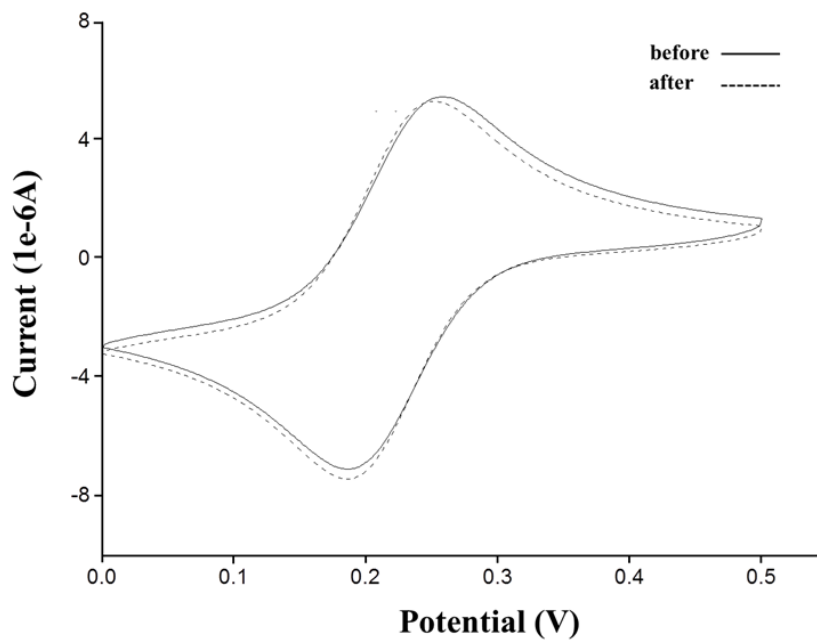
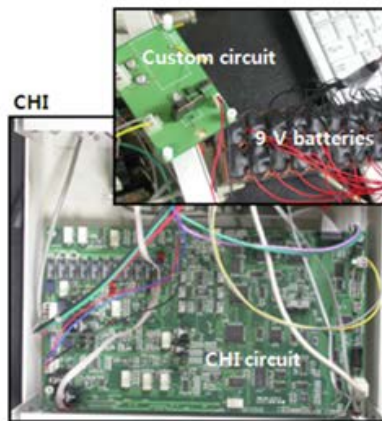


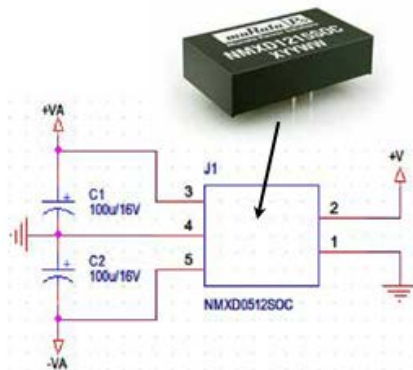
Figure 2-8. Effect of electrochemical cleaning with 0.5 M H_2SO_4 . Cyclic voltammograms of the Au disk electrode before and after electrochemical cleaning with H_2SO_4 . Cyclic voltammetry was conducted by cycling the potential between 0 and +0.5 V versus Ag/AgCl in a 5 mM $\text{K}_3\text{Fe}(\text{CN})_6$ solution with 100 mM KNO_3 . The scan rate was 50 mV/s.

2.2.4. Instruments

Electrochemical examination of the Au electrodes on the chip was carried out using a conventional potentiostat (Model CHI660A, CH Instruments Inc.) with an Ag/AgCl electrode and a Pt wire as the reference and counter electrodes, respectively. A DBHV-100 high voltage supplier (Digital Bio Technology, Korea) driven by a six-channel voltage control program, which was written using LabVIEW software version 8.2 (National Instruments, Austin, TX), was used for electrophoresis. The potentiostat was isolated from the external electric outlet by a custom-made DC power supplier that converted from DC 9 V batteries to DC +5, +15, and -15 V to match the output voltages of the internal power module of the Potentiostat (Figure 2-9). Amperometric detection was performed in a Faraday cage equipped with a picoamp booster (Model CHI200, CH Instruments Inc.).



Dual Output DC/DC Converters



3-terminal Integrated Switching Regulators

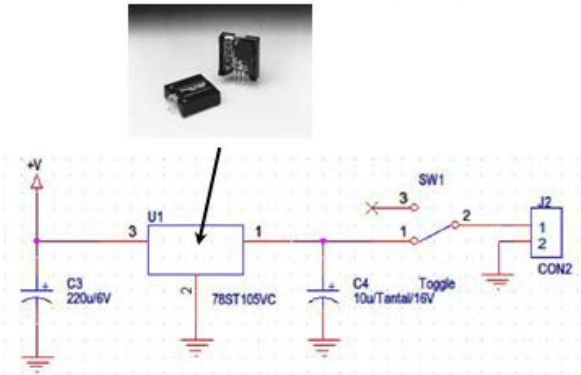


Figure 2-9. Electrically isolated potentiostat.

2.2.5. Electrophoresis and Amperometric Detection

To optimize the surface condition of the microchannels, the glass chip channel was treated according to the following procedure. First, the channel was rinsed with deionized water, 0.1 M HCl, 0.1 M NaOH, and 25 mM $\text{Na}_2\text{B}_4\text{O}_7$ (or 25 mM MES) for 10 min each. The effect of the position of the Au working electrode relative to the PGSB was evaluated by through electrophoretic separation of the ferricyanide species. A 200 μM potassium ferricyanide solution was placed in the sample reservoir and loaded in the pinched injection mode by applying +150 V to the sample waste reservoir for 20 s; the sample reservoir was grounded while both the buffer and waste reservoirs were floating. For sample injection and separation, voltages of +250 and +100 V were applied to the buffer–waste reservoir and the sample reservoir/ sample–waste reservoir, respectively, and the buffer reservoir was grounded. The detection potential of +0.15 V (vs an Ag/AgCl/KCl (3M) reference electrode located in the chamber beyond the PGSB, as shown in Scheme 2-1) was applied to the Au working electrode during the separation.

To ensure successful electrophoresis and amperometric detection under the high electric field, two biological compounds, i.e., 100 μM dopamine and 150 μM catechol, were mixed in a 25 mM MES buffer. Similar to the method that was used to load and separate ferricyanide, pinched injection was employed to load the sample plug by applying +150 V between the sample and the sample waste reservoir for 20 s. The separation was carried out under a variety of electric fields

(50–500 V/cm).

2.3. Results and Discussion

2.3.1. Open Circuit Potential under an External Electric Field

The open circuit potential (OCP) between the Au working electrodes and the PGSB was measured under various electric fields. Figure 2-10 shows the OCP data obtained with spaces of -0, 100, 200, and 400 μm between the Au working electrodes and the PGSB. The electric field gradient (ΔV_s) applied along the microchannel for electrophoretic separation varied from 30 to 400 V/cm. The OCP data was obviously dependent on the ΔV_s as well as the distance between the Au working electrode and the PGSB. The OCP increased with increasing ΔV_s and distance. This result indicates that there are critical problems that need to be solved in order to perform electrochemical detection using electrodes in the middle of a microchannel with a high electric field for electrophoresis.

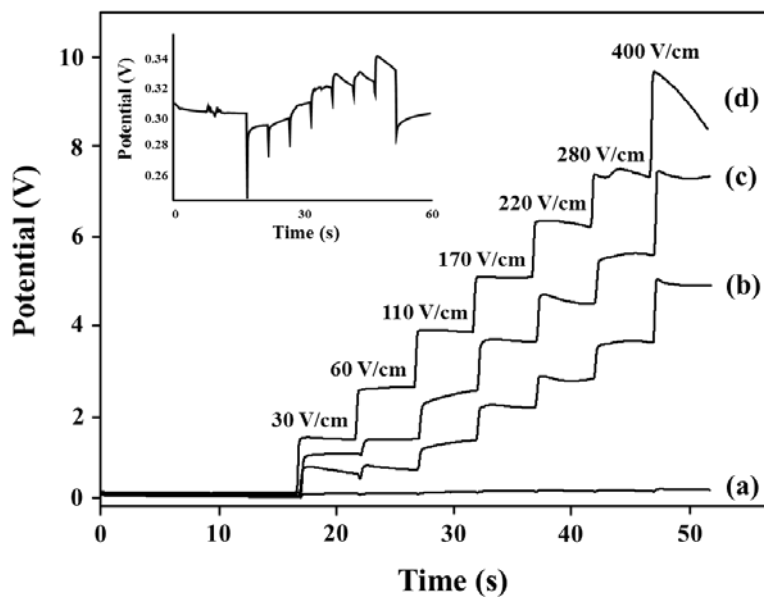
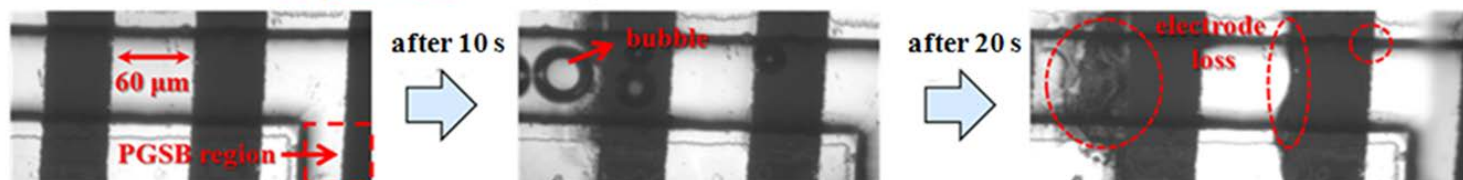


Figure 2-10. Open circuit potential difference as a function of the relative position of the Au working electrode and the PGSB under various electrophoretic fields. The Au working electrodes (10 μm wide) were (a) 0 μm , (b) 100 μm , (c) 200 μm , (d) and 400 μm away from the PGSB. The microchannel was filled with 100 mM KNO_3 solution. Inset is a close-up of (a).

2.3.2. Effect of the Bipolar Electrochemical Reaction at the Microelectrode

There are two major problems: (1) The bipolar disparity of the electrochemical potential on the electrode and (2) the inaccurate amperometric detection. The first issue is highly related to the bipolar effect that is observed when an electrode is exposed to a steep electric field gradient. This bipolar electrode behavior⁷⁸⁻⁸⁰ may distort electrochemical signals from the electrode and harm the working electrode surface (Figure 2-11). A steep gradient of the external electric field in the solution phase may lead to considerable disparity in the electrochemical potential between the ends of an electrode (ΔV_{edge}). However, the Fermi level throughout the electrode is not expected to be significantly affected by the field gradient. This disparate electrochemical potential on the electrode surface is a function of the width and position of the electrode on the microfluidic chip. A larger ΔV_{edge} is observed for wider electrodes that are further from the PGSB in the narrow microchannel. The maximum voltage, applied to the microchannel for electrophoretic separation, is restricted by the condition that no wireless electrochemical reaction should take place due to the external electric field gradient. To satisfy this condition, ΔV_{edge} should be lower than the electrochemical potential window for a given solution and electrode material.

(a) Au electrode (60 μm wide), electrophoretic field (250 V/cm)



(b) Au electrode (20 μm wide), electrophoretic field (400 V/cm)



Figure 2-11. Effect of bipolar electrochemical reaction on the electrodes under a high electric field. As shown in the images, (a) 60 μm -wide Au electrodes under 250 V/cm are not sufficiently stable to be used as amperometric detectors, and (b) most of the 20 μm -wide Au electrodes are stable under 400 V/cm. Because the Au electrodes near the PGSB are under a much smaller electrophoretic field gradient, they can be guaranteed to be stable.

The potential window is determined via a cyclic voltammogram obtained in the absence of the electric field gradient in the solution. For example, an electric field with a strength of 400 V/cm causes a maximum difference of 0.4 and 0.8 V between the edges of 10 and 20 μm wide Au electrodes, respectively. Because the potential window of the Au electrode in the 0.1 M KNO_3 and MES buffer employed in this study is wider than 1 V (Figure D), the electrochemical reaction on the Au electrode due to the external electric field required for electrophoretic separation would be negligible. Moreover, as Figure 2-12 illustrates, the electric potential gradient is expected to be minimal in front of the PGSB, which is connected to a reference electrode system with a very low resistance. The reduction of the electric potential gradient near the PGSB leads to a minimal bipolar effect, i.e., suppression of ΔV_{edge} , if the electrode is positioned just in front of the PGSB. This was confirmed by the significant reduction in OCP fluctuation, as shown in Figure 2-10a. This result was virtually the same as that obtained under reverse electric fields (Figure E).

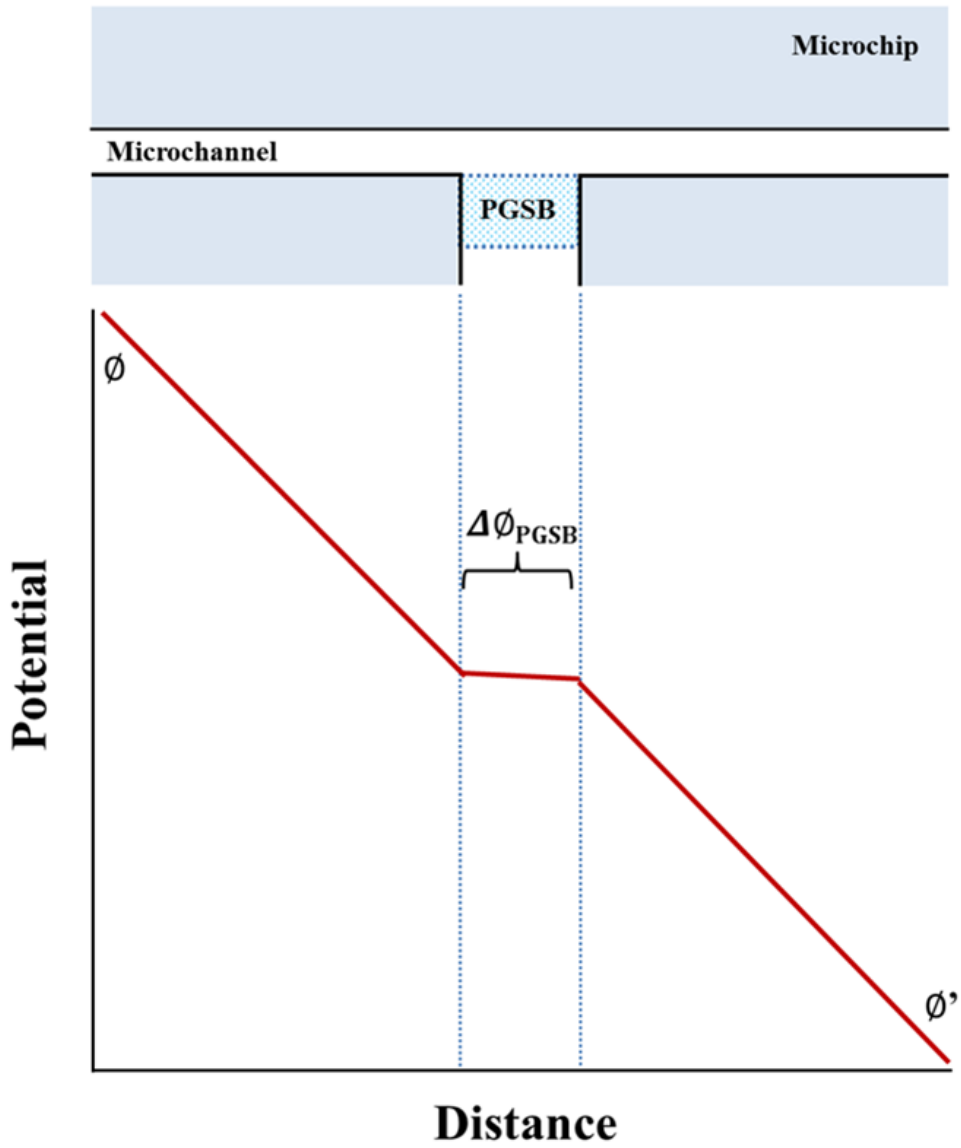


Figure 2-12. Predicted potential profile near the PGSB region. The $\Delta\phi_{\text{PGSB}}$ of the PGSB channel should be much smaller than the potential difference elsewhere in the microchannel.

2.3.3. Inaccuracy of Amperometric Detection

The other problem is the accuracy of the electrochemical potential that is applied to the Au electrode for amperometric detection. This is also a function of ΔV_{edge} and the potential drop between the electrode and the PGSB. It is evident that a higher resistance between the working and the reference electrodes under a steeper external electric field would produce a larger potential drop along the solution in the microchannel.⁸¹ Therefore, it is necessary to tune the position of the working electrode with respect to the PGSB for successful amperometric detection during electrophoresis on a microchip. Practically, the potential shifts between the working and reference electrodes that are caused by ΔV_s in the microchannel can be calibrated using a hydrodynamic voltammogram.⁸² However, the position within the microchannel that is significantly away from the PGSB is still problematic. First, the electrochemical potential is unavoidably affected by the ΔV_s , which is normally on a much larger scale than the potential difference applied between the working and reference electrodes for amperometric detection. Even a tiny fluctuation in ΔV_s can result in a severe shift in the electrochemical potential for amperometric detection. Moreover, this system is also affected by the bipolar effect, i.e., ΔV_{edge} . Due to the significantly reduced electric potential gradient near the PGSB, the electrode just in front of the PGSB is predicted to be on an almost equipotential surface with the PGSB. Therefore, the solution potential at the working electrode located near the PGSB is not significantly different from that of the reference electrode (Figure 2-12). This is supported by the fact that the

potential fluctuation in OCP (ΔV_F) was less than 5 mV even under a high external electric field (ΔV_s) of 400 V/cm (Table 2-1). These results are in good accordance with the Klett report,⁸³ which showed the OCP data that was acquired on an equipotential surface. These results indicate that the working electrode located just in front of the PGSB has the same potential as the reference electrode when no potential bias is applied for amperometric detection. The potential fluctuation is minimized, and the noise level is effectively suppressed. Therefore, if the electrode is located just in front of the PGSB, there is no need for the enormous increase of detection potential to compensate for the effect of ΔV_s .^{66,81,84} Consequently, placing the working electrode close to the PGSB enables accurate control of the electrochemical potential in the middle of the electrophoretic channel, which allows for continuous amperometric detection during electrophoresis.

Table 2-1. Potential fluctuations at various distances between the PGSB and the working electrodes under a range of electrophoretic fields.

Electric field gradient (ΔV_s , V/cm)	Distance	0 μm	100 μm	200 μm	400 μm
	Potential fluctuation (ΔV_F , mV)				
30		± 1	± 30	± 6	± 10
60		± 2	± 20	± 4	± 10
110		± 2	± 30	± 60	± 20
170		± 1	± 20	± 20	± 8
220		± 5	± 50	± 30	± 300
280		± 4	± 20	± 40	± 60
400		± 3	± 10	± 30	± 300

2.3.4. Cyclic Voltammetry under Various Electric Fields

The electric potential gradient in the middle of the microchannel is proportional to the resistance of the region of interest on the microchip.⁸⁵ The local resistance in the region in front of the PGSB is significantly less than in other parts of the microchannel because the PGSB is an electric conductor that enables free migration of ions and is linked to the reference electrode. The potential drop near the PGSB is expected to deviate from the linearity of the electric potential in the remainder of the microchannel (Figure 2-12). This prediction was confirmed by the OCP data shown in Figure 2-10, which were acquired from the electrode placed in front of the PGSB and are almost free from the effects of the external potential gradient. Noise generated during the potentiometric measurement increased proportionally with the external electric field (ΔV_s). Nevertheless, the noise level was less than 5 pA in the Faraday cage. The cyclic voltammograms shown in Figure 2-13 indicate that the electrochemical redox behavior of the ferricyanide ions at the electrode remain unchanged except for a slight reduction in current and a potential shift of less than several tens of mV under an electric field up to 400 V/cm. This supports that the potential shift and noise resulting from the given range of ΔV_s ⁸⁶⁻⁸⁸ are acceptable for in-channel electrochemical detection during electrophoretic separation on a microchip.

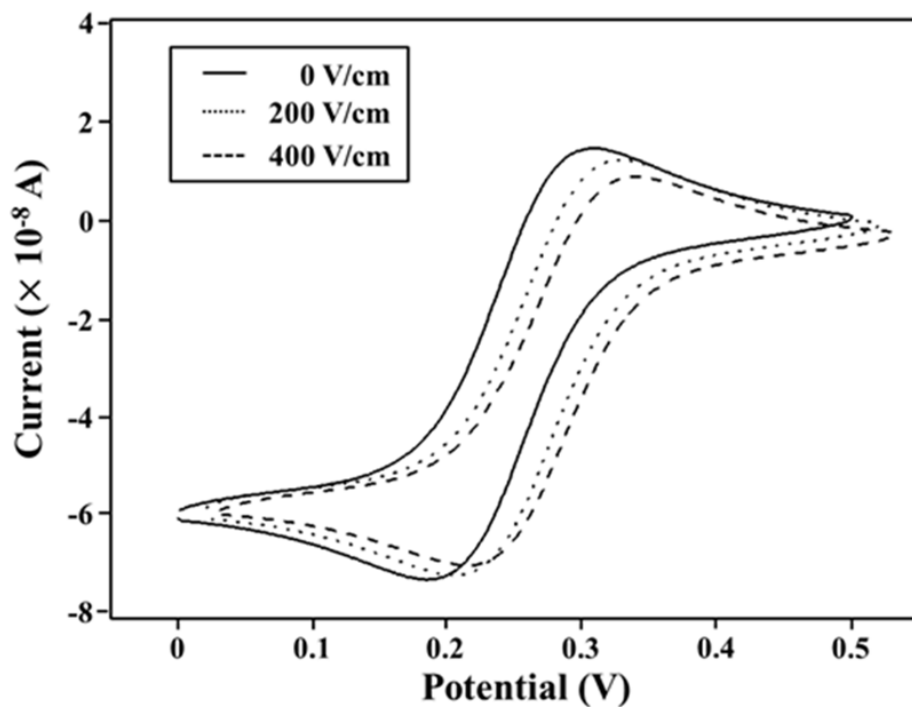


Figure 2-13. Cyclic voltammograms from the Au electrode located in front of the PGSB under CE fields: solid line (0 V/cm), dotted line (200 V/cm), and dashed line (400 V/cm). Cyclic voltammetry was performed in a 1 mM $\text{K}_3\text{Fe}(\text{CN})_6$ solution with 100 mM KNO_3 (supporting electrolyte). Conditions: width of the Au working electrode, 10 μm ; reference electrode, Ag/AgCl/KCl (3 M); counter electrode, Pt wire; scan rate, 100 mV/s.

As the distance between the working electrode and the PGSB increases, the EC measurements increasingly suffer from severe noise and inaccurate electrochemical potential of the electrode, which may eventually damage the working electrode (Figure 2-14). Therefore, the placement of the working electrode close to the PGSB overcomes the restrictions on amperometric detector position in terms of electrophoresis and allows versatile designs of the microfluidic chip.

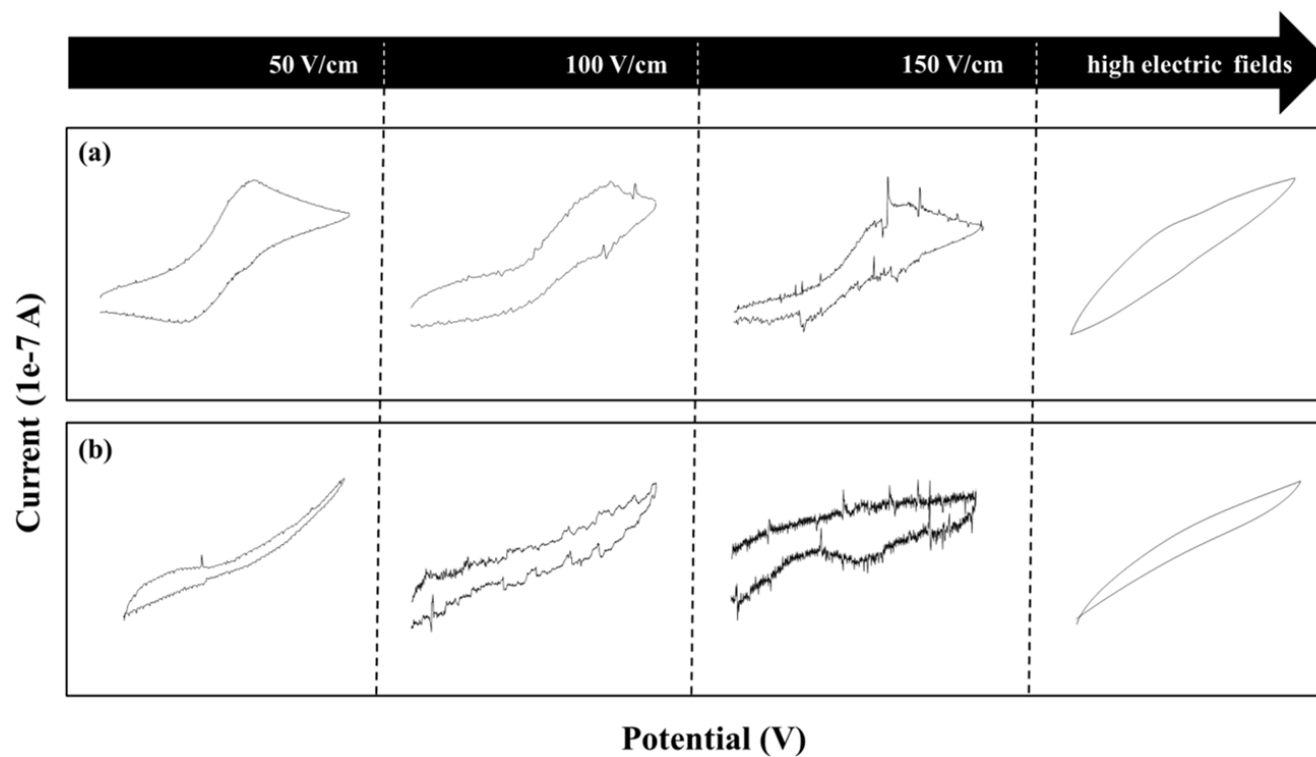


Figure 2-14. Effect of the distance from the PGSB to the Au working electrode under various electrophoretic fields. (a) Au working electrode 50 μm away from the PGSB. (b) Au working electrode 150 μm away from the PGSB. Au working electrode dimensions: 60 μm wide. Cyclic voltammetry conditions are the same as those for Figure 2-7.

2.3.5. Separation on a PGSB Integrated Microchip

Electrophoresis on a microchip equipped with the PGSB was performed to elucidate the separation and detection performances via the separation efficiency and amperometric response. Figure 2-15 shows the electropherograms from the Au microband electrodes located (a) 0 and (b) 50 μm from the PGSB. These electropherograms were obtained from the separation of 200 μM potassium ferricyanide at 150 V/cm on a PGSB-integrated microchip. The numbers of theoretical plates (i.e., separation efficiency) were 10 700/m (a) and 11 500/m (b), and the peak currents were 17 nA (a) and 8.0 nA (b). The roles of the polyelectrolytic gel were as an in-channel salt bridge electrically linked to the reference electrode and as a stopper to prevent leakage of the buffer solution (Figure F).

Although the polyelectrolytic gel is obviously a different material than glass, there are no significant differences between the two regions in terms of separation efficiency. For example, the number of theoretical plates measured using the electrode in front of the PGSB were similar to that from the other electrode, which was located 50 μm away from the PGSB. On the other hand, the peak current was twice as high for the electrode located in front of the PGSB than that of the electrode 50 μm from the PGSB. Figure 2-15 shows that the peak shape of the electropherogram from the electrode just in front of the PGSB was very similar to that from the electrode in the middle of the glass microchannel. The limit of detection ($S/N=2$) was determined to be 1.5 μM for ferricyanide under -150

V/cm.

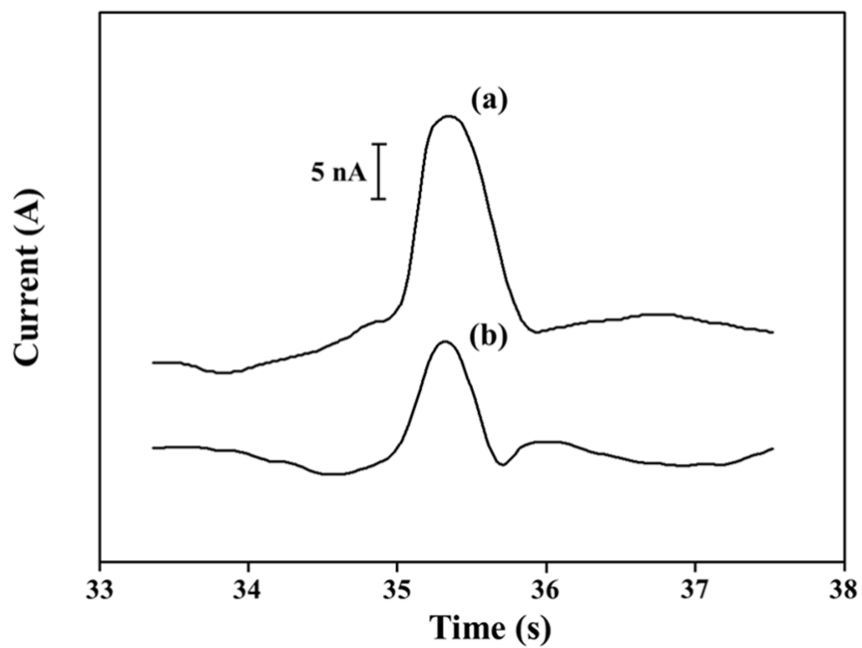


Figure 2-15. Electropherograms of 200 μM $\text{K}_3\text{Fe}(\text{CN})_6$ detected (a) 0 μm and (b) 50 μm from the PGSB. Conditions: CE field strength, -150 V/cm; Au working electrode width, 20 μm ; total length, 1.6 cm; effective length, 1.2 cm; running buffer, 25 mM sodium borate; detection potential, +0.15 V vs Ag/AgCl/KCl (3 M) reference electrode.

Figure 2-16 demonstrates the functionality of the proposed microchip system equipped with PGSB for neurotransmitter separation by electrophoresis. The electropherograms of the neurotransmitter mixtures consisting of dopamine (100 μ M) and catechol (150 μ M) show separation under electric fields ranging from 50 to 500 V/cm. The results shown in Figure 2-16 indicate that the electric field strength was the dominant parameter for determining the separation efficiency. The highest separation efficiency was observed under an electric field of 200 V/cm (catechol, 10 500/m, and dopamine, 8500/m). As the electric field increases from 50 V/cm to 500 V/cm, the migration time decreases for all compounds. The reproducibility of electrophoresis on the PGSB integrated microchip was evaluated by performing 7 repetitive separations. Mean migration times of 32 s (± 0.8) and 36 s (± 1.2) and peak currents of 750 pA (± 40) and 920 pA (± 35) were observed for dopamine and catechol, respectively. These electrophoresis results confirm reproducibly a separation under a high electric field employing a PGSB-based detection system.

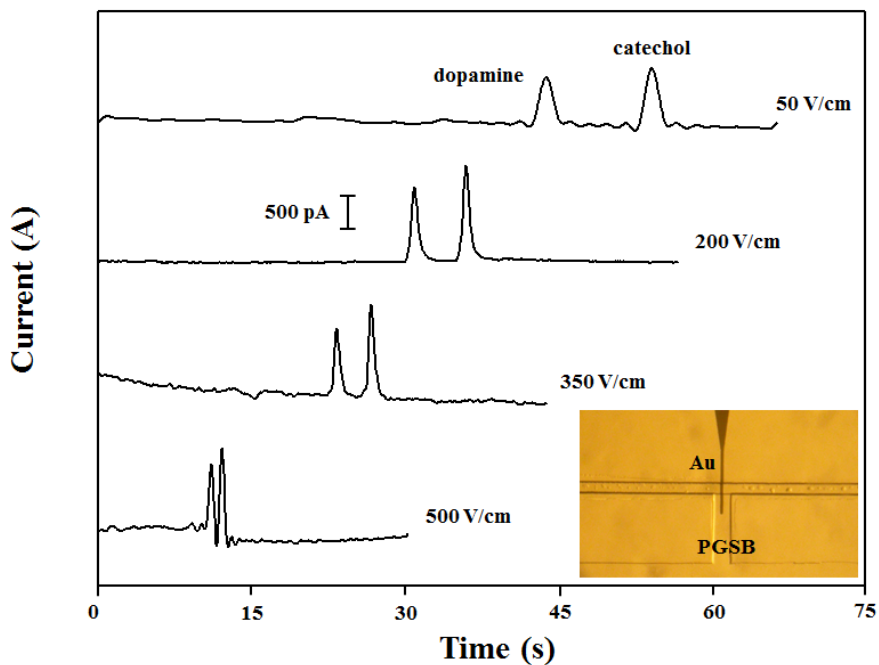


Figure 2-16. Electropherograms of dopamine (100 μM) and catechol (150 μM) under high electric fields obtained using the PGSB-integrated microchip. Conditions: width of the Au working electrode, 20 μm ; total length, 5.4 cm; effective length, 5 cm; running buffer, 25 mM MES; detection potential, +0.05 V vs Ag/AgCl/KCl (3 M) reference electrode.

2.4. Conclusions

A novel in-channel electrochemical detection method for MCE based on a polyelectrolytic gel salt bridge was proposed and validated. This configuration enables in-channel electrochemical detection with very limited interference of the applied electrophoretic field by the introduction of a PGSB. Besides enabling electrochemical detection under various high electric fields, the simple fabrication process of the concise glass microchip ensures promising applications for portable and reliable MCE devices. Consequently, this method represents a technical breakthrough as it provides a fundamental solution for electrochemical detection within a microchannel in the presence of a high electric field. By virtue of the proposed design, the electrochemical detector can function regardless of where it is placed within the microchannel network including in the middle of the separation channel under a high electric field. This indicates the possibility of chemical monitoring anywhere, even under a high electric field, using a chip-based micro total analysis system consisting of multiple functional units. Further integration and miniaturization of the control peripherals and the chip itself are predicted to enable the realization of practical systems for microfluidic analysis.

CHAPTER 3

NONFARADAIC NANOPOROUS ELECTROCHEMISTRY FOR CONDUCTOMETRY AT HIGH ELECTROLYTE CONCENTRATION

3.1. Introduction

Conductometry is widely regarded as a conventional method.³⁶ Conductivity measurements can be performed in two different modes: Contact and contactless.³⁷ Contactless conductivity measurements involve high excitation frequencies and capacitive coupling between the electrodes and the solution in order to determine the conductivity of the solution.⁸⁹ However, this method has limited sensitivity because the impedance of the dielectric layer is as high as that of the solution. In addition, high excitation frequencies are required to keep the impedance of the dielectric layer at a reasonable value, which leads to more expensive instrumentation. On the other hand, contact conductivity methods involve direct contact between the electrode and solution, resulting in a lower input ac frequency and higher sensitivity than contactless methods.

One of the general limitations in conductometry is the difficulty in detecting ions at high concentrations because the smaller resistance of the solution leads to a smaller contribution of solution resistance to the total impedance, which reduces the sensitivity of the ion analysis. This problem is aggravated at a small electrode because a higher electrode impedance leads to a smaller contribution of the solution resistance to the total impedance; this is why the maximum concentration of the dynamic range in conductometric detection does not exceed several tens of mM.³⁷

It is sometimes necessary to examine the variation in ion concentration and/or composition of the solution under a high ionic strength. Aqueous media with high

ion concentrations are ubiquitous in nature, e.g., sea water, cytosol, and body fluids contain many ions. Successful conductometry in the presence of a large amount of electrolytes would enable us to monitor extracellular signals such as the propagation of action potential along the axon in a neuron without a faradaic reaction. Measuring the concentration of salt brines is also useful for the fishing industry.⁹⁰ In addition, trace analysis of ions at high electrolyte concentrations is significant as demonstrated by the following examples: The detection of iodine, which is an essential micronutrient for many organisms, in seawater,⁹¹ bromate, which is classified as an animal and human carcinogen, in ozonated sea water for effective disinfectant in aquaculture,⁹² and Ca^{2+} as a regulator of neurotransmitter whose local concentration varies in extracellular fluid. For practical analysis, conductometry is the underlying principle for detection in ion chromatography. Because the concentration of an eluent is relatively high, an ion suppressor is required to magnify the conductance changes due to the analyte by reducing the background conductivity of the eluent. Despite advances in ion suppressor technology, issues of cost, maintenance, and miniaturization remain.^{93,94}

The impedance at the electrode-solution interface, which is referred to as electrode impedance in this dissertation, should be as low as possible for conductometry at high electrolyte concentrations. It is doubtful that enlargement of the real surface area of an electrode would reduce the electrode impedance; for example, platinization of an electrode surface was used to prepare Pt black, which has been used in commercial conductometry devices.⁹⁵ However, Pt black is

mechanically fragile and its nanoporous structure tends to collapse leaving debris. Recently, new fabrication methods that generate much more stable nanoporous materials with uniform and controllable pore sizes of a few nm have been reported.⁹⁶⁻⁹⁸ One of the nanoporous Pt electrodes prepared by these methods, i.e., L₂-ePt, has a higher surface-to-volume ratio than Pt black and has a lower impedance at the surface.⁹⁹ Without using any molecules with a specific ion affinity, alkali and alkaline earth ions can be differentiated via impedance measurements at L₂-ePt in aqueous solution at a high ionic strength.¹⁰⁰ This ion selectivity at L₂-ePt in the absence of any surface modifier is enabled not by the enlarged surface area but rather the morphology of the nanoporous electrodes. The ion transport and EDL overlap in the nanopores, which are the fundamental phenomena that underlie the apparent electrochemical behavior observed at nanoporous electrodes, sensitively depend on the electrolyte concentration of the solution¹⁰¹ and pore characteristics, i.e., size, connectivity, and uniformity.¹⁰² However, the knowledge to date is so limited that it rarely provides more than a superficial understanding. Therefore, in-depth impedometric investigation of nanoporous electrodes is crucial to deeper insights into nanoporous electrochemistry and further creative applications.

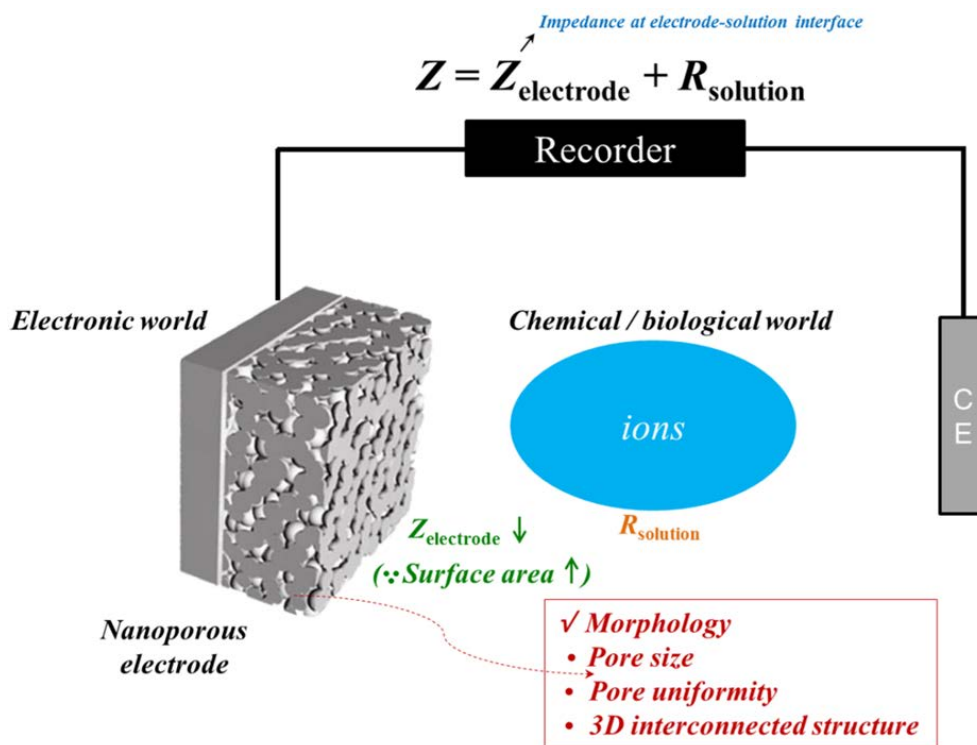


Figure 3-1. Effect of pore morphology on electrode impedance of the nanoporous electrode.

In this study, we employed three electrodes with different morphology (L₂-ePt, Pt black, flat Pt) for comparison study. L₂-ePt is a well-defined nanoporous electrode with pore sizes of 1–2 nm, whereas Pt black is a random-structured porous electrode with pore sizes in the nanometer range (Figure 3-2). It allows us to see how the nanoporous geometry contributes to the nonfaradaic impedance at nanoporous electrodes, suggesting a strategy for conductometry at high ionic strength.

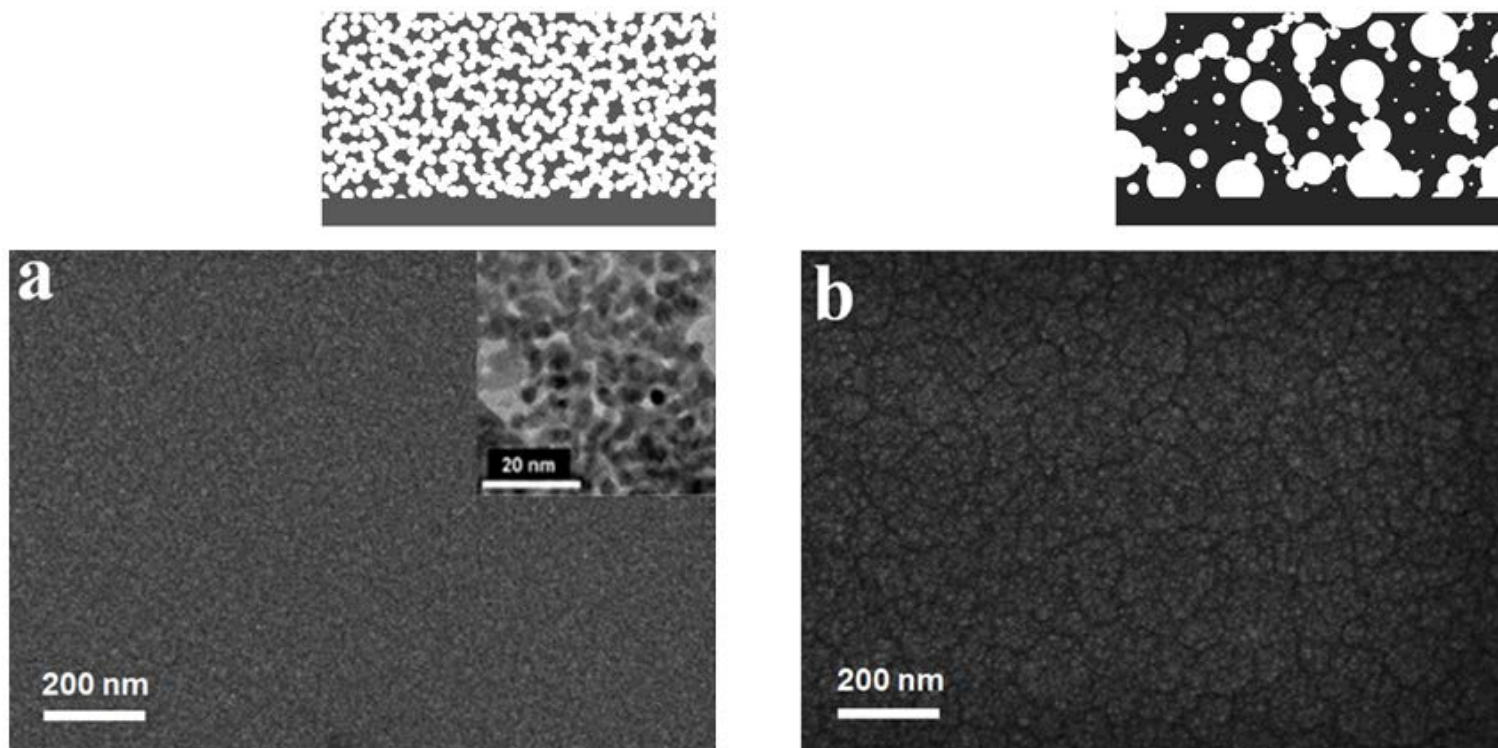


Figure 3-2. SEM image of nanoporous Pts: (a) L₂-ePt and (b) Pt black. Inset at (a) : TEM image of L₂-ePt.

3.2. Experimental

3.2.1. Reagents

t-octylphenoxypolyethoxyethanol (Triton ~~X-100~~)X sulfuric acid, sodium carbonate, sodium bicarbonate, sodium chloride, sodium fluoride, sodium bromide, sodium nitrate, and sodium sulfate were purchased from Sigma-Aldrich (St. Louis, MO) except for hydrogen hexachloroplatinate hydrate (Kojima chemicals, Japan) and were used without further purification. All the aqueous solutions in this experiment were prepared with ultrapure deionized water produced by NANOpure (Barnstead).

3.2.2. Fabrication of Nanoporous Pt

The nanoporous Pt denoted by L₂-ePt was prepared by electroplating of Pt in reverse micelle solution as described in our previous report.¹⁰³ Hydrogen hexachloroplatinate hydrate (5 wt%), 0.3 M sodium chloride (45 wt%), and Triton X-100 (50 wt%) were mixed and heated to 60 °C. The mixture as made was transparent and homogeneous. The temperature of the mixture solution was maintained around 40 °C using a thermostat (WCB-11H, Daihan Scientific). L₂-ePt was electrochemically deposited on micro electrode array (MEA60 200 Pt GND, Qwane Biosciences) at -0.2 V vs. Ag/AgCl. A micro-electrode array electrode with a diameter of 40 μm and a 5-μm-thick well was used as the substrate in order to maintain a constant geometric surface area before and after the fabrication of the

nanoporous electrode. The resulting L₂-ePt electrode was in distilled water for 1 day to extract the Triton X-100 and this procedure was repeated 3-4 times.

The Pt black electrode was fabricated by a reported method,¹⁰⁴ which is a lead-free method to neglect effects of electrode materials. The Pt black electrode was also fabricated by electrodeposition of platinum ions on the plane Pt electrode (MEA60 200 Pt GND, Qwane Biosciences) from a 50% hydrogen hexachloroplatinate hydrate aqueous solution. Pt black film was electrodeposited by applying constant potential at -0.12 V vs. Ag/AgCl. Scanning electron microscopy (SEM) characterization was performed using a SUPRA 55VP Field Emission SEM (Carl Zeiss) with an acceleration voltage of 2 kV.

3.2.3. Electrochemical Measurements

Cyclic voltammetry was performed in a three electrode system, using Model CHI750 (CH Instruments) as electrochemical analyzer. Hg/Hg₂SO₄ (saturated K₂SO₄, RE-2C, BAS Inc.) and Pt wire (dia. 0.5 mm, Sigma) were used as reference electrode and counter electrode, respectively. The plane Pt electrodes were used as a flat working electrode to compare with nanoporous Pt. Reference 600 equipped with EIS300 electrochemical impedance spectroscopy software (Gamry Instruments) was used for the electrochemical impedance spectroscopy (EIS) experiments. A programmed ac input with 10 mV amplitude over a frequency range from 0.1 Hz to 10 kHz was superimposed on the dc potential, -0.5 V vs. Hg/Hg₂SO₄ where no faradaic reaction occurs.¹⁰¹ All experiments were carried out

at room temperature. The solution was purged with high purity nitrogen gas for 15 min prior to use and nitrogen environment was maintained over the solution throughout the experiments.

3.2.4. Fabrication of a Nanoporous Pt Integrated PDMS/Glass Chip

The fabrication of the PDMS/glass chip was prepared similarly to our previous work.^{105,106} Briefly, after cleaning a glass slide (Cat. No. 1000412, Paul Marienfeld GmbH & Co. KG, Germany) using a piranha solution ($\text{H}_2\text{SO}_4/\text{H}_2\text{O}_2 = 3:1$), the glass substrate was processed in sequence by spin coating photoresist AZ 5214 (Clariant, Switzerland) at 4000 rpm, prebaking for 1 min at 100 °C, first exposure for 5 s at 17 mJ/cm², reversal baking for 5 min at 100 °C, flood exposure for 20 s at 17 mJ/cm², and development using AZ300MIF (Clariant, Switzerland). The Pt electrodes made of 2000 Å Pt film/200 Å Titanium (Ti) layer were sputtered and then patterned using the lift-off process to remove the reminder of the patterned Pt/Ti film. The final nanoporous electrodes patterned substrate was prepared by electroplating. The electroplating method of nanoporous Pt is shown in the Fabrication of Nanoporous Pt Section.

The master for the PDMS microchannel was prepared using similar photolithographic procedures. In brief, photoresist SU-8 2050 (MicroChem Corp., USA) was spin-coated at 1800 rpm onto a silicon wafer and then sequentially treated with photolithography procedures including soft baking, UV exposure, post expose baking, development, hard baking. PDMS monomer and its curing agent

(Sylgard 184, Dow Corning, USA) were mixed at 10:1 and poured into the SU-8 master and degassed in a vacuum chamber. After curing in the oven for 90 min at 65 °C, PDMS was detached from the master and punched for creating 1 mm diameter reservoirs of the microchannel. The electrodes patterned glass slide was bonded to the PDMS substrate by plasma treatment (Figure B).

3.2.5. Ion Chromatography and Conductivity Detection

The ion chromatographic system consisted of an IP20 isocratic pump (Dionex, Sunnyvale, CA, USA), a Rheodyne 7725i sample injector (Rheodyne, Cotati, CA, USA) with a 5 or 25 μ L PEEK loop, a CD20 conductivity detector (Dionex, Sunnyvale, CA, USA), a 4 mm SRS 300 suppressor (Dionex, Sunnyvale, CA, USA), and a microchip-based conductivity detection system. A Dionex IonPac AS14 column (250 \times 4 mm i.d.) was used at room temperature. The end of PEEK tubing from the column or suppressor was inserted into the inlet reservoir in the PDMS/glass chip (Figure 3-3).

Conductivity detections were performed using an SR830 DSP lock-in amplifier (Stanford Research Systems, Sunnyvale, CA, USA). An ac input of 10 mV amplitude with frequencies among 1 kHz, 100 Hz, and 10 Hz from the lock-in amplifier was applied to a pair of identical electrodes in the PDMS/glass chip. Series resistances were used as the voltage divider. The output DC voltage of the lock-in amplifier was transmitted to the computer through a data acquisition card (National Instruments, Austin, TX) at a rate of 1 kHz. Collected signals were saved

using the LabView software (National Instruments, Austin, TX) for data analysis.

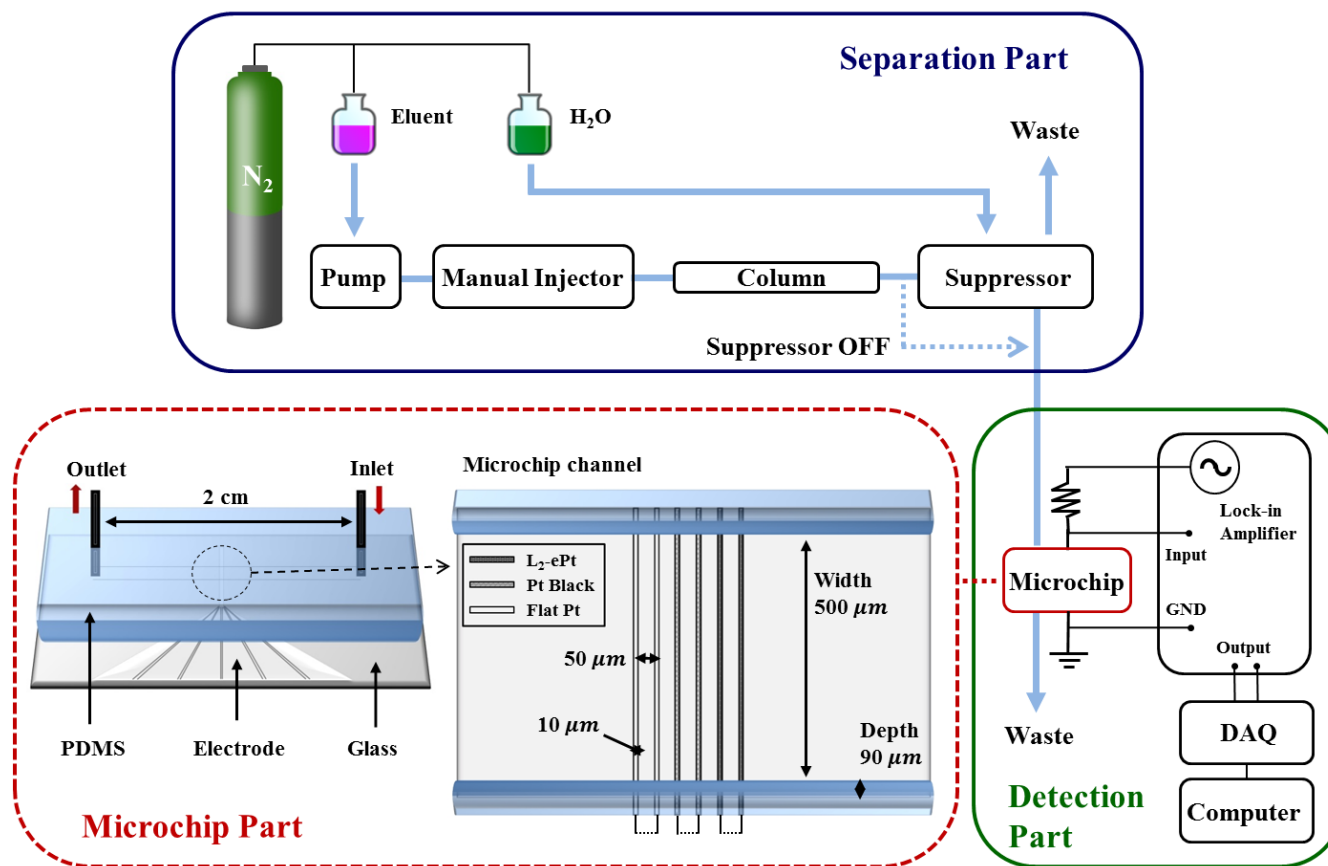


Figure 3-3. Schematic diagram of the setup used for ion chromatography with microchip-based conductivity detector.

3.3. Results and Discussion

3.3.1. Determination of Real Surface Area Using Cyclic Voltammetry

The SEM images of the nanoporous Pt electrodes used in this study (Figure 3-2) show that Pt black occurs as a rough and random film, whereas the surface of L₂-ePt looks smooth at the same scale, indicating uniformly distributed minuscule pores with 1–2 nm diameters, as confirmed by the TEM image of L₂-ePt. The structure of L₂-ePt appears to be a sponge with numerous three-dimensionally interconnected pores.¹⁰³ The electrochemical cleaning of the electrodes was conducted by cycling potential in a 1 M H₂SO₄ solution. The nanostructured electrodes were cycled over the limited potential range of 0.2 V versus Hg/Hg₂SO₄ to minimize the degradation of the nanostructure that may occur during surface oxide formation. Figure 3-4 shows a comparison of the cyclic voltammetric responses of the fabricated Pt electrodes in a 1 M H₂SO₄ solution. The much larger current at the L₂-ePt and Pt black electrodes is characteristic of the enlarged surface area resulting from the electrodeposited Pt. The roughness factor (f_R = real surface area/ apparent surface area) at the L₂-ePt (f_R 212) and Pt black (f_R 232) electrodes was determined from the hydrogen adsorption/desorption peaks of the cyclic voltammograms referring to 210 $\mu\text{C cm}^{-2}$ of the conversion factor.¹⁰⁷ It reflects the similarity in the real surface areas of the two electrodes or the slightly larger real surface area of Pt black than that of L₂-ePt.

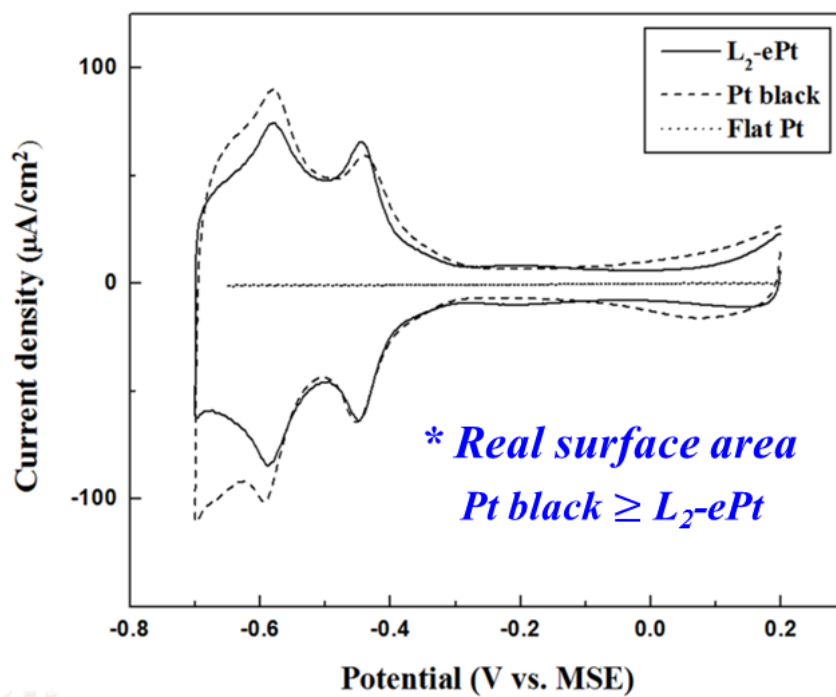


Figure 3-4. Comparison of cyclic voltammograms of the electrodeposited Pt electrodes (L₂-ePt and Pt black) and the flat Pt electrode in 1 M H₂SO₄ at 200 mV/s. MSE denotes mercury sulfate electrode (Hg/Hg₂SO₄). Apparent surface area of working electrode is 0.00001256 cm².

3.3.2. Impedance in Various Electrolyte Concentrations

Figure 3-5 shows the impedometric results for 0.001–1 M NaF solutions. A frequency of 1 kHz, which is typically employed for conductometry measurements, was applied for this experiment. As clearly evident in Figure 3-5a, the nanoporous Pt electrodes, i.e., L₂-ePt and Pt black, were more sensitive to the ion concentration than the flat Pt electrode. Interestingly, the difference in impedance among the Pt electrodes became larger at higher ion concentrations. Compared with Pt black, L₂-ePt clearly exhibited a lower impedance at 0.1 M, and this behavior was more obvious at 1 M despite the similar surface areas of the two electrodes.

To clarify this behavior, the electrode impedance was calculated by subtracting the solution resistance, obtained by fitting from the measured impedance, from the total impedance. While the electrode impedance of flat Pt was almost independent of the ion concentration, as shown in Figure 3-5b, the electrode impedance of the nanoporous Pt electrodes decreased as the ion concentration increased. Moreover, the electrode impedance of L₂-ePt dropped much more than that of Pt black. Figure 3-5b shows that the response of the total impedance to ion concentration is attributed to the electrode impedance.

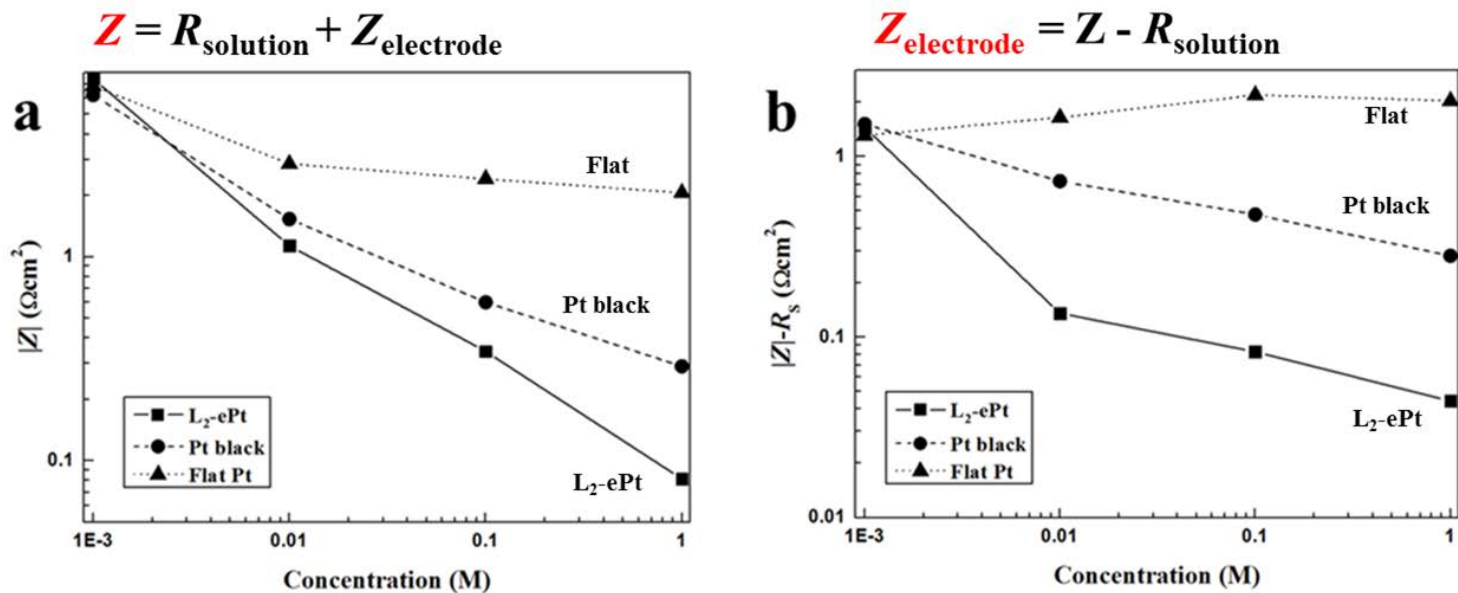


Figure 3-5. (a) Total impedance as a function of concentration for comparison between the nanoporous and flat electrode. (b) Impedance corrected by subtracting solution resistance (R_s) from (a).

3.3.3. Capacitance of Nanoporous and Flat Pts

Under the conditions for Figure 3-5, i.e., no faradaic reaction and the presence of only nonadsorptive electrolytes, the electrode impedance is described by its capacitance. Figure 3-6 shows that the dependence of the capacitance on the ion concentration at the flat Pt electrode differs from that at the nanoporous Pt electrodes. The electrode capacitance, C_e , can be determined using the following equation:

$$C_e = (2\pi fZ'')^{-1} \quad (1)$$

The capacitance of the flat Pt was almost invariant with ion concentration, whereas that of the nanoporous Pt electrodes sensitively responded to the change in ion concentration. Considering the pore size and the Debye length estimated from the electrolyte concentration (the calculated Debye length is 9.6 nm for 1 mM electrolyte), the EDL overlap was predicted to occur inside the nanoporous electrodes, resulting in a reduced double layer capacitance. Because the EDL thickness depends on the ionic strength, the capacitance at the nanoporous electrode can be tuned by controlling the ionic strength.¹⁰¹ Typically, 0.4 M electrolyte per volt is required to charge nanoporous electrodes with a specific capacitance of 10 $\mu\text{F}/\text{cm}^2$ and diameter of 10 nm.¹⁰⁸ If the concentration of the electrolyte is not sufficiently high, ions from the bulk solution should be transported toward the nanopores. Therefore, the capacitance of the nanoporous electrode can also be influenced by the mass transfer rate of electrolytes. In Figure 3-6, the dependence of the capacitance on ion concentration is manifested in the

high-frequency region, while the slope at low frequencies is gentle. The region where the capacitance responds sensitively to frequency shifts to higher frequency for higher ion concentration. In the high-frequency regime, the mass transport of ions from the bulk solution is negligible and the EDLs inside the nanopores remain overlapped during the impedance measurements. In this situation, the capacitance should be a sensitive function of frequency. A thinner EDL at higher ion concentrations requires ion displacements over a shorter distance for charging so that the capacitance varies on a shorter time of electric field oscillation, i.e., higher frequency. The higher capacitance of L₂-ePt indicates that the charging dynamics at the L₂-ePt are faster than at Pt black. In contrast to the nanoporous electrodes, flat Pt exhibited a monotonous response of the electrode capacitance to the frequency variation, and the ion concentration had only a minor influence.

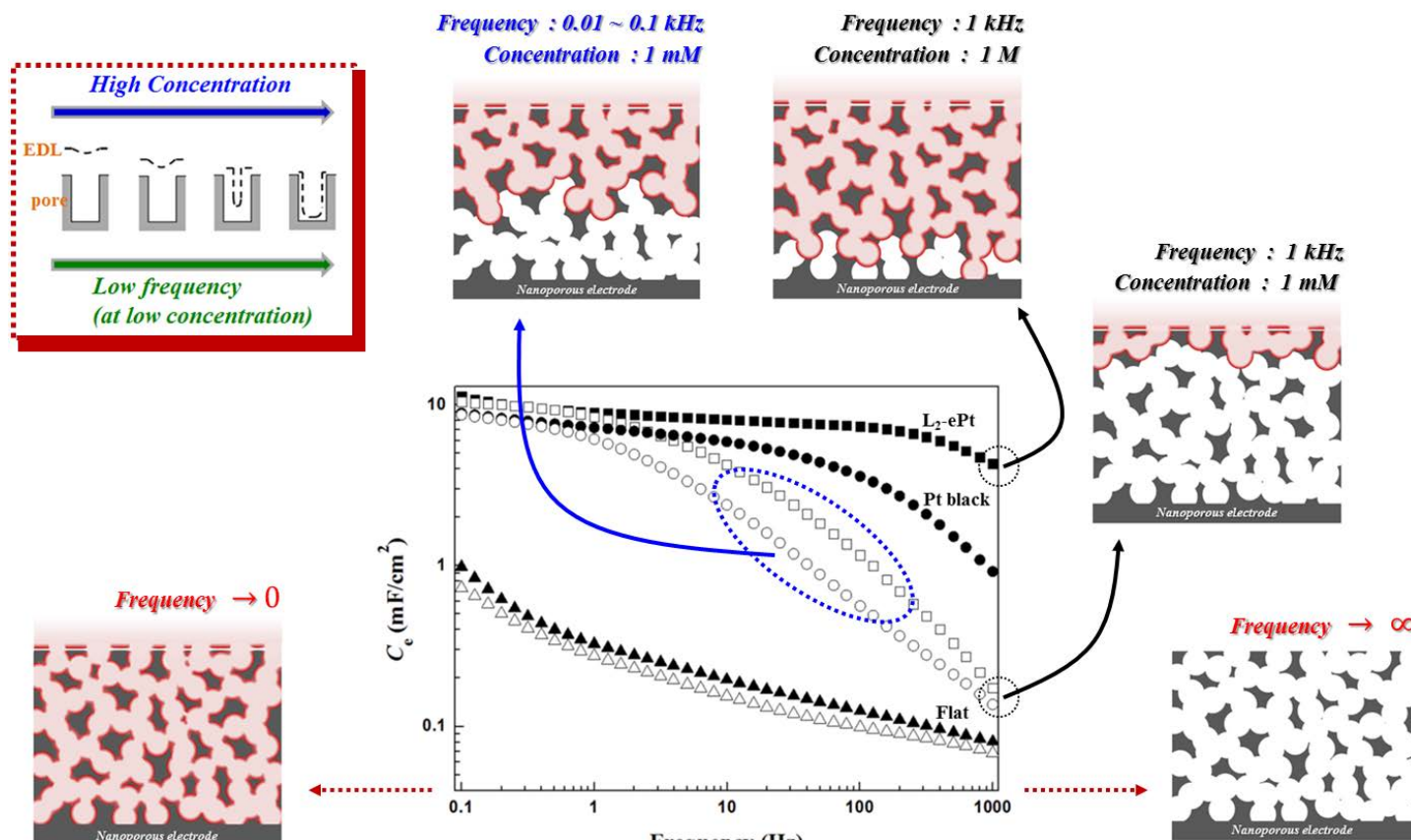


Figure 3-6. Electrode capacitance (C_e) of L₂-ePt (■), Pt black (●), and flat Pt (▲) as a function of frequency. 1 mM (open) and 1 M (filled) NaF solutions.

3.3.4. Determination of the Pore Resistance Using TLM

More sophisticated models are required for a deeper understanding of the structural complexity of nanoporous electrodes. The Transmission line model (TLM) proposed by de Levie¹⁰⁹ is widely used for the analysis of electrochemical results from nanoporous electrodes.^{110,111}

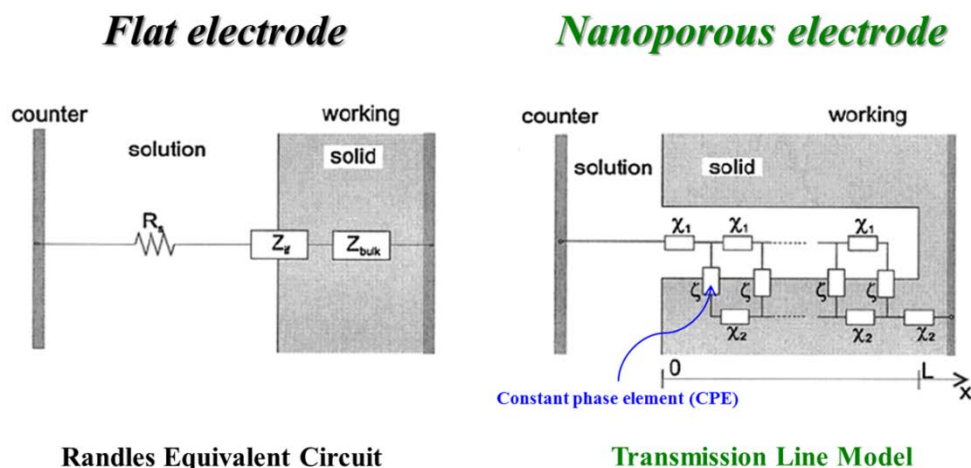


Figure 3-7. Transmission line model for the analysis of electrochemical results from nanoporous materials.

One of the purposes of TLM is to evaluate the relaxation frequency and pore resistance, which are closely related to the morphological aspects of the nanopores. The relaxation frequency, F_L , indicates the knee frequency in the Nyquist plot at the nanoporous electrode.¹¹² In contrast to the impedance of flat electrodes, a line with a 45 slope commonly appears in the high-frequency region of the Nyquist

plots of nanoporous electrodes. The plot evolves into a vertical line that represents a combination between resistance and capacitance in series in the frequency region lower than the knee frequency. The F_L provides information regarding the charging dynamics at nanoporous electrodes: the line with the unity slope at high frequencies comes from the limitation of the mass transport of ions into the nanopore. As the interfacial polarization process is not purely capacitive but exhibits a complex behavior in this system, the capacitive element should be described by a constant phase element (CPE).¹¹³ In this case, TLM is illustrated in Figure 3-10d. F_L can be determined using eq 2.¹¹²

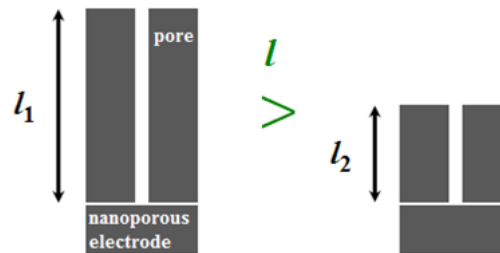
$$F_L = \frac{1}{2\pi(rql^2)^{1/\alpha}} \quad (2)$$

In eq 2, r is the electrolyte resistance per unit of length in the pores, l is the film thickness, q is the constant that contains the double-layer capacitance, and α is a function of the phase angle ϕ with the relation of $\alpha = \phi/(\pi/2)$.

*** Relaxation Frequency (F_L)**

$$F_L = \frac{1}{2\pi R_1 C_3} = \frac{1}{l^2 r_1 q_3}$$

Electrode thickness (l)



1. l : thickness

2. r : electrolyte resistance (per unit of length in the pores)

3. q : capacitance

Electrolyte resistance (r)

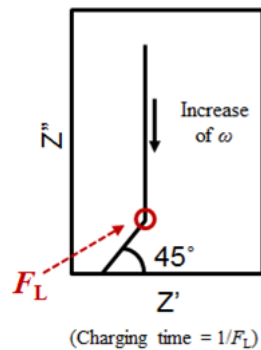
Pore size



Connectivity

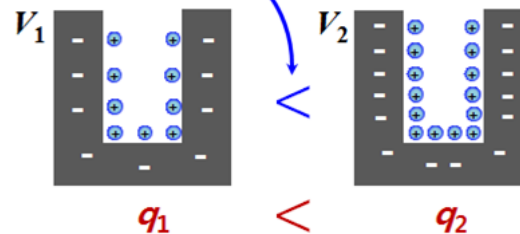


- Nyquist plot



Capacitance (q)

the total number of ion for charging



Assumption
applied voltage
 $V_1 = V_2$

Figure 3-8. Conceptual diagram of relaxation frequency.

The r , q , and α values were obtained by fitting the experimental data as shown in Figure 3-10. Table 3-1 shows that the F_L values of the nanoporous electrodes increase as the electrolyte concentration rises. High electrolyte concentrations bring about quick capacitive charging inside the pores without any considerable involvement of the mass transport of ions into the pores. The F_L of L₂-ePt is roughly 10 times higher than that of Pt black. Because the reciprocal of F_L indicates the access time, L₂-ePt has a short access time for capacitance owing to its fast charging dynamics (Figure 3-9).

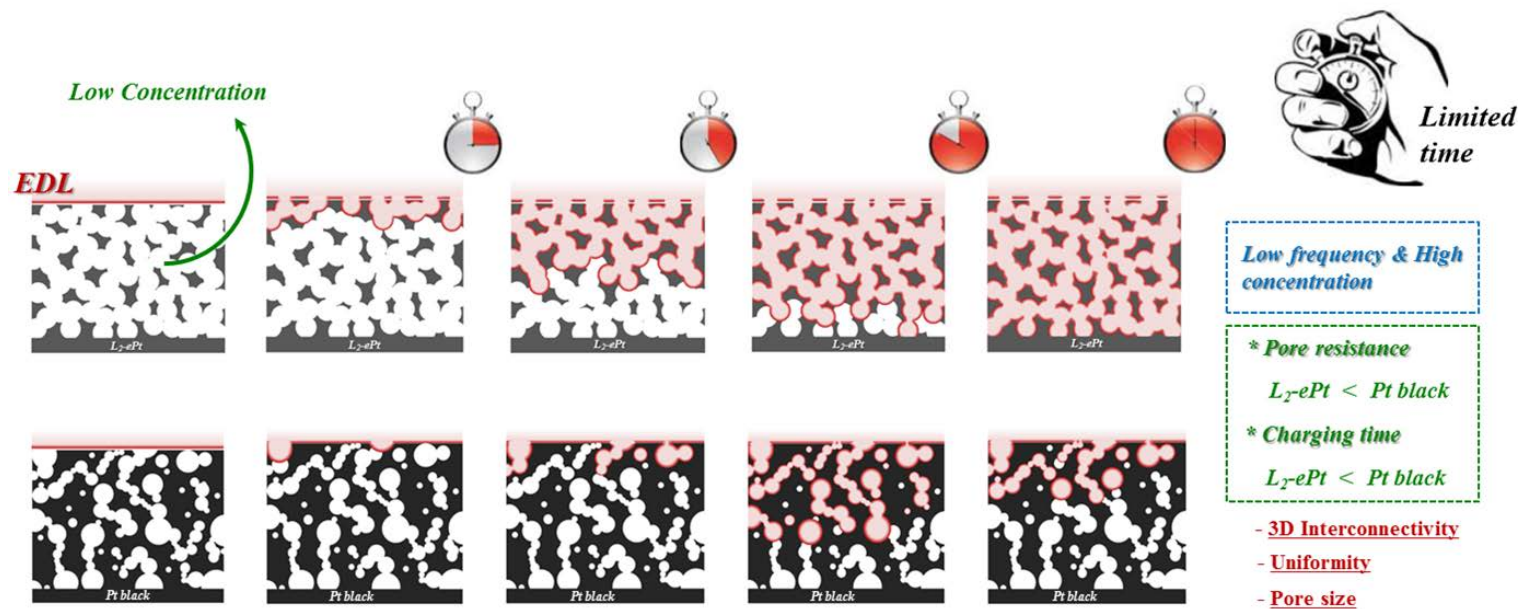


Figure 3-9. Predicted charging time of the nanoporous Pt electrodes (L_2 -ePt and Pt black).

Figure 3-10 shows the Bode plots for L₂-ePt, Pt black, and flat Pt; L₂-ePt and Pt black showed similar trends, including a plateau in the intermediate frequency region and two parallel lines between $\log(Z'-R_s)$ and $\log Z''$ with a slope of $-\alpha$ in the low-frequency region. It should be noted that the plateau in the Bode plot does not originate from R_s but from the resistance elements inside the pores. The short plateaus in Figure 3-10, parts a and b are characteristic of nanoporous electrodes.¹¹⁰ In contrast, no plateau appears in the Bode plot for flat Pt. This critical difference is ascribed to the pore resistance, which comes from the pore walls interfering with ion migration in the nanoporous electrode.^{109,112}

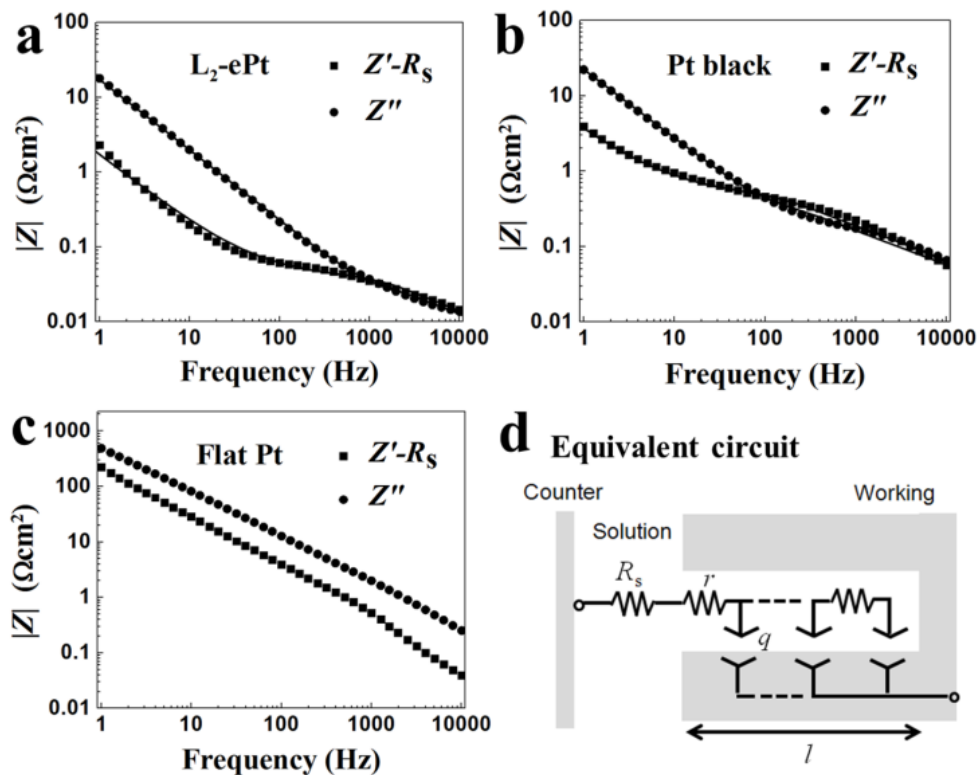


Figure 3-10. Bode plots from (a) $\text{L}_2\text{-ePt}$, (b) Pt black, and (c) flat Pt in 1 M NaF.

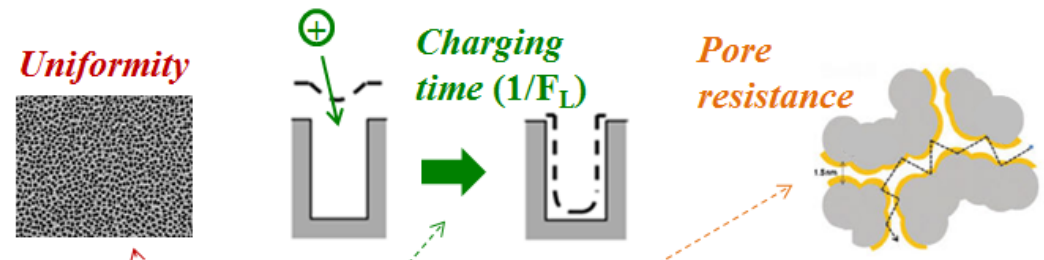
The Z' values in the Bode plots were corrected with the solution resistances. The data in (a,b,c) were fitted based on equivalent circuit with CPE based on TLM (solid line) presented in (d).

The pore resistance can be also determined by fitting the experimental data using the TLM; the fitting parameters can then be substituted into eq 3 to determine the value of the pore resistance (R_{pore}).

$$R_{\text{pore}} = \frac{lr}{3} \quad (3)$$

Table 3-1 shows that the R_{pore} values of the nanoporous electrodes decrease with increasing electrolyte concentration and that the R_{pore} of L₂-ePt is much smaller than that of Pt black. The ratio of the difference between the two R_{pore} values to the average value, i.e., $\delta R_{\text{pore}} / [R_{\text{pore}}] \equiv \gamma_{\text{pore}}$, of L₂-ePt is superior to that of Pt black.

Table 3-1. Impedometric parameters measured from L₂-ePt and Pt black.



concn [C] (M)	L ₂ -ePt			Pt black			range [C] (M)	γ_{pore}^d	
	α^a	F_L (Hz) ^b	R_{pore} ($\Omega \text{ cm}^2$) ^c	α	F_L (Hz)	R_{pore} ($\Omega \text{ cm}^2$)		L ₂ -ePt	Pt black
0.001	0.86	1.15	5.47	0.82	0.49	11.58	0.001–0.01	1.76	1.27
0.01	0.92	19.34	0.35	0.85	2.39	3.05	0.01–0.1	0.91	0.62
0.1	0.94	52.81	0.13	0.90	4.68	1.61	0.1–1	1.08	1.07
1	0.94	180.12	0.04	0.90	16.82	0.49	0.001–1	1.97	1.84

^aCPE exponent. ^bRelaxation frequency. ^cPore resistance. ^dRatio of the difference between the two pore resistance values to the average value.

3.3.5. Mechanism for Conductometry at Nanoporous Electrode

The origins of the sensitive response of the nanoporous electrodes are summarized in Figure 3-11.

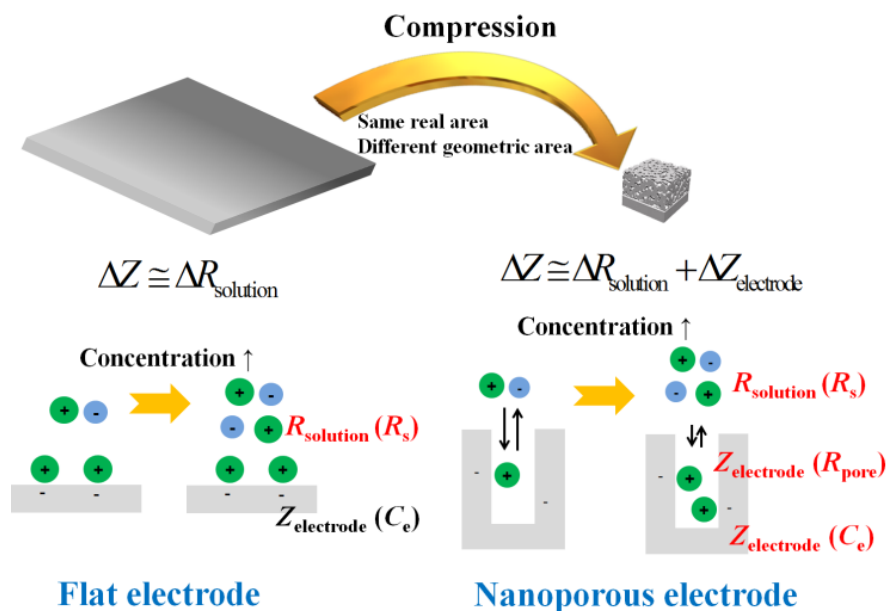


Figure 3-11. Mechanism for conductometry at nanoporous electrode. The impedance components in red indicate the elements to which the observed conductance is attributed.

First, the enlarged surface area reduces the electrode impedance. As the electrode gets smaller, the surface-to-volume ratio serves as a more important factor to effectively diminish the impedance. It is obvious that nanoporous electrodes with smaller nanopores are more appropriate, especially for ultramicroelectrodes that are a few micro- or submicrometers in diameter. Second, the electrode impedance

varies as a function of ion concentration. The capacitance and pore resistance of L₂-ePt respond more sensitively to changes in the ion concentration than those of Pt black. At high ion concentrations, the charging process at the L₂-ePt is faster than at the Pt black electrode, as indicated by a higher capacitance and lower pore resistance. This leads to a significantly lower electrode impedance of L₂-ePt than that of Pt black, due to its distinct morphology. L₂-ePt has a uniform 3D interconnected nanoporous structure with pore sizes of 1–2 nm, whereas Pt black has randomly distributed pores including very small ones of less than 1 nm. The better pore connectivity and more uniform structure of L₂-ePt are the causes of its fast charging dynamics (Figure 3-12). These results are in good accordance with previous results that showed that ordered mesoporous solids exhibit faster diffusion processes (by about 1 order of magnitude) in comparison with nonordered gels of similar or even larger porosity.^{114,115}

*** Shortest route**
 $L_2\text{-ePt} < \text{Pt black}$

*** Charging time**
 $L_2\text{-ePt} < \text{Pt black}$

*** R_{pore}**
 $L_2\text{-ePt} < \text{Pt black}$

Assumption

1. $l_1 = l_2$
2. Pore size ($L_2\text{-ePt} = \text{Pt black}$)

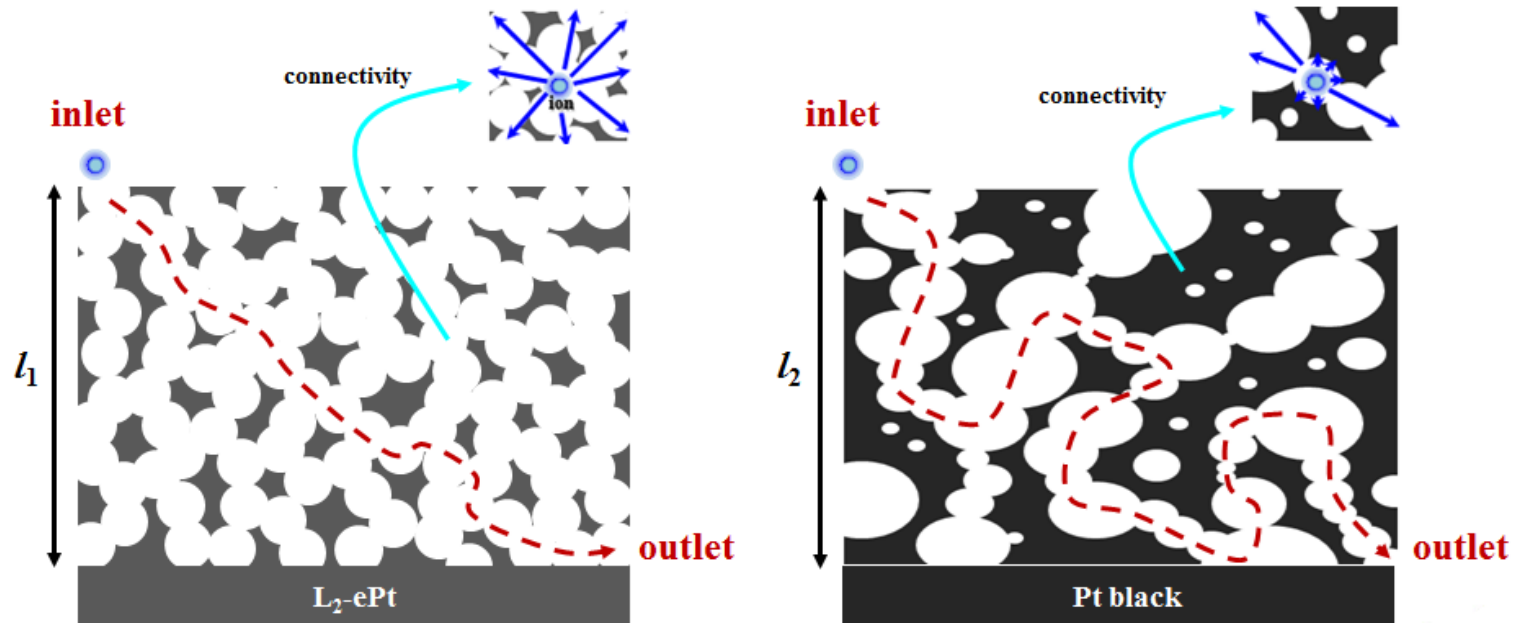


Figure 3-12. Effect of pore connectivity in the nanoporous Pt electrodes ($L_2\text{-ePt}$ and Pt black).

When it comes to pore size, smaller pores will retard more severely ion transport through the pores (Figure 3-13). One can see the distribution of pore sizes, particularly the presence of very small pores, from the slopes of the Nyquist plot in the region below the relaxation frequency, F_L .^{116,117} The slope carries information about the α value of CPE. Table 3-1 shows that the α values of L₂-ePt are higher than those of Pt black. This means that the characteristic charging behavior of L₂-ePt is closer to pure capacitance, indicating a more facile ion transport through the nanopores.

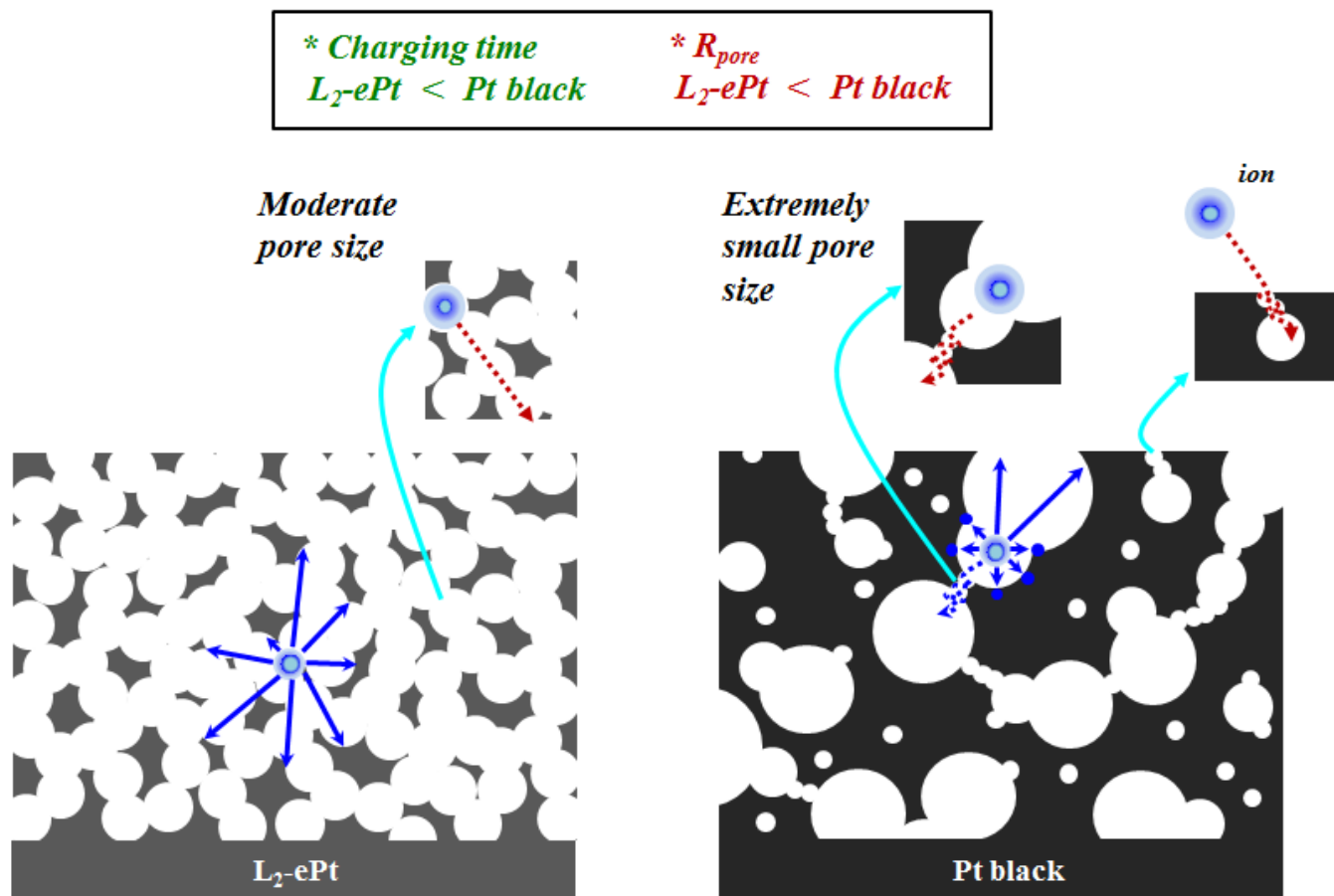


Figure 3-13. Effect of pore size in the nanoporous Pt electrodes ($L_2\text{-ePt}$ and Pt black).

3.3.6. Nonfaradaic Electrochemical Behavior at Nanoporous Electrode

The results of the impedance analysis described above tell us that nanoporous electrodes with diameters comparable to the thickness of the EDL have an electrode impedance that varies with the real surface area and/or the characteristic elements produced by nanopores such as the pore resistance, R_{pore} , and the factor containing the capacitance, C_e . These factors that can modify the electrode impedance are discriminatively determined by the input ac frequency and the electrolyte concentration. In the case of a high frequency and a low ion concentration, the EDLs overlap in nanopores (see case 1, Figure 3-14) so that surface enlargement makes little contribution in reducing the electrode impedance, while R_{pore} and C_e are still influential. In all remaining cases, which are a low frequency and a low ion concentration or a high ion concentration regardless of the frequency, the area of the EDL surface is enlarged to be commensurate with the porous geometry of the electrode body and thus substantially contributes to the decrease in the electrode impedance. The nanopore-characteristic factors, R_{pore} and C_e , influence the electrode impedance as well, making conductometric signals more sensitive (see case 2, Figure 3-14). Therefore, nanoporous electrodes for conductometry are less advantageous under low ionic strengths and high frequency conditions.

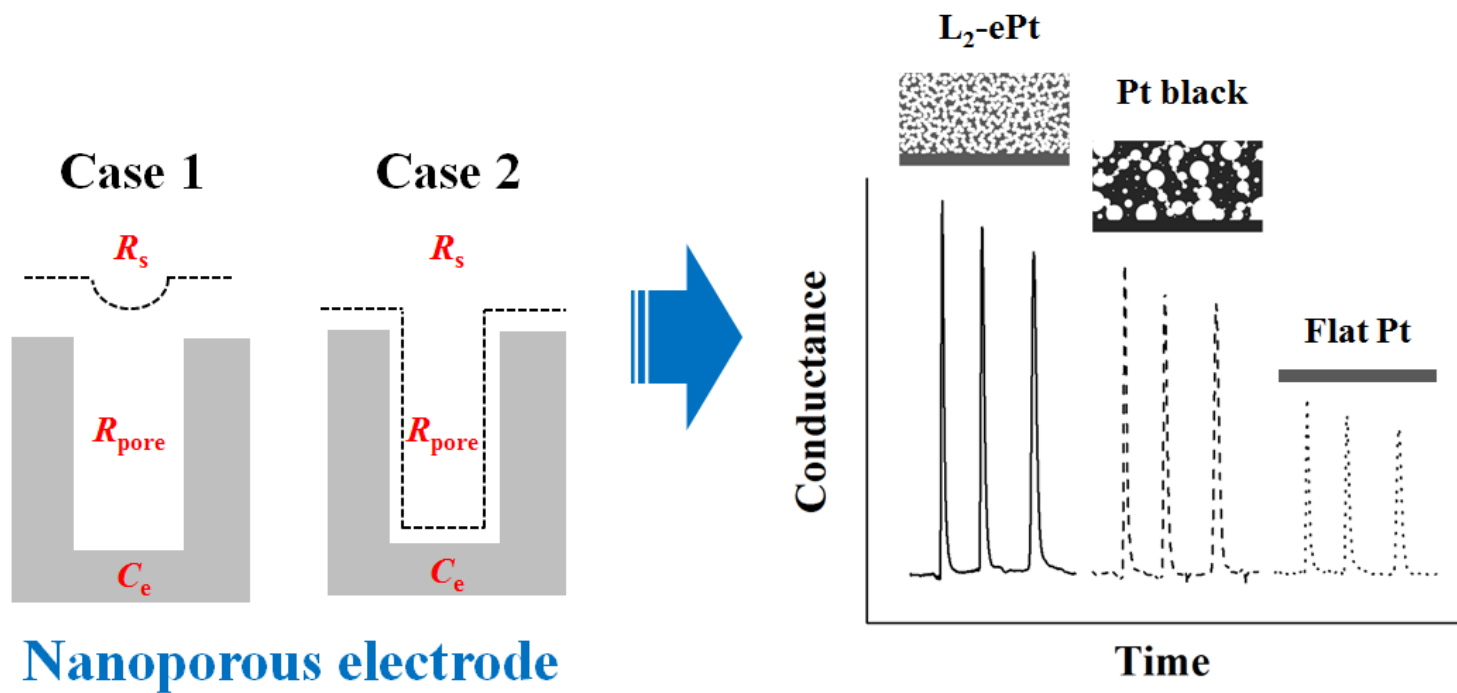


Figure 3-14. Two cases for nanoporous electrodes in the solution. Dashed line indicates electrical double layer.

3.3.7. Conductance Detection Using Nanoporous Electrode

On the basis of the results of the impedometric study, the nonfaradaic electrochemical behavior at nanoporous electrodes suggests useful applications. In this study, we exploited nanoporous Pt for conductometric detectors that can be integrated with conventional ion chromatographs.

Because the conductivity change is hardly detected at high ionic strengths, ion chromatography is normally conducted with an ion suppressor to lower the electrolyte concentration to the submillimolar level. If nanoporous electrodes can sufficiently suppress the electrode impedance, the conductometric signal will be enhanced and successfully detected at high ionic strengths, even without using an ion suppressor. Figure 3-15 shows the influence of the nanoporous electrode morphology on the conductometric signal intensity. It is obvious that L₂-ePt gives the strongest signal throughout the full range of applied frequencies, though the real surface areas of the L₂-ePt and Pt black electrodes are similar. In principle, the change in conductivity should be smaller at lower operating frequencies due to higher electrode impedance, as confirmed by the results of the flat Pt electrode in Figure 3-15. However, it is interesting that the signal intensity of nanoporous Pt electrodes at 10 Hz is rather higher than 1 kHz, such that the difference from the flat electrode is increased.

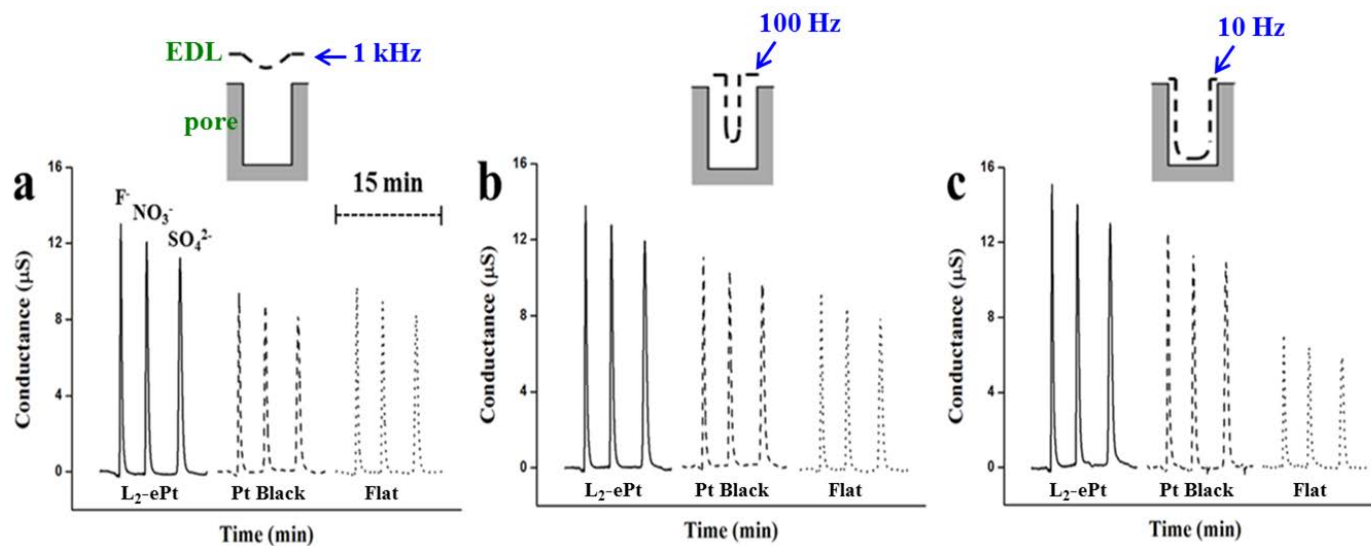


Figure 3-15. Ion chromatograms obtained using the L₂-ePt, Pt black and Flat Pt electrodes as a function of frequency (a) 1 kHz, (b) 100 Hz, and (c) 10 Hz under suppressed detection mode: solid line (L₂-ePt), dashed line (Pt black), and dotted line (Flat Pt). Conditions: eluent, 3.5 mM sodium carbonate/1 mM sodium bicarbonate; flow rate, 1.2 mL/min; injection, 25 μL of 1.5 mM F^- , 1 mM NO_3^- , and 0.6 mM SO_4^{2-} .

The ion concentration and dynamic distribution in the nanopores have a great influence on the electrode impedance. Because the polarization in the pores is remarkably affected by ion transport from the bulk solution, the electrode impedance of nanoporous electrodes should be sensitive to a change in ion concentration of the bulk solution, particularly near the pore inlets. The chromatograms in Figure 3-15 were obtained when the ion suppressor was turned on. As a result, the electrode impedance was not sufficiently reduced due to a low ion concentration at the high frequency. On the other hand, when the frequency was lowered, the nanoporous system had enough time for ions to transport from the bulk solution into the pore so that the electrode impedance was significantly reduced by the augmented ion concentration inside the nanopores (Figure 3-16, 3-17).

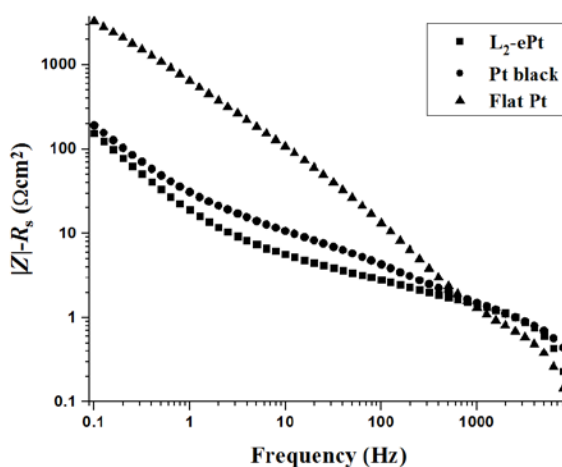


Figure 3-16. Electrode impedance as a function of frequency in 1 mM NaF solution.

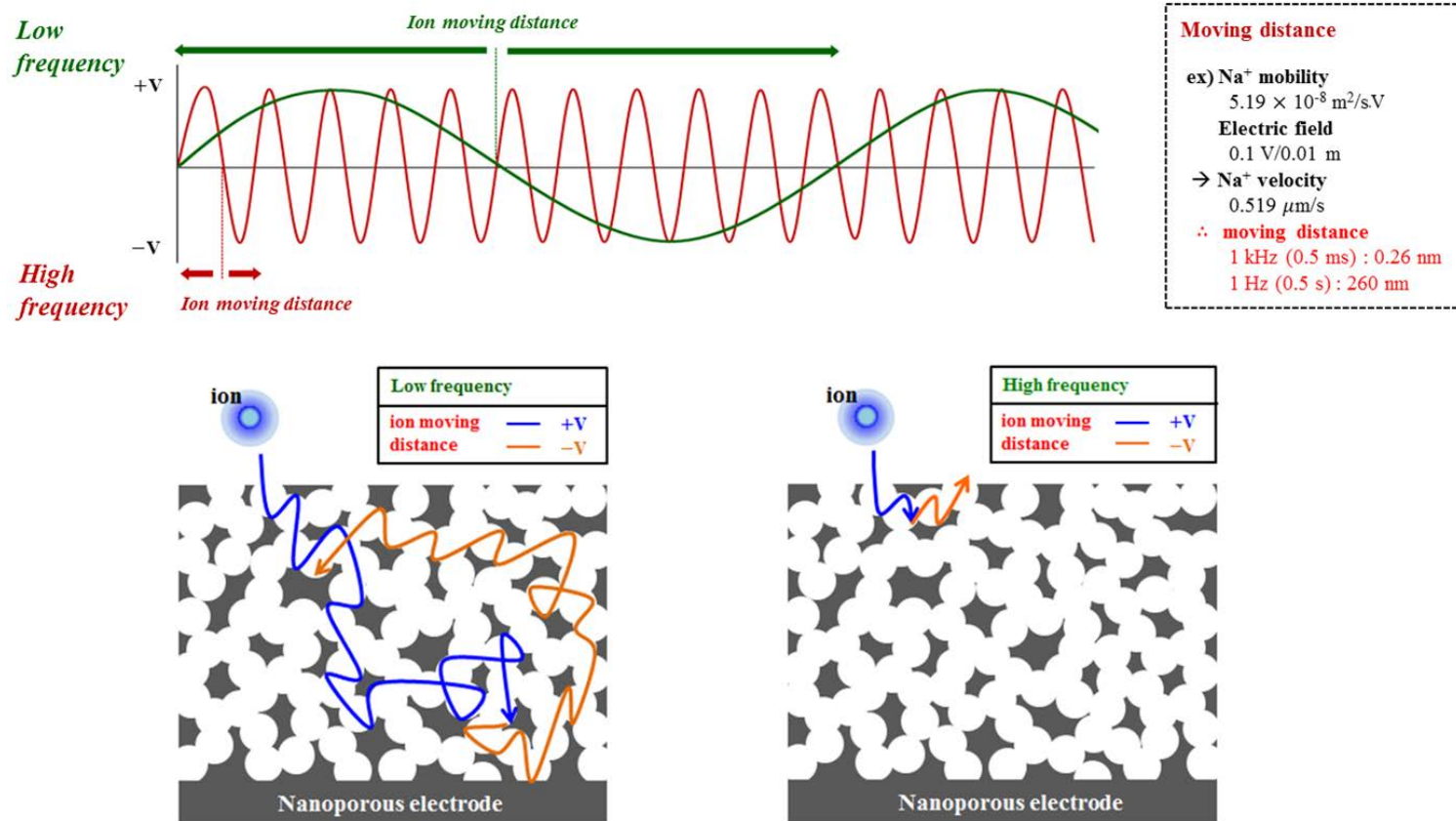


Figure 3-17. Effect of frequency on moving distance of ion in the nanoporous electrode.

3.3.8. Conductance Detection at High Electrolyte Concentration

Higher ionic strengths lead to smaller contributions of the solution resistance to the total impedance, making the measured conductance less sensitive to the change in ion concentration in the bulk solution. However, a nanoporous electrode can markedly reduce its own electrode impedance and distinctively respond to changing ion concentrations even at high frequencies. We used a synthetic seawater sample and obtained the results in Figure 3-18. As an ion suppressor was used, the eluent concentration was lowered while the concentration of analytes remained high. Overall, the conductometric responses are consistent with those from the solution of low analyte concentration, ensuring that L₂-ePt also works well at high electrolyte concentration. The peak distortion, which has a non-Gaussian peak shape, is due to column overloading (Figure H).^{118,119}

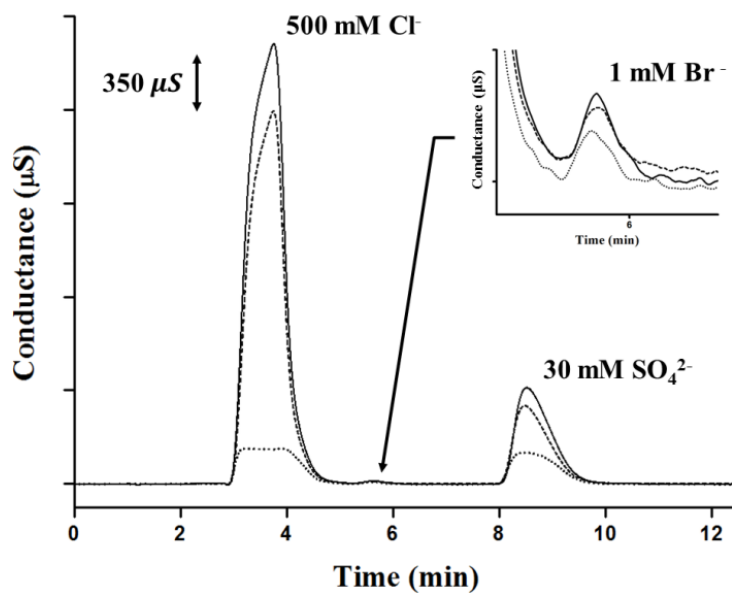


Figure 3-18. Ion chromatograms of synthetic seawater in the suppressed mode when the L₂-ePt (solid line), Pt black (dashed line), and flat Pt (dotted line) electrodes were operated at 1 kHz. Conditions: eluent, 7.5 mM sodium carbonate/1 mM sodium bicarbonate; flow gradient from 1.2 mL/min (0-2 min) to 0.8 mL/min (2-14 min); injection, 5 μ L of 500 mM Cl⁻, 1 mM Br⁻, and 30 mM SO₄²⁻.

Encouraged by the enhanced conductometric signals at nanoporous electrodes, we attempted to apply them to ion chromatography in the nonsuppressed mode, i.e., without the ion suppressor. Figure 3-19 shows the ion chromatograms of brine in which the concentrations of both the eluent and the analytes are high. The first peak is due to Na^+ ions weakly interacting with the anion-exchanger resins in the column, resulting in the shortest retention time. The second peak is due to Cl^- ions. The injected 30 mM brine sample was detected at the nanoporous Pt electrodes, while the flat Pt electrode gave a negligible signal that was indistinguishable from the background signal. The $\text{L}_2\text{-ePt}$ electrode yielded the strongest response in a highly concentrated sample (1 M brine concentration), as shown in Figure 3-19b.

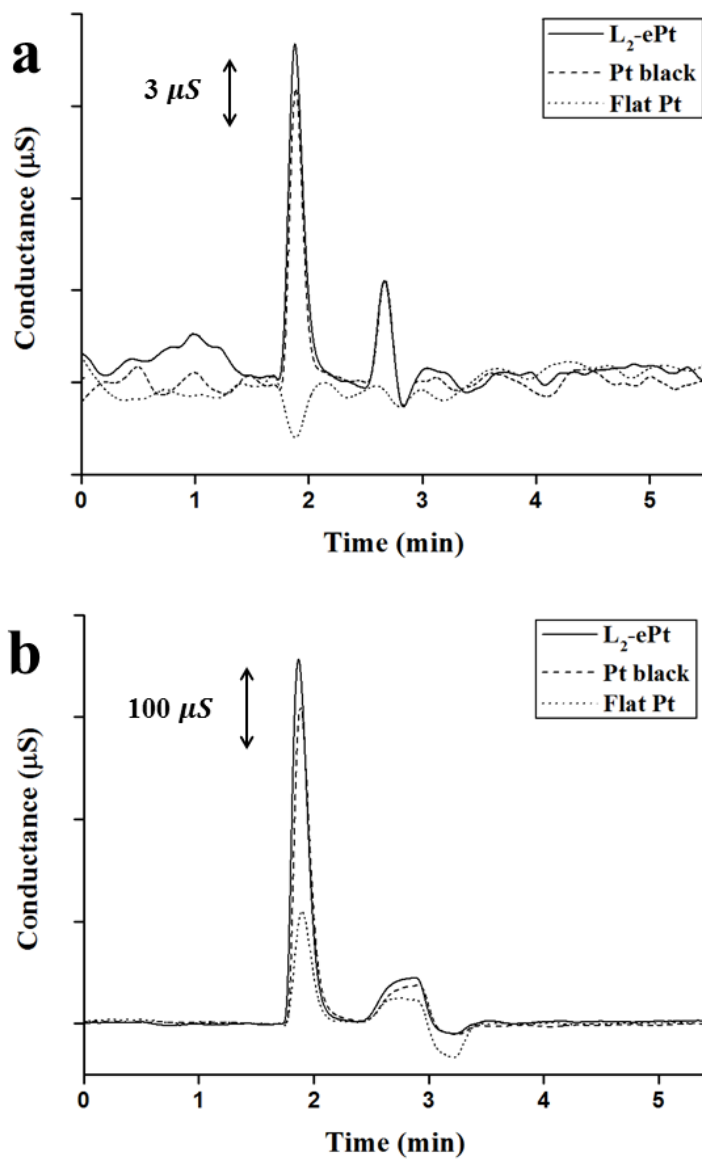


Figure 3-19. Ion chromatograms of NaCl brine in the non-suppressed mode from the $\text{L}_2\text{-ePt}$, Pt black and flat Pt electrodes at 1 kHz. Conditions: eluent, 7.5 mM sodium carbonate/1 mM sodium bicarbonate; flow rate, 1.5 mL/min; injection, 5 μL of (a) 30 mM, and (b) 1 M NaCl.

The calibration curves for the various brine concentrations are presented in Figure 3-20, indicating that L₂-ePt produces the best linearity in the calibration curves. This result suggests the possibility of conductometric detection without ion suppressors for ion chromatography by introducing nanoporous Pt with a uniform structure.

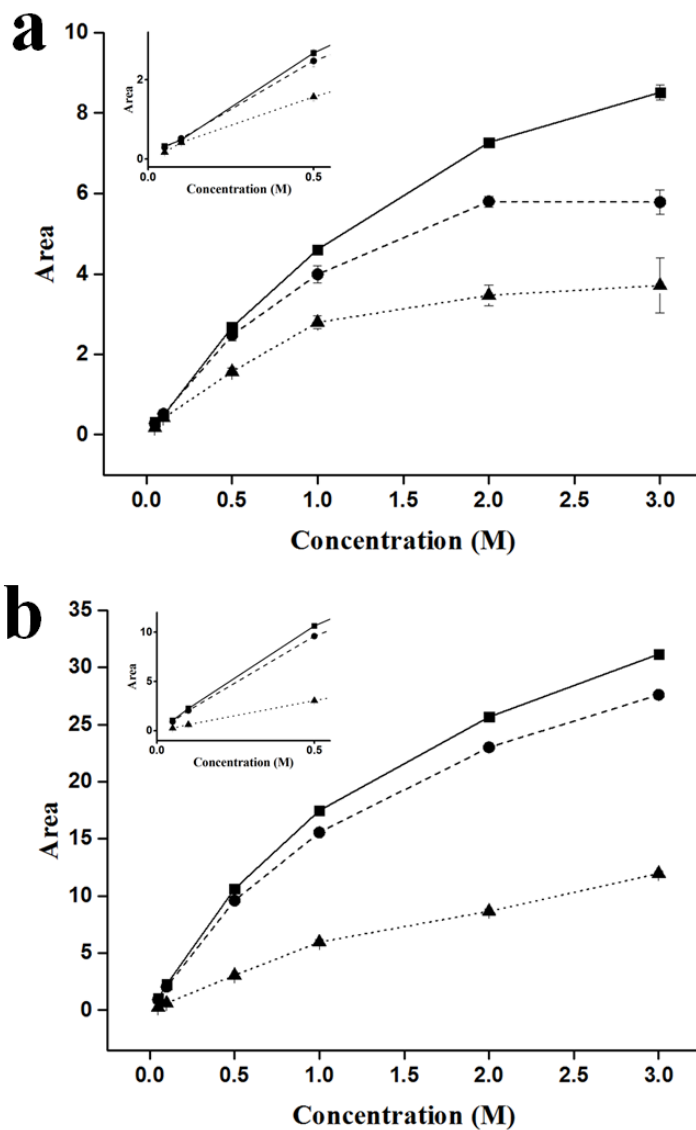


Figure 3-20. Calibration curves of peak areas for concentration of (a) Cl^- and (b) Na^+ in brine solution from the $\text{L}_2\text{-ePt}$ (solid line), Pt black (dashed line), and flat Pt (dotted line) electrodes. The conditions for ion chromatography are the same as those for Figure 3-19. The error bars are based on the standard deviations from four independent measurements for respective points.

3.4. Conclusions

Nanopores on an electrode surface create unconventional nonfaradaic charging dynamics. In this work, we investigated this phenomenon by impedance analysis using three electrodes of different morphologies, i.e., L₂-ePt, Pt black, and flat Pt, and found the unique features that can only be observed at nanoporous electrodes. Owing to not only effective suppression of electrode impedance but also characteristic elements that vary with ion concentration, the electrode impedance becomes exceptionally sensitive to the ion concentration, leading to successful conductometry measurements even at high ionic strengths and low frequencies.

L₂-ePt with more uniform nanopores exhibited a superior conductometric performance than Pt black, another well-known and widely used nanoporous electrode. The impedance spectroscopic study provided a reasonable basis to understand this behavior. The 1-2 nm pore diameter of L₂-ePt, which is comparable to the characteristic EDL thickness, enabled the detection of conductivity changes at high electrolyte concentrations. This finding offers insight into nonfaradaic electrochemical ionics at nanopores and suggests innovative applications, e.g., real-time monitoring of extracellular neuronal signals.

REFERENCES

- (1) Ge, R.; Allen, R. W. K.; Aldous, L.; Bown, M. R.; Doy, N.; Hardacre, C.; MacInnes, J. M.; McHale, G.; Newton, M. I. *Anal. Chem.* **2009**, *81*, 1628.
- (2) Dalavoy, T. S.; Wernette, D. P.; Gong, M. J.; Sweedler, J. V.; Lu, Y.; Flachsbart, B. R.; Shannon, M. A.; Bohn, P. W.; Cropek, D. M. *Lab Chip* **2008**, *8*, 786.
- (3) Park, J. Y.; Kricka, L. J. *Anal. Bioanal. Chem.* **2014**, *406*, 5631.
- (4) Kline, T. R.; Runyon, M. K.; Pothiwala, M.; Ismagilov, R. F. *Anal. Chem.* **2008**, *80*, 6190.
- (5) Qin, L. D.; Vermesh, O.; Shi, Q. H.; Heath, J. R. *Lab Chip* **2009**, *9*, 2016.
- (6) Dominguez-Vega, E.; Perez-Fernandez, V.; Crego, A. L.; Garcia, M. A.; Marina, M. L. *Electrophoresis* **2014**, *35*, 28.
- (7) Kovarik, M. L.; Ornoff, D. M.; Melvin, A. T.; Dobes, N. C.; Wang, Y. L.; Dickinson, A. J.; Gach, P. C.; Shah, P. K.; Allbritton, N. L. *Anal. Chem.* **2013**, *85*, 451.
- (8) Ríos, A.; Escarpa, A.; González, M. C.; Crevillén, A. G. *TrAC Trends in Analytical Chemistry* **2006**, *25*, 467.
- (9) Schwarz, M. A.; Hauser, P. C. *Lab Chip* **2001**, *1*, 1.
- (10) Uchiyama, K.; Nakajima, H.; Hobo, T. *Anal. Bioanal. Chem.* **2004**, *379*, 375.
- (11) Mogensen, K. B.; Klank, H.; Kutter, J. P. *Electrophoresis* **2004**, *25*, 3498.
- (12) Vandaveer, W. R.; Pasas, S. A.; Martin, R. S.; Lunte, S. M. *Electrophoresis*

- 2002**, 23, 3667.
- (13) Tanyanyiwa, J.; Leuthardt, S.; Hauser, P. C. *Electrophoresis* **2002**, 23, 3659.
 - (14) Keynton, R. S.; Roussel, T. J.; Crain, M. M.; Jackson, D. J.; Franco, D. B.; Naber, J. F.; Walsh, K. M.; Baldwin, R. P. *Anal. Chim. Acta* **2004**, 507, 95.
 - (15) Adams, R. N. *Electrochemistry at solid electrodes*; M. Dekker: New York,, 1969.
 - (16) Opallo, M.; Bilewicz, R. *Advances in Physical Chemistry* 2011.
 - (17) Mani, V.; Chikkaveeraiah, B. V.; Patel, V.; Gutkind, J. S.; Rusling, J. F. *Acs Nano* **2009**, 3, 585.
 - (18) Kim, S. N.; Rusling, J. F.; Papadimitrakopoulos, F. *Adv. Mater.* **2007**, 19, 3214.
 - (19) Jo, G.; Choe, M.; Lee, S.; Park, W.; Kahng, Y. H.; Lee, T. *Nanotechnology* **2012**, 23.
 - (20) Soleymani, L.; Fang, Z. C.; Sargent, E. H.; Kelley, S. O. *Nat. Nanotechnol.* **2009**, 4, 844.
 - (21) Das, J.; Kelley, S. O. *Anal. Chem.* **2011**, 83, 1167.
 - (22) Wittstock, A.; Zielasek, V.; Biener, J.; Friend, C. M.; Baumer, M. *Science* **2010**, 327, 319.
 - (23) Snyder, J.; Fujita, T.; Chen, M. W.; Erlebacher, J. *Nat. Mater.* **2010**, 9, 904.
 - (24) Zhang, H. G.; Yu, X. D.; Braun, P. V. *Nat. Nanotechnol.* **2011**, 6, 277.
 - (25) Chmiola, J.; Yushin, G.; Gogotsi, Y.; Portet, C.; Simon, P.; Taberna, P. L. *Science* **2006**, 313, 1760.

- (26) Steele, B. C. H.; Heinzl, A. *Nature* **2001**, *414*, 345.
- (27) Qiao, Y.; Li, C. M. *J. Mater. Chem.* **2011**, *21*, 4027.
- (28) Nazeeruddin, M. K.; Baranoff, E.; Gratzel, M. *Sol. Energy* **2011**, *85*, 1172.
- (29) Park, S.; Park, S.; Jeong, R. A.; Boo, H.; Park, J.; Kim, H. C.; Chung, T. D. *Biosens. Bioelectron.* **2012**, *31*, 284.
- (30) Hu, K. C.; Lan, D. X.; Li, X. M.; Zhang, S. S. *Anal. Chem.* **2008**, *80*, 9124.
- (31) Heim, M.; Rousseau, L.; Reculosa, S.; Urbanova, V.; Mazzocco, C.; Joucla, S.; Bouffier, L.; Vytras, K.; Bartlett, P.; Kuhn, A.; Yvert, B. *J. Neurophysiol.* **2012**, *108*, 1793.
- (32) Oren, Y. *Desalination* **2008**, *228*, 10.
- (33) Han, J. H.; Lee, E.; Park, S.; Chang, R.; Chung, T. D. *J. Phys. Chem. C* **2010**, *114*, 9546.
- (34) Bae, J. H.; Han, J. H.; Han, D.; Chung, T. D. *Faraday Discuss.* **2013**, *164*, 361.
- (35) Bae, J. H.; Han, J. H.; Chung, T. D. *Phys. Chem. Chem. Phys.* **2012**, *14*, 448.
- (36) Willard, H. H. *Instrumental methods of analysis*; 7th ed.; Wadsworth Pub. Co.: Belmont, Calif., 1988.
- (37) Guijt, R. M.; Evenhuis, C. J.; Macka, M.; Haddad, P. R. *Electrophoresis* **2004**, *25*, 4032.
- (38) Kenyon, S. M.; Meighan, M. M.; Hayes, M. A. *Electrophoresis* **2011**, *32*, 482.
- (39) Poinot, V.; Gavard, P.; Feurer, B.; Couderc, F. *Electrophoresis* **2010**, *31*,

105.

- (40) Tran, N. T.; Ayed, I.; Pallandre, A.; Taverna, M. *Electrophoresis* **2010**, *31*, 147.
- (41) Lim, Y. C.; Kouzani, A. Z.; Duan, W. *Microsyst. Technol.* **2010**, *16*, 1995.
- (42) Arora, A.; Simone, G.; Salieb-Beugelaar, G. B.; Kim, J. T.; Manz, A. *Anal. Chem.* **2010**, *82*, 4830.
- (43) Chen, X. G.; Fan, L. Y.; Hu, Z. *Electrophoresis* **2004**, *25*, 3962.
- (44) Guihen, E.; O'Connor, W. T. *Electrophoresis* **2009**, *30*, 2062.
- (45) Baker, C. A.; Duong, C. T.; Grimley, A.; Roper, M. G. *Bioanalysis* **2009**, *1*, 967.
- (46) Viskari, P. J.; Landers, J. P. *Electrophoresis* **2006**, *27*, 1797.
- (47) Opekar, F.; Stulik, K. *Electrophoresis* **2011**, *32*, 795.
- (48) Gotz, S.; Karst, U. *Anal. Bioanal. Chem.* **2007**, *387*, 183.
- (49) Kitagawa, F.; Otsuka, K. *J. Pharmaceut. Biomed.* **2011**, *55*, 668.
- (50) Renzi, R. F.; Stamps, J.; Horn, B. A.; Ferko, S.; VanderNoot, V. A.; West, J. A. A.; Crocker, R.; Wiedenman, B.; Yee, D.; Fruetel, J. A. *Anal. Chem.* **2005**, *77*, 435.
- (51) Fister, J. C.; Jacobson, S. C.; Davis, L. M.; Ramsey, J. M. *Anal. Chem.* **1998**, *70*, 431.
- (52) Wang, J. *Accounts. Chem. Res.* **2002**, *35*, 811.
- (53) Fischer, D. J.; Hulvey, M. K.; Regel, A. R.; Lunte, S. M. *Electrophoresis* **2009**, *30*, 3324.

- (54) Ghanim, M. H.; Abdullah, M. Z. *Talanta* **2011**, 85, 28.
- (55) Wallingford, R. A.; Ewing, A. G. *Anal. Chem.* **1987**, 59, 1762.
- (56) Lu, W. Z.; Cassidy, R. M. *Anal. Chem.* **1994**, 66, 200.
- (57) Park, S.; McGrath, M. J.; Smyth, M. R.; Diamond, D.; Lunte, C. E. *Anal. Chem.* **1997**, 69, 2994.
- (58) Voegel, P. D.; Zhou, W. H.; Baldwin, R. P. *Anal. Chem.* **1997**, 69, 951.
- (59) Xu, J.-J.; Wang, A.-J.; Chen, H.-Y. *TrAC Trends in Analytical Chemistry* **2007**, 26, 125.
- (60) Woolley, A. T.; Lao, K. Q.; Glazer, A. N.; Mathies, R. A. *Anal. Chem.* **1998**, 70, 684.
- (61) Wang, J.; Tian, B. M.; Sahlin, E. *Anal. Chem.* **1999**, 71, 5436.
- (62) Ertl, P.; Emrich, C. A.; Singhal, P.; Mathies, R. A. *Anal. Chem.* **2004**, 76, 3749.
- (63) Rossier, J. S.; Roberts, M. A.; Ferrigno, R.; Girault, H. H. *Anal. Chem.* **1999**, 71, 4294.
- (64) Amatore, C.; Da Mota, N.; Sella, C.; Thouin, L. *Anal. Chem.* **2007**, 79, 8502.
- (65) Amatore, C.; Da Mota, N.; Sella, C.; Thouin, L. *Anal. Chem.* **2008**, 80, 4976.
- (66) Martin, R. S.; Ratzlaff, K. L.; Huynh, B. H.; Lunte, S. M. *Anal. Chem.* **2002**, 74, 1136.
- (67) Chen, C. P.; Hahn, J. H. *Anal. Chem.* **2007**, 79, 7182.
- (68) Rossier, J. S.; Ferrigno, R.; Girault, H. H. *J. Electroanal. Chem.* **2000**, 492, 15.

- (69) Chen, D. C.; Hsu, F. L.; Zhan, D. Z.; Chen, C. H. *Anal. Chem.* **2001**, *73*, 758.
- (70) Lacher, N. A.; Lunte, S. M.; Martin, R. S. *Anal. Chem.* **2004**, *76*, 2482.
- (71) Arora, A.; Eijkel, J. C. T.; Morf, W. E.; Manz, A. *Anal. Chem.* **2001**, *73*, 3282.
- (72) Zhan, W.; Alvarez, J.; Crooks, R. M. *J. Am. Chem. Soc.* **2002**, *124*, 13265.
- (73) Klett, O.; Nyholm, L. *Anal. Chem.* **2003**, *75*, 1245.
- (74) Ordeig, O.; Godino, N.; del Campo, J.; Munoz, F. X.; Nikolajeff, F.; Nyholm, L. *Anal. Chem.* **2008**, *80*, 3622.
- (75) Chun, H. G.; Chung, T. D.; Kim, H. C. *Anal. Chem.* **2005**, *77*, 2490.
- (76) Joo, S.; Park, S.; Chung, T. D.; Kim, H. C. *Anal. Sci.* **2007**, *23*, 277.
- (77) Li, X. G.; Tian, Y.; Xia, P. P.; Luo, Y. P.; Rui, Q. *Anal. Chem.* **2009**, *81*, 8249.
- (78) Mavre, F.; Anand, R. K.; Laws, D. R.; Chow, K. F.; Chang, B. Y.; Crooks, J. A.; Crooks, R. M. *Anal. Chem.* **2010**, *82*, 8766.
- (79) Chang, B. Y.; Crooks, J. A.; Chow, K. F.; Mavre, F.; Crooks, R. M. *J. Am. Chem. Soc.* **2010**, *132*, 15404.
- (80) Dumitrescu, I.; Anand, R. K.; Fosdick, S. E.; Crooks, R. M. *J. Am. Chem. Soc.* **2011**, *133*, 4687.
- (81) Forry, S. P.; Murray, J. R.; Heien, M. L. A. V.; Locascio, L. E.; Wightman, R. M. *Anal. Chem.* **2004**, *76*, 4945.
- (82) Wallenborg, S. R.; Nyholm, L.; Lunte, C. E. *Anal. Chem.* **1999**, *71*, 544.
- (83) Klett, O.; Bjorefors, F.; Nyholm, L. *Anal. Chem.* **2001**, *73*, 1909.
- (84) Martin, R. S.; Gawron, A. J.; Lunte, S. M.; Henry, C. S. *Anal. Chem.* **2000**,

72, 3196.

- (85) Mavre, F.; Chow, K. F.; Sheridan, E.; Chang, B. Y.; Crooks, J. A.; Crooks, R. *M. Anal. Chem.* **2009**, *81*, 6218.
- (86) Matysik, F. M. *J Chromatogr. A* **1996**, *742*, 229.
- (87) Matysik, F. M. *J Chromatogr. A* **1998**, *802*, 349.
- (88) Cao, W. D.; Liu, J. F.; Yang, X. R.; Wang, E. *Electrophoresis* **2002**, *23*, 3683.
- (89) Coltro, W. K. T.; Lima, R. S.; Segato, T. P.; Carrilho, E.; de Jesus, D. P.; do Lago, C. L.; da Silva, J. A. F. *Anal. Methods-Uk* **2012**, *4*, 25.
- (90) Hilderbrand, K. S. , Preparation of Salt Brines for the Fishing Industry, **1999**;
<http://seagrant.oregonstate.edu/sites/default/files/sgpubs/onlinepubs/h99002.pdf> (Accessed 19.07.14).
- (91) Ito, K. *Anal. Chem.* **1997**, *69*, 3628.
- (92) Zakaria, P.; Bloomfield, C.; Shellie, R. A.; Haddad, P. R.; Dicinoski, G. W. *J Chromatogr. A* **2011**, *1218*, 9080.
- (93) Haddad, P. R.; Jackson, P. E.; Shaw, M. J. *J Chromatogr. A* **2003**, *1000*, 725.
- (94) Matysik, F. M. *Microchim. Acta* **2008**, *160*, 1.
- (95) Glasstone, S. *An introduction to electrochemistry*; D. Van Nostrand company, inc.: New York,, 1942.
- (96) Attard, G. S.; Bartlett, P. N.; Coleman, N. R. B.; Elliott, J. M.; Owen, J. R.; Wang, J. H. *Science* **1997**, *278*, 838.
- (97) Erlebacher, J.; Aziz, M. J.; Karma, A.; Dimitrov, N.; Sieradzki, K. *Nature* **2001**, *410*, 450.

- (98) Gogotsi, Y.; Nikitin, A.; Ye, H. H.; Zhou, W.; Fischer, J. E.; Yi, B.; Foley, H. C.; Barsoum, M. W. *Nat. Mater.* **2003**, 2, 591.
- (99) Park, S.; Song, Y. J.; Boo, H.; Chung, T. D. *J. Phys. Chem. C* **2010**, 114, 8721.
- (100) Bae, J. H.; Chung, T. D. *Electrochim. Acta* **2011**, 56, 1947.
- (101) Boo, H.; Park, S.; Ku, B. Y.; Kim, Y.; Park, J. H.; Kim, H. C.; Chung, T. D. *J. Am. Chem. Soc.* **2004**, 126, 4524.
- (102) Sun, G. W.; Wang, J. T.; Liu, X. J.; Long, D. H.; Qiao, W. M.; Ling, L. H. *J. Phys. Chem. C* **2010**, 114, 18745.
- (103) Park, S.; Lee, S. Y.; Boo, H.; Kim, H. M.; Kim, K. B.; Kim, H. C.; Song, Y. J.; Chung, T. D. *Chem. Mater.* **2007**, 19, 3373.
- (104) Kicela, A.; Daniele, S. *Talanta* **2006**, 68, 1632.
- (105) Kim, S. K.; Kim, J. Y.; Kim, K. P.; Chung, T. D. *Anal. Chem.* **2007**, 79, 7761.
- (106) Kang, C. M.; Joo, S.; Bae, J. H.; Kirn, Y. R.; Kim, Y.; Chung, T. D. *Anal. Chem.* **2012**, 84, 901.
- (107) Trasatti, S.; Petrii, O. A. *J. Electroanal. Chem.* **1992**, 327, 353.
- (108) Robinson, D. B.; Wu, C. A. M.; Jacobs, B. W. *J. Electrochem. Soc.* **2010**, 157, A912.
- (109) De Levie, R. *Electrochim. Acta* **1963**, 8, 751.
- (110) Elliott, J. M.; Owen, J. R. *Phys. Chem. Chem. Phys.* **2000**, 2, 5653.
- (111) Robinson, D. B.; Wu, C. A. M.; Ong, M. D.; Jacobs, B. W.; Pierson, B. E.

Langmuir **2010**, *26*, 6797.

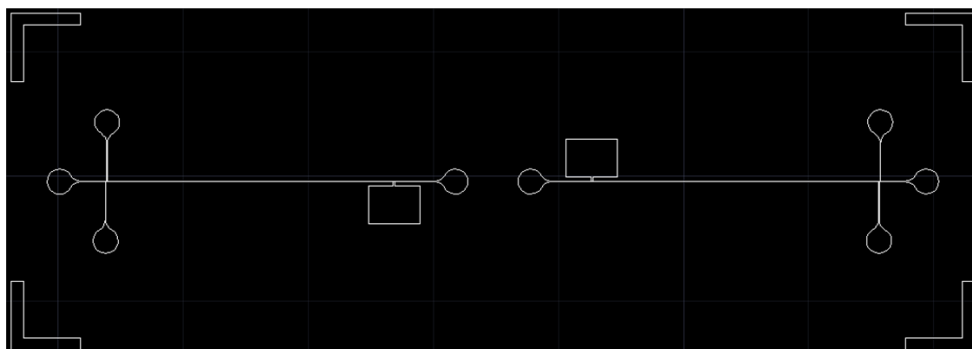
- (112) Bisquert, J.; Garcia-Belmonte, G.; Fabregat-Santiago, F.; Ferriols, N. S.; Bogdanoff, P.; Pereira, E. C. *J. Phys. Chem. B* **2000**, *104*, 2287.
- (113) Barsoukov, E.; Macdonald, J. R. *Impedance spectroscopy: theory, experiment, and applications*; John Wiley & Sons, 2005.
- (114) Walcarius, A.; Etienne, M.; Lebeau, B. *Chem. Mater.* **2003**, *15*, 2161.
- (115) Delacote, C.; Gaslain, F. O. M.; Lebeau, B.; Walcarius, A. *Talanta* **2009**, *79*, 877.
- (116) Song, H. K.; Jung, Y. H.; Lee, K. H.; Dao, L. H. *Electrochim. Acta* **1999**, *44*, 3513.
- (117) Song, H. K.; Hwang, H. Y.; Lee, K. H.; Dao, L. H. *Electrochim. Acta* **2000**, *45*, 2241.
- (118) Golshanshirazi, S.; Guiochon, G. *Anal. Chem.* **1989**, *61*, 462.
- (119) Wahab, M. F.; Anderson, J. K.; Abdelrady, M.; Lucy, C. A. *Anal. Chem.* **2014**, *86*, 559.

APPENDIX

A. Mask Layout

A-1. PGSB-Integrated Microchip

Microchannel



Microelectrode

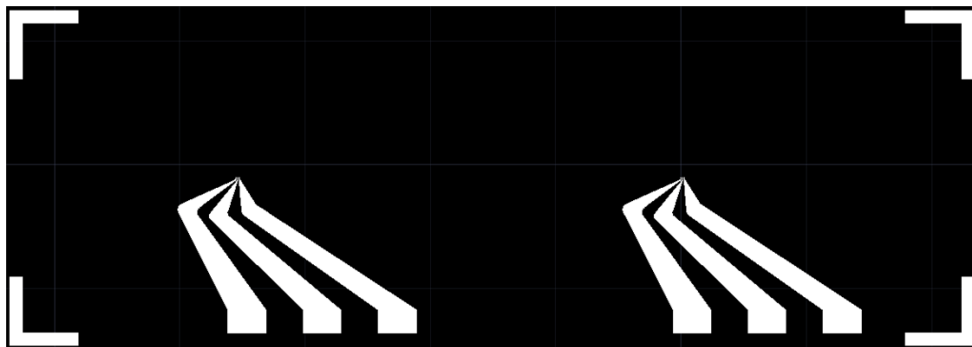
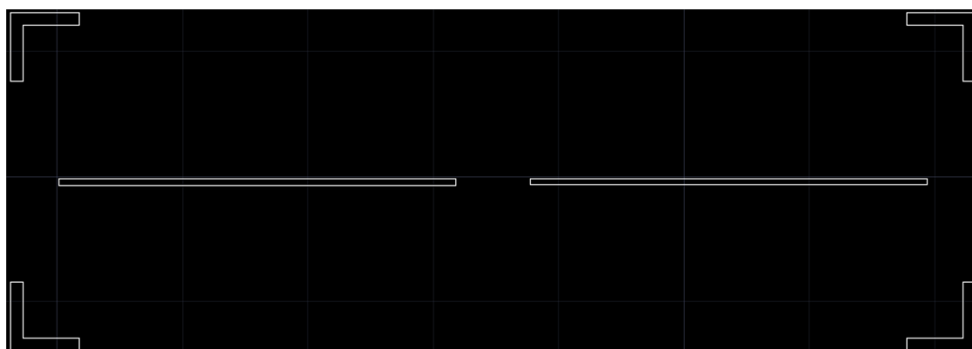


Figure A-1. Mask layout for a PGSB-integrated microchip (chapter 2).

A-2. Mask for Conductivity Detection

Microchannel



Microelectrode

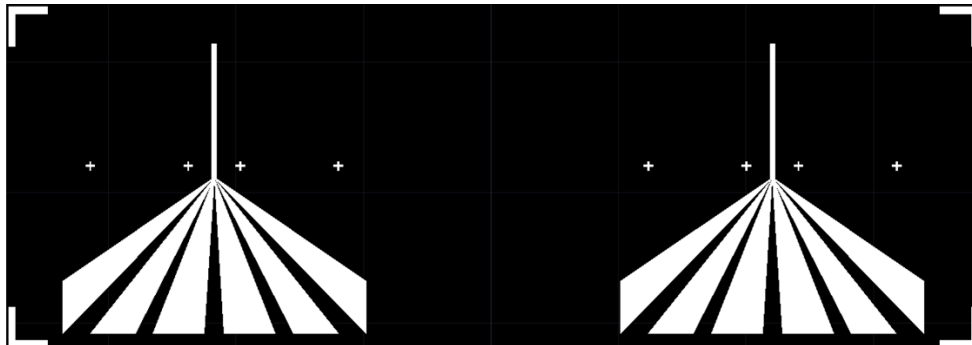


Figure A-2. Mask layout for conductivity detection (chapter 3).

B. Microchip Fabrication for Conductivity Detection

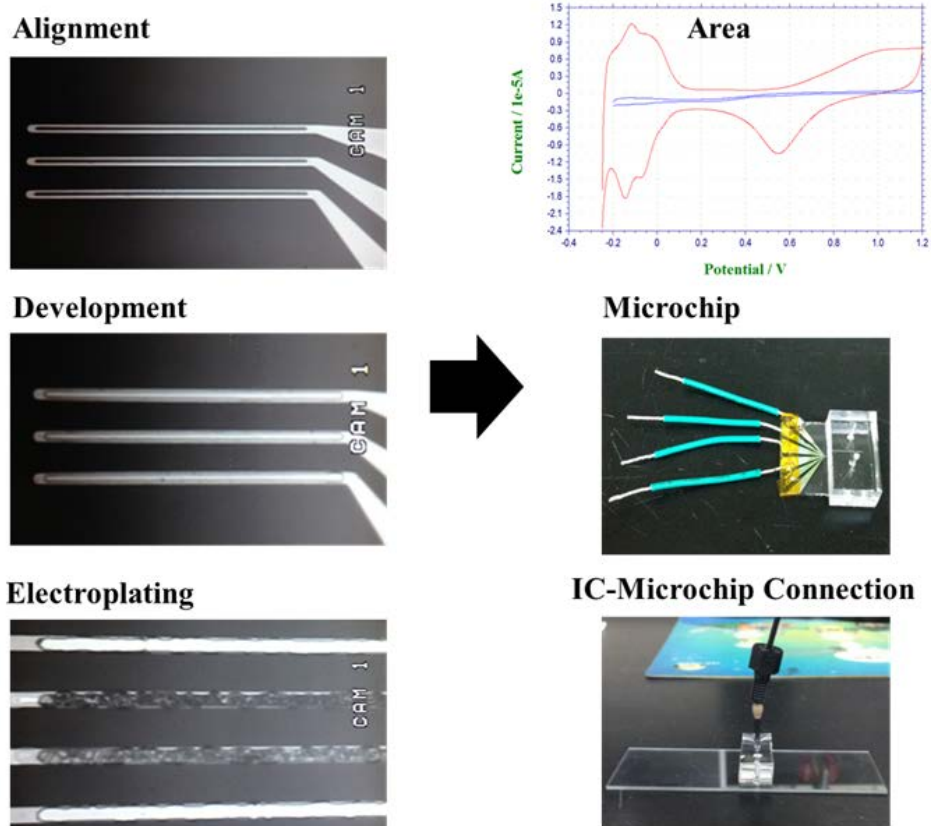


Figure B. Microchip fabrication for an ion chromatography detector. The fabrication process comprises consecutive electrode patterning, oxide layer deposition, development, electroplating, patterned PDMS bonding, and IC-microchip connection formation (Chapter 3).

C. Simulation of Electric Field Gradient Using CFD-ACE+

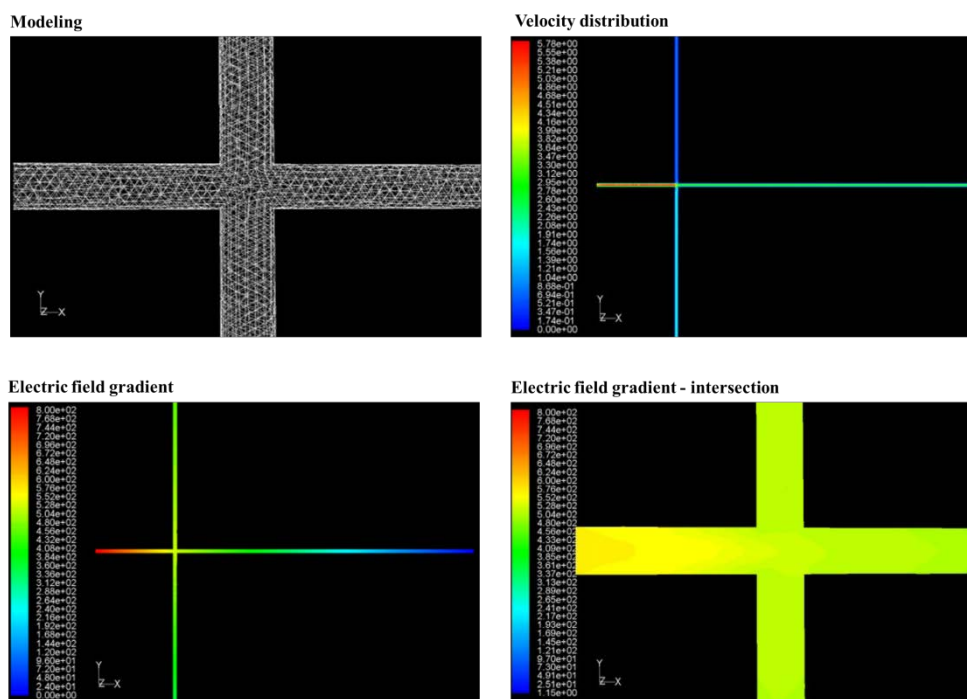


Figure C. CFD-ACE+ simulation. Channel dimensions: 100 μm wide, 30 μm deep. The parameters of the aqueous solution, such as density and viscosity, were included in this simulation (Chapter 2).

D. Measurement of the Potential Window of the Gold Electrode

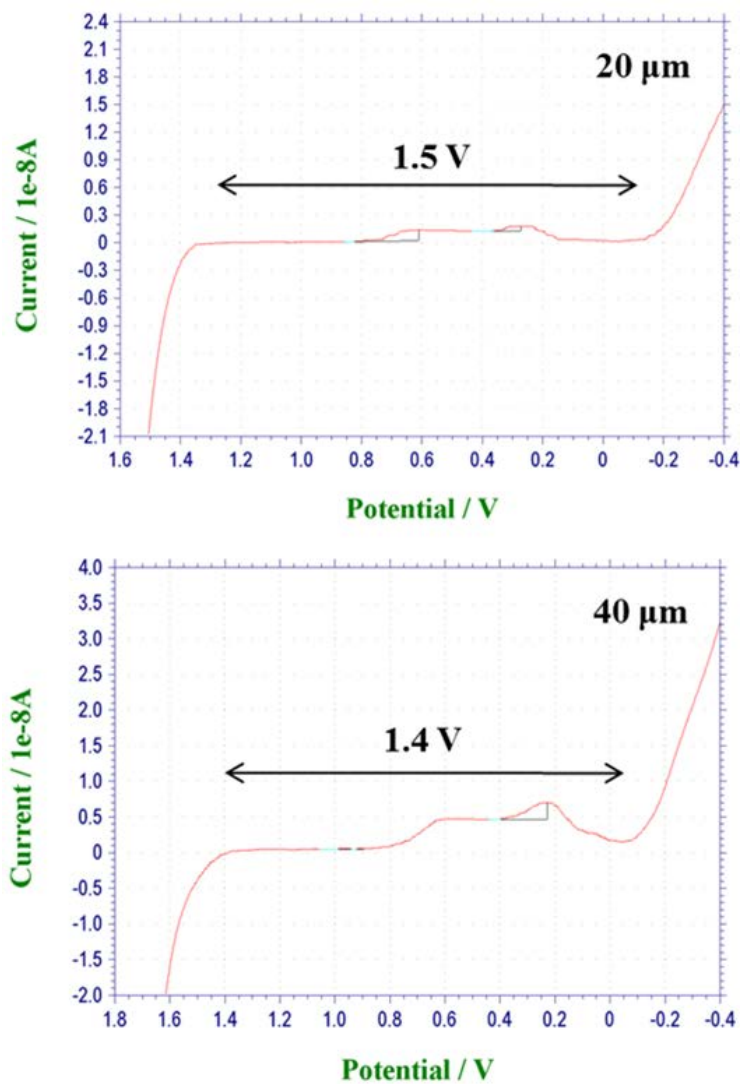


Figure D. *I*–*V* curves for the gold electrode in the 0.1 M KNO₃ and MES buffer. Conditions: Widths of the Au working electrodes: 20 μm and 40 μm; reference electrode: Ag/AgCl/KCl (3 M); counter electrode: Pt wire; scan rate: 50 mV/s (Chapter 2).

E. Difference of OCP of the Forward and Reverse Electric Fields

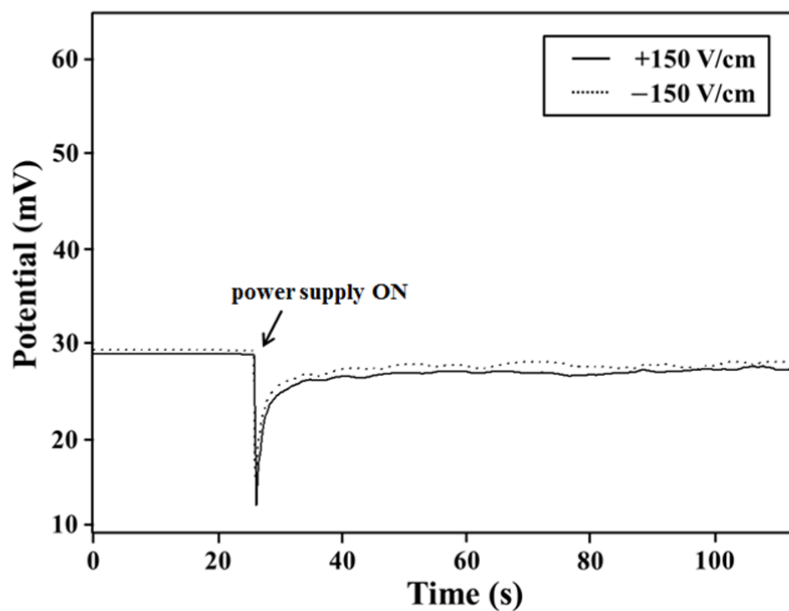


Figure E. Comparison of the open circuit potentials under forward and reverse electric fields. There is little difference between the forward and reverse electrophoretic fields. As stated in the “Instruments” section, the potentiostatic circuit for detection was electrically isolated from the custom-made DC power supply for the electrophoretic field. Repetitive reversals of the applied electrophoretic field between +150 and -150 V/cm showed a voltage change of less than 5 mV in the open circuit potential of the Au electrode, as shown in this figure (Chapter 2).

F. Test of Ion Leakage through PGSB

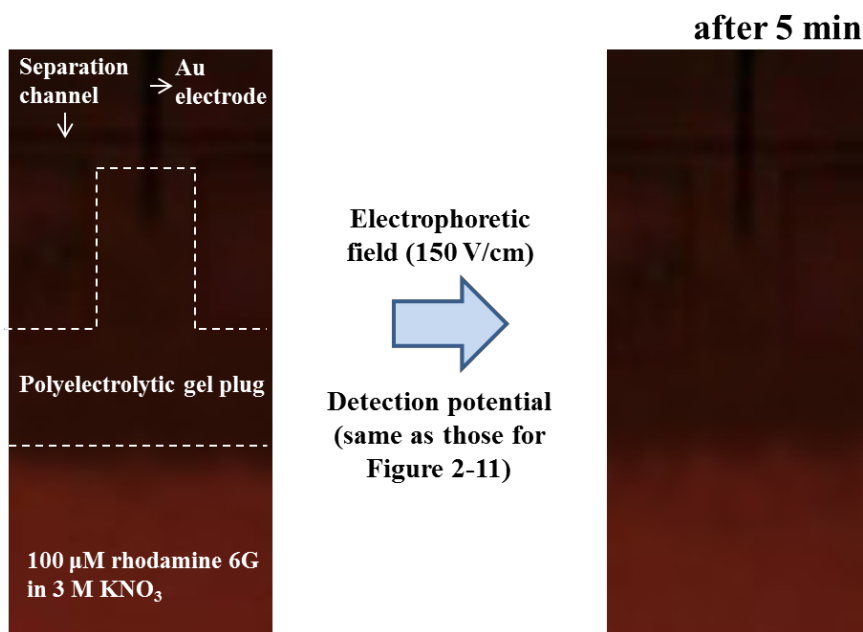


Figure F. Leakage test of the inner solution and ions in the microchannel. Hardened PGSB (with a negatively charged backbone) has such a high density of fixed charges that it should be able to effectively block the electrolyte solution. We monitored the motion of Rhodamine 6G, which is a cationic fluorescent dye that is in the chamber for the internal filling solution of the reference electrode, into the separation channel through the PGSB. The conclusion was that ion leakage through the PGSB is negligible (Chapter 2).

G. Comparison of the Real Surface Areas of the Microelectrodes

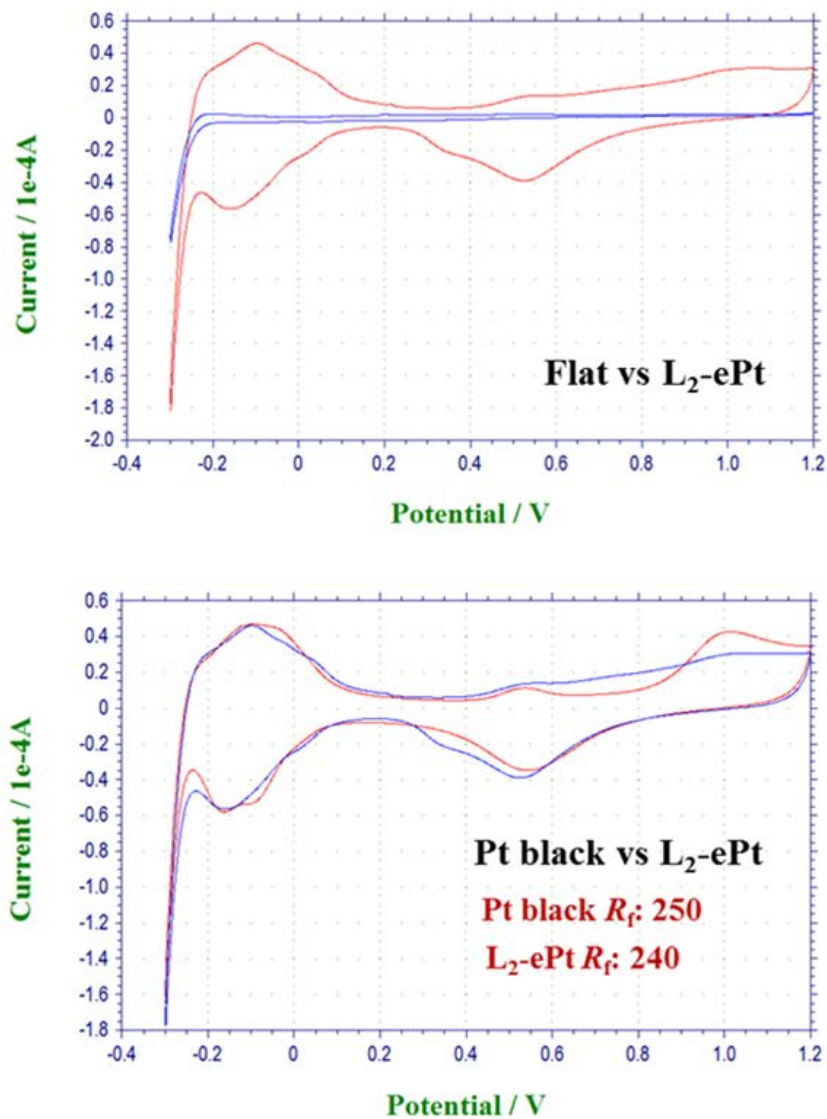
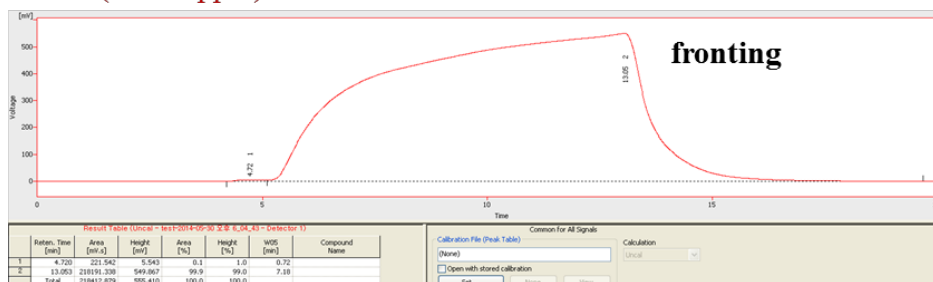


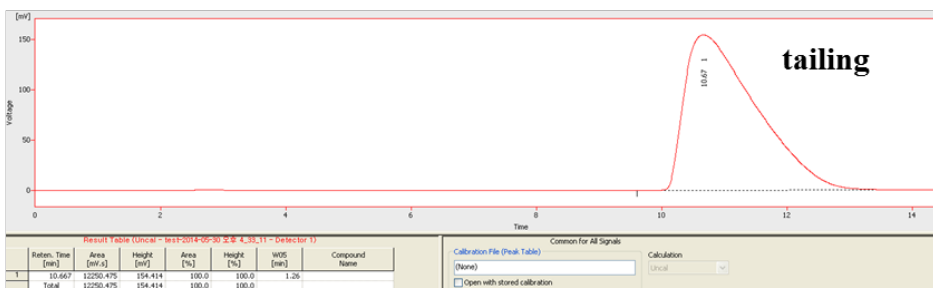
Figure G. Comparison of the cyclic voltammograms of the electrodeposited Pt microelectrodes (i.e., L₂-ePt and Pt black) and the flat Pt microelectrode in 0.5 M H₂SO₄ at 50 mV/s (Chapter 3).

H. Peak Distortion Effects in Ion Chromatography

0.5 M (17726 ppm) Cl^- (ion suppressor ON)



0.03 M (2882 ppm) SO_4^{2-}



0.001 M (80 ppm) Br^-

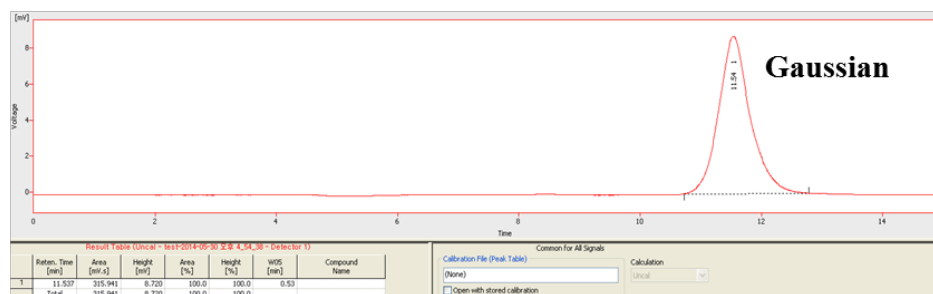


Figure H. Peak distortion effects under overloaded conditions of sample ions in conventional ion chromatography. Conditions: Eluent: 3.5 mM sodium carbonate/1 mM sodium bicarbonate; flow rate: 1.2 mL/min; injection: 25 μL (Chapter 3).

LIST OF PUBLICATIONS

1. Ji-Hyung Han, Kwang Bok Kim, Je Hyun Bae, Beom Jin Kim, **Chung Mu Kang**, Hee Chan Kim, and Taek Dong Chung “Ion Flow Crossing over a Polyelectrolyte Diode on Microfluidic Chip” *Small* **2011**, 7, 2629.
2. **Chung Mu Kang**, Segyeong Joo, Je Hyun Bae, Yang-Rae Kim, Yongseong Kim, and Taek Dong Chung “In-Channel Electrochemical Detection in the Middle of Microchannel under High Electric Field” *Anal. Chem.* **2012**, 84, 901.
3. Donghoon Han, Yang-Rae Kim, **Chung Mu Kang**, and Taek Dong Chung “Electrochemical Signal Amplification for Immunosensor based on 3D Interdigitated Array Electrodes” *Anal. Chem.* **2014**, 86, 5991.
4. Je Hyun Bae[†], **Chung Mu Kang**[†], Hyoungseon Choi, Beom Jin Kim, Woohyuk Jang, Sung Yul Lim, Hee Chan Kim, and Taek Dong Chung “Nonfaradaic Nanoporous Electrochemistry for Conductometry at High Electrolyte Concentration” *Anal. Chem.* **2015**, in press, DOI: 10.1021/ac504415c. († Two authors are equally contributed to this paper.)

ABSTRACT (in Korean)

전기화학적 원리에 기반을 둔 원천기술은 바이오, 제약, 화학 및 환경 분석을 위한 소형화 시스템을 구축하는데 유리한 장점을 가지고 있다. 우선, 전기화학 시스템은 근본적으로 소형화에 유리하고, 초소형 전자기계기술의 발달과 도입으로 소형화 특성을 극대화 할 수 있다. 또한, 소형 분석시스템에 필요한 시료 주입 및 농축, 혼합, 분리, 검출 등 다양한 요소기술을 전기화학적 원리를 통해 구현할 수 있다.

소형 분석시스템에 적용되는 여러 가지 요소기술 중, 검출기술은 소형화와 분석성능에 직접 관계하기 때문에 중요한 분야로 인식된다. 따라서, 소형 분석시스템과 관련된 수많은 검출 전략이 제안되고 있다. 전기화학 검출법의 경우 소형화에 따른 성능 저하 현상이, 다른 검출 방법들 (광학/질량 검출법)에 비해 상대적으로 작기 때문에 소형 분석 시스템에 접목하기 쉬운 검출 방법으로 관련 연구 사례가 많이 보고 되고 있다. 하지만, 현재까지 보고된 우수한 전기화학적 검출 사례들에도 불구하고, 소형 분석시스템에서 보다 효과적으로 전기화학적 검출법을 수행할 수 있도록 마이크로 전극 설계, 전극 물질 개발, 전극의 구조적 효과 등에서 제기되는 문제점 등을 개선하고 극복해야 한다. 본 학위 논문은 강한 전기장의 간섭효과를 최소화하는 새로운 마이크로 전기화학 검출시스템과, 전도도 검출법의 한계를 극복할 수 있는 나노다공성 전극의 구조적 특성에 관한 연구내용으로 구성된다.

1 장에서 소형 분석시스템의 배경과 현재 직면하고 있는 문제점들에 대해 전반적으로 다뤘고, 특히 소형 분석장치의 전기화학적 검출법과 관련된 내용을 중심으로 기술했다.

2 장에서 전기영동이 수행되는 분리 채널에 폴리전해질 염다리를 집적하고, 강한 전기장이 인가된 분리 채널 내에서 전기화학적 검출법을 수행할 수 있는 새로운 방법을 제안했다. 작업전극과 폴리전해질 염다리를 마이크로 채널 내부 등전위면에 위치시키면, 분리효율을 저해하는 현상과 외부전기장의 간섭효과를 최소화할 수 있고 이를 통해 고감도 전기화학 검출법을 수행할 수 있다. 본 전기화학 검출시스템의 동작 원리를 검증하기 위해, 작업전극과 폴리전해질 염다리 (기준전극) 사이의 거리와 외부 전기장의 세기를 변화시키며, 전기적으로 분리된 일정 전위기를 사용해 개방회로 전위를 측정했다. 또한, 강한 전기장 (~ 400 V/cm)이 인가된 마이크로 채널 내부에서 순환 전압전류법을 수행함으로써, 외부 전기장의 간섭효과를 최소화하는 전기화학 검출시스템의 성능을 검증했다. 결과적으로 카테콜, 도파민 등의 생물질 분리와 전기화학적 검출과정 등을 통해, 소형 분석장치의 효과적인 검출 방법으로 가능성을 검증했다. 향후 강한 전기장을 이용한 마이크로칩 전기영동 분야에서 획기적인 전기화학 검출법으로 널리 활용될 것으로 기대된다.

주요어 : 마이크로칩, 전기화학 검출법, 폴리전해질 염다리, 등전위면, 전기영동장, 내부채널

3 장에서 나노포러스 전극의 구조적 효과에 기인한 이온의 전기화학적 거동을 살펴보고, 전도도 셀의 작업 전극으로 활용함으로써 이온 크로마토그래피의 전도도 검출 성능 한계를 개선했다. 나노포러스 전극은 포어 사이즈, 모폴로지, 이온강도, 전기장의 변화에 따라 민감한 비패러데이 특성을 보인다. 본 연구에서 이온 농도와 교류전기장의

조절을 통해 전극 표면의 전기적 이중층 중첩 현상과 이온 이송능력을 살펴보고 전극 임피던스에 미치는 효과를 확인했다. 전송선 이론 모델에 기반을 둔 임피던스 분석법은, 해당 등가회로를 통해 이온농도와 전극 표면 모폴로지의 변화에 따라 결정되는 포어저항과 캐패시턴스 값을 알려준다. 균일한 포어 사이즈와 기하학적 구조를 가진 나노포러스 백금 (L_2 -ePt)을 불균일한 포어 사이즈의 수지상 구조를 가진 나노포러스 백금 (Pt black)과 비교 했다. 실제 면적이 비슷함에도 불구하고, L_2 -ePt 는 Pt black 에 비해 용액의 전도도 변화에 민감하게 감응했다. 또한, 일반적으로 측정하기 어려운 것으로 알려진 고농도의 전해질 환경에서 L_2 -ePt 는 Pt black 이나 flat Pt 에 비해 우수한 선형 감응을 보였다. 따라서, 나노포러스 전극의 모폴로지 효과를 적절히 활용하면 고농도의 전해질 환경에서 이온 서프레스의 도움 없이 성공적으로 이온 크로마토그래피의 전도도 검출법을 수행할 수 있다.

주요어 : 비패러데이 전기화학적 거동, 표면 모폴로지, 전기적 이중층 중첩, 포어 저항, 이온 농도, 나노포러스 백금, 이온 크로마토그래피

* 본 학위 논문을 구성하고 있는 연구내용은 본 저자가 SCI 논문에 출판한 내용을 대부분 복제했다 (*Anal. Chem.*, 2012, 84, 901 & *Anal. Chem.*, 2015, in press, DOI: 10.1021/ac504415c).

학번 : 2008-30810